

**LIBRARY
Michigan State
University**

This is to certify that the
dissertation entitled

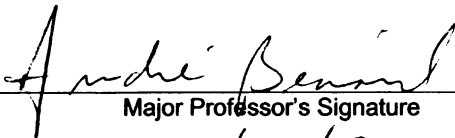
**A METHODOLOGY FOR MATERIAL DESIGN APPLIED TO
POROUS MEDIA WITH FLOW**

presented by

DEEP BANDYOPADHYAY

has been accepted towards fulfillment
of the requirements for the

PhD degree in Mechanical Engineering


Major Professor's Signature

8/21/08

Date

A METHODOLOGY FOR MATERIAL DESIGN APPLIED
TO POROUS MEDIA WITH FLOW

By

Deep Bandyopadhyay

A DISSERTATION

Submitted to
Michigan State University
in partial fulfillment of the requirements
for the degree of

DOCTOR OF PHILOSOPHY

Mechanical Engineering

2008

ABSTRACT

A METHODOLOGY FOR MATERIAL DESIGN APPLIED TO POROUS MEDIA WITH FLOW

By

Deep Bandyopadhyay

Two methodologies to design the microstructure of porous materials are presented in this work. The methodologies are based on shape and topology optimization and allow to identify layouts of the microstructure of a periodic cells using criteria such as maximizing the effective properties, minimizing the energy losses, or maximizing the mixing of a dispersed solute. The porous materials studied are made of a mixture of a heterogeneous solid matrix with its void filled with fluids. There exist two relevant length scales in the model materials: a microscale, which is associated with the pores, and a large scale associated with the overall part.

The governing equations for the microscale and the large scale are related through the effective properties. These effective properties are derived using the theory of homogenization. Expressions derived using homogenization for effective properties such as permeability, dispersivity are computed using finite element analysis and validated with experimental results. Shape and topology optimization are used to find the optimal shape and layout of the microstructure.

In shape optimization, an algorithm is developed to find an optimal shape of the pores in the microstructure for a given criterion for single and multiphase flow. Three different shapes for the solid region of the microstructure were analyzed: circular, elliptic and rectangular geometries. The macroscopic fluid flow and solute transport equations were solved based of the effective properties computed for the optimized microstructure. The velocity and solute fields were compared with those computed from a microstructure form by square array of identical porosity as of the optimized microstructure. The result showed that the optimized microstructure has a significant improvement in reducing energy loss during fluid flow and increasing mixing of the dispersed solute.

Topology optimization is then used to design porous media for two different objective functions: minimizing dissipation power and maximizing dispersive power. The governing equations were solved using finite element analysis and the sensitivity is computed using an adjoint problem based of the approach. The results were evaluated by comparing the macroscopic fluid flow for the optimal microstructure with the flow obtained for a microstructures formed by square array with same porosity as the optimized microstructure.

ACKNOWLEDGMENTS

I wish to express my sincere gratitude to my advisor Dr. André Bénard and my committee members Dr. Charles Petty, Dr. Alejandro Diaz, and Dr. Craig Somerton for their unfailing support in my PhD study. Their advice on technical matters, encouragement, motivation and constructive criticism were greatly acknowledged.

This work is supported by I/UCRC-MTP. This support is gratefully acknowledged. The implementation of the method of moving asymptotes used here was provided by Prof. Krister Svanberg from the Department of Mathematics at KTH in Stockholm. I thank Prof. Svanberg for allowing us to use his program.

I would also like to thank Department of Mechanical Engineering, Michigan State University for their financial support in time of need. I am also grateful to College of Engineering, Michigan State University which has provided the best research resources and facilities. I wish to thank the entire staff of Mechanical engineering, OISS, DECS and Graduate School for their valuable timely assistance.

Finally, I wish to express my heartfelt gratitude to my parents Biplab and Krishna Bandyopadhyay and my in laws Madhukar and Meena Meshram for the constant support and encouragement. Words cannot express how thankful I am to my dearest wife Manisha for her love and care. I would also like to thank my sister Joyeta Chatterjee, brother in

laws Bipul Chatterjee and Mayur Meshram and last but not the least to my dearest nephew Kabir. Without their support this dissertation would not have been possible. It is to my family I dedicate this dissertation.

TABLE OF CONTENTS

LIST OF TABLES	ix
LIST OF FIGURES	x
LIST OF FIGURES	x
NOMENCLATURE	xvi
CHAPTER 1	1
INTRODUCTION	1
1.1 General	1
1.2 Solute Transport and Fluid Flow in Porous Media	4
1.3 Research Approach	5
1.4 Material design techniques	7
1.5 Dissertation layout	8
CHAPTER 2	10
THEORY FOR SINGLE PHASE FLUID FLOW IN POROUS MEDIA	10
2.1 Introduction	10
2.2 Derivation of Effective Permeability Tensor	12
2.3 Computation of Effective Permeability Tensor	19
CHAPTER 3	22
THEORY FOR SOLUTE TRANSFER IN POROUS MEDIA	22
3.1 Introduction	22
3.2 Derivation of Effective Dispersion Tensor	22
3.3 Computation of Effective Dispersion Tensor	29
CHAPTER 4	36
DESIGN OF POROUS MEDIA USING SHAPE OPTIMIZATION TO OPTIMIZE EFFECTIVE PROPERTIES	36
4.1 Introduction	36
4.2 Identifying the Periodic Cell	36
4.3 Formulation of the optimization problem	41
4.3.1 Maximize effective permeability	41
4.3.1.1 Example Problems	43
4.3.2 Maximizing the effective dispersivity	54
4.3.2.1 Example Problems	55
4.4 Discussion	68
CHAPTER 5	70

DESIGN OF POROUS MEDIA USING SHAPE OPTIMIZATION TO MAXIMIZE “DISPERSIVE POWER” AND MINIMIZE DISSIPATION POWER.....	70
5.1 Introduction.....	70
5.2 Optimization of “dispersive power” and dissipation power	70
5.3 Example Problems	74
5.3.1 Optimization of dispersive power and dissipation power for a given base dimension and pressure gradient.....	77
5.3.2 Optimization of the “dispersive power” and the dissipation power for a given base dimension	83
5.4 Discussion.....	97
 CHAPTER 6	103
TOPOLOGY OPTIMIZATION OF FLUID FLOW IN POROUS MEDIA TO MINIMIZE DISSIPATION POWER.....	103
6.1 Introduction.....	103
6.2 Formulation of the optimization problem.....	106
6.2.1 Minimizing Dissipation power	108
6.2.2 Implementation Issues	112
6.3 Example Problems	114
6.3.1 Minimizing Dissipation Power	116
6.4 Discussion.....	127
 CHAPTER 7	131
TOPOLOGY OPTIMIZATION OF SOLUTE TRANSPORT IN POROUS MEDIA TO MAXIMIZE “DISPERSIVE POWER”	131
7.1 Introduction.....	131
7.2.1 Maximizing “Dispersive power”	136
7.2.2 Implementation Issues	139
7.3 Example Problems	141
7.3.1 Maximizing “Dispersive power”	143
7.4 Discussion.....	146
 CHAPTER 8	147
THEORY FOR MULTIPHASE FLUID FLOW IN POROUS MEDIA	147
8.1 Introduction.....	147
8.2 Derivation of Effective Permeability Tensor using Mixture Model	148
8.3 Identifying the Periodic Cell.....	154
8.4 Formulation of the optimization problem.....	158
8.4.1 Minimize dissipation power for multiphase fluid flow.....	158
8.5 Example Problems	159
8.5.1 Minimize dissipation power for multiphase fluid flow.....	160
8.6 Discussion.....	171

CHAPTER 9	174
SUMMARY AND CONCLUSION	174
APPENDIX A	180
APPENDIX B	190
APPENDIX C	195
REFERENCES	200

LIST OF TABLES

Table 1.1 List of engineering disciplines where porous materials are used. In many instances the microstructure of the porous material has a direct impact on performance.	2
Table 3.1 Parameters corresponding to the geometry shown in Figure (3.2) and which are used in the solution of the dispersion tensor.....	32
Table 4.1 Dimensions of the microstructures shown in Figure (4.8).....	51
Table 4.2 Dimensions of the microstructures as shown in Figure (4.13) .	63
Table 5.1 Dimensions of the periodic cells shown in Figure (5.2).....	80
Table 5.2 Dimensions of the microstructures as shown in Figure (5.8). ..	90
Table 5.3 Optimized value of normalized dissipation power and normalized dispersion power for the microstructures as shown in Figure (5.8).....	91
Table 8.1 Dimensions of the microstructures shown in Figure (8.5).....	165
Table 8.2 Optimized value of normalized dissipation power and normalized dispersion power for the microstructures as shown in Figure (8.8).....	170

LIST OF FIGURES

Images in this thesis/dissertation are presented in color.

Figure 1.1. a-d. Examples of industrial applications of porous media. 3

Figure 1.2 Flow chart providing an overview of the methodology 6

Figure 1.3. a-b. Examples of (a) shape optimization and (b) topology optimization from (Jorgen, 2003). 7

Figure 2.1 Schematic showing the particle pore diameter for porous media from (Kaviany 1991)..... 11

Figure 2.2. Schematic of a porous material (Ω_M) in (a) made of an assembly of periodic microscopic cells (Ω_m) (b). The interface between the solid-fluid in each periodic cell is Γ_{sl} and the interface between two periodic cells is denoted by Γ_{cell} 13

Figure 2.3 Contour plot of the distribution of the longitudinal component of the permeability tensor (μU) for round cylinder in a square periodic domain. The results are presented in m^2 21

Figure 3.1. Schematic of macrostructure (Ω_M) (a) consisting of periodic microscopic cells (Ω_m) (b). The interface between the solid-fluid in each periodic cell is Γ_{sl} and the interface between two periodic cells is denoted by Γ_{cell} 24

Figure 3.2 Schematic of a periodic microscopic cells. Dimensions of a, b, l, h are tabulated in Table (3.2) for a typical cells. “a” is the only parameter used in the optimization of a cylinder. 31

Figure 3.3 Comparison of dimensionless longitudinal effective dispersion tensor measured through experiments (data taken from Buyuktas and Wallender 2004) with numerical results obtained in this work using homogenization for a porosity of 0.8..... 33

Figure 3.4 Comparison of dimensionless longitudinal effective dispersion tensor measured through experiments for a cubic array of a porosity 0.43 (Gunn and Pryce 1969) and numerical simulations obtained with square array of particles of porosity 0.4 (Edwards et al. 1991) with results obtained in this work using homogenization. 34

Figure 4.1 Schematic of of the arrangement of the cells in the macroscopic domain studied consisting of periodic microscopic cells as shown in dashed line.	38
Figure 4.2 Schematic of periodic microscopic cells with an elliptic solid region.	39
Figure 4.3 Schematic of periodic microscopic cells formed from a rectangular solid region.....	40
Figure 4.4 Schematic of the unstructured triangular mesh used for finite element analysis.	44
Figure 4.5 Graph of the iteration history for circular solid region with varied step size and initial conditions.	46
Figure 4.6 Graph of the iteration history for elliptic solid region with varied step size and initial conditions.	47
Figure 4.7 Graph of the iteration history for rectangular solid region with varied step size and initial conditions.	48
Figure 4.8. a-c. Schematic of the optimal periodic cells obtained after optimization. Dimensions of the periodic cells are shown in Table (4.1)	50
Figure 4.9. a-c. Schematic of distribution of longitudinal permeability (μU_{11}) for microstructures shown in Figure (4.5).....	53
Figure 4.10 Graph of the iteration history for circular solid region with varied step size and initial conditions.	58
Figure 4.11 Graph of the iteration history for elliptic solid region with varied step size and initial conditions.	59
Figure 4.12 Graph of the iteration history for rectangular solid region with varied step size and initial condition.....	60
Figure 4.13. a-c. Schematic of the optimal periodic cells obtained after optimization with dimensions tabulated in Table (4.2)	62
Figure 4.14 a-c. Schematic of distribution of longitudinal dispersivity (Z_{11}) for microstructures shown in Figure (4.7).....	66

Figure 4.15 a-c. Schematic of velocity for microstructures shown in Figure (4.7)	67
Figure 5.1 Schematic of the unstructured triangular mesh used for finite element analysis.	76
Figure 5.2 a-h Schematic of the optimal periodic cells obtained after optimization for the dimensions tabulated in Table (5.1).....	79
Figure 5.3 Computed values of the objective functions for a parallel flow configuration.	81
Figure 5.4 Computed values of the objective functions for a cross flow configuration.	82
Figure 5.5 Graph of the iteration history for the circular solid region with a varied step size and initial conditions.	85
Figure 5.6 Graph of the iteration history for the elliptic solid region with a varied step size and initial conditions.	86
Figure 5.7 Graph of the iteration history for the rectangular solid region with a varied step size and initial conditions.	87
Figure 5.8. a-c. Schematic of the optimal periodic cells obtained after optimization with the dimensions tabulated in Table (5.2).....	89
Figure 5.9 a-c. Contours of the longitudinal component of the permeability (μU_{11}) for the microstructures shown in Figure (5.8).....	94
Figure 5.10 a-c. Contours of the longitudinal component of the dispersivity (Z_{11}) for the microstructures shown in Figure (5.8).....	95
Figure 5.11 a-c. Plots of the velocity vectors in microstructure corresponding to Figure (5.8)	96
Figure 5.12 Schematic of the macroscopic layout with applied boundary conditions.....	99
Figure 5.13 Comparison of the velocity fields for a domain with a microstructure formed with the optimized elliptic cross section with the velocity field for a square array of same porosity.....	100
Figure 5.14 a-c. Comparison of solute dispersion after time $t = 0.02$ sec for the macroscopic domain formed with a microstructure of elliptic cross	

section cylinders (a) obtained from shape optimization with the microstructure obtained from a square array (b) of same porosity. The magnitude of c is shown in right (c). 102

Figure 6.1 Flowchart showing the steps of the algorithm based on topology optimization for designing microstructures. 105

Figure 6.2. Schematic of a periodic microscopic cell (Ω_m). The interface between the solid-fluid in each periodic cell is Γ_{sl} and the interface between two periodic cells is denoted by Γ_{cell} 107

Figure 6.3 Plot showing the dependence of α on q 110

Figure 6.4 Schematic of a periodic microscopic cells with a liquid zones imposed on Zone 1 above to avoid a continuous solid region between the cells. 113

Figure 6.5 Schematic of the unstructured triangular mesh used for the finite element analysis. 115

Figure 6.6 Schematic of microstructure layout for volume fraction 0.5 and with macroscopic pressure gradient of 1N/m^2 in horizontal direction.... 117

Figure 6.7 Schematic of microstructure layout for volume fraction 0.7 with macroscopic pressure gradient of 1N/m^2 in horizontal direction ... 118

Figure 6.8. Schematic of the microstructure layout for a volume fraction 0.2 with an equal macroscopic pressure gradient of 1N/m^2 in the horizontal and vertical directions. 120

Figure 6.9. Schematic of the microstructure layout obtained for a volume fraction of 0.3 with an equal macroscopic pressure gradient of 1N/m^2 in the horizontal and the vertical directions 121

Figure 6.10. Schematic of a microstructure layout for volume fraction 0.4 with equal macroscopic pressure gradient of 1N/m^2 in the horizontal and the vertical directions. 122

Figure 6.11 Schematic of the microstructure layout for a volume fraction 0.5 with equal macroscopic pressure gradients of 1N/m^2 in the horizontal and vertical directions. 123

Figure 6.12. Schematic of the microstructure layout for a volume fraction 0.6 with equal macroscopic pressure gradients of 1N/m^2 in the horizontal and vertical directions.	124
Figure 6.13 Schematic of the microstructure layout for volume fraction of 0.7 with equal macroscopic pressure gradients of 1N/m^2 in the horizontal and vertical directions.	125
Figure 6.14. Schematic of the microstructure layout for a volume fraction 0.8 with equal macroscopic pressure gradient of 1N/m^2 in the horizontal and vertical directions.	126
Figure 6.15 Schematic of the macroscopic layout with applied boundary conditions.....	129
Figure 6.16 Comparison of the velocity profiles in the macroscopic domain for a microstructure formed from a cross section obtained from topology optimization with the velocity field obtained for a square array of same porosity.....	130
Figure 7.1 Flowchart of the topology optimization methodology employed.....	133
Figure 7.2 Schematic of a periodic microscopic cell.....	135
Figure 7.3 Schematic of a periodic microscopic cells with the zones to avoid continuous solid region.....	140
Figure 7.4 Schematic of the unstructured triangular mesh used in the finite element analysis.	142
Figure 7.5 Schematic of microstructure layout for volume fraction 0.7 with equal macroscopic pressure gradient of 1N/m^2 in the horizontal and vertical directions and a concentration gradient in the horizontal direction.	144
Figure 7.6 Schematic of the microstructure layout for a volume fraction 0.3 with equal macroscopic pressure gradient of 1N/m^2 in the horizontal and vertical directions and a concentration gradient in the horizontal direction.....	145
Figure 8.1 Schematic of the process of representing a two phase flow with an equivalent a single phase flow model.	149

Figure 8.2 Schematic of a homogeneous macroscopic domain studied consisting of periodic microscopic cells.....	155
Figure 8.3 Schematic of periodic microscopic cells with an elliptic solid region.....	156
Figure 8.4 Schematic of periodic microscopic cells with a rectangular solid region.....	157
Figure 8.5 Schematic of the iteration history for a circular solid region with varied step size and initial conditions.....	161
Figure 8.6 Schematic of the iteration history for an elliptic solid region with varied step size and initial conditions.....	162
Figure 8.7 Schematic of the iteration history for a rectangular solid region with varied step size and initial conditions.....	163
Figure 8.8 a-c. Schematic of the optimal periodic cells obtained after optimization.....	164
Figure 8.9 a-c. Schematic of velocity distribution of fluid mixture for microstructures shown in Figure (8.8).....	167
Figure 8.10 a-c. Schematic of pressure distribution of fluid mixture for microstructures shown in Figure (8.8).....	168
Figure 8.11 Schematic of the macroscopic layout with applied boundary conditions.....	172
Figure 8.12. Comparison of velocity field in a macroscopic domain for microstructure form with the cross section obtained from shape optimization to minimize energy loss for multiphase flow with that formed by square arrays of the same porosity.....	173

NOMENCLATURE

a	Major axis
a	Characteristic pressure tensor
b	Minor axis
c	Volumetric concentration
$c^{(0)}, c^{(1)}, c^{(2)}, c^{(3)}$	Periodic pressure from perturbation expansion of c
d	Isotropic dispersivity
d_p	Equivalent diameter of the solid region
D	Dispersion tensor
D	Molecular diffusivity
H	Characteristic macro height
h	Characteristic micro height
I	Identity tensor
k	Isotropic permeability
K	Permeability Tensor
l	Characteristic micro length
L	Characteristic macro length
N	Periodic Vector
n	Normal vector
n	Porosity
p	Pressure
$p^{(0)}, p^{(1)}, p^{(2)}, p^{(3)}$	Periodic pressure from perturbation expansion of p
P	Characteristic pressure
Pe	Peclet number
q	Tuning parameter for penalty term
t	Time
u	Periodic velocity

$\mathbf{u}^{(0)}, \mathbf{u}^{(1)}, \mathbf{u}^{(2)}, \mathbf{u}^{(3)}$	Periodic velocity from perturbation expansion of \mathbf{u}
\mathbf{U}	Characteristics velocity tensor
\mathbf{v}	Any periodic velocity
x	Small scale
X	Large scale
X	Horizontal Coordinate
Y	Vertical Coordinate
α	Penalty term
μ	Dynamic Viscosity
Ω_M	Macroscopic domain
Ω_m	Microscopic domain
Ω_s	Solid region
Ω_f	Fluid region
ε	Length scale ratio
Γ	Boundary
\mathfrak{S}	Objective function
θ	Horizontal angle between two periodic cells
ρ	Design variable
ρ^f	Density of fluid

CHAPTER 1

INTRODUCTION

1.1 General

A porous medium is a mixture of a heterogeneous solid matrix with its void filled with fluids (Kaviany, 1991). A porous media has structural properties such as elasticity, strength and have found numerous scientific and engineering applications such as those listed in Table (1.1).

The term “porous materials” is usually reserved to materials such as ceramic, fibers, concrete, or naturally occurring porous rocks. But a broader use of the term porous media can describe a wide variety of devices or components. Figure 1.1 shows few examples of porous media such as heat exchanger (b) (Industrial Quick Search, 2007), material for micro chip (a) (H-IP-O, 2007), filters (c) (Filtration and Separation Buyers Guide, 2007), and static mixture (d) (Cleveland Eastern Mixers, 2007).

Table 1.1 List of engineering disciplines where porous materials are used. In many instances the microstructure of the porous material has a direct impact on performance.

Discipline	Usage of Porous Material
Agricultural engineering	Dealing with drainage and irrigation
Civil engineering	Concrete is a porous medium
Environmental engineering	Groundwater pollution by toxic liquids and hazardous wastes
Chemical engineering	Reactors, static mixers
Mechanical engineering	Layout of heat exchangers can be modeled as a porous media and micro channel cooling
Biomedical engineering	Bones, lungs and kidneys

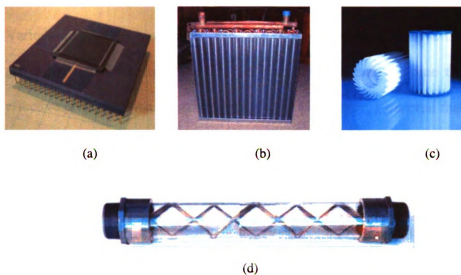


Figure 1.1. a-d. Examples of industrial applications of porous media.

1.2 Solute Transport and Fluid Flow in Porous Media

Various approaches have been presented in the literature to derive the governing equations for fluid flow in porous media and compute the effective properties. An effective property is a property of a material that changes with factors such as modification in the micro structure or the acting boundary conditions, whereas a physical property can be measured or perceived without changing its identity of the material such as viscosity, molecular diffusivity.

Some noted works to compute effective properties are self-consistent methods by Kroner (Kroner 1978), statistical modeling techniques by Kroner (Kroner 1986), averaging methods by Quintard and Whitaker (Quintard and Whitaker 1988) and the theory of homogenization by Bensoussan and Sanchez-Palencia (Bensoussan 1978, Sanchez-Palencia 1980). The last method is used in this work to derive an expression for the effective properties. Effective properties of any material are computed from solving and averaging the resulting quantity over the microstructure.

The theory of homogenization provides a rigorous treatment of multi-scale problems applicable to numerous differential equations with multi scale features. It is assumed here that there exists two length scales (micro and macro) which are very different in magnitude. When applied to derive the governing equations for porous media, the microstructure is also

assumed to be periodic at the micro scale and homogeneous at the macro scale.

1.3 Research Approach

The objective of this work is to develop methodologies for the design of the microstructure of a porous material. To achieve this, first a review of previous works done on the mechanics of single and multiphase flows and solute transport in porous media is presented. The equations derived from the theory of homogenization (Bensoussan 1978, Sanchez-Palencia 1980) are used as described by C. C. Mei (Mei 1992) and solved using various commercial software. The effective properties of the given material are computed and compared with various experimental and numerical results. The method of moving asymptotes, as proposed by K. Svanberg (Svanberg 1978, 2002), is used to find the optimal microstructure of the porous using shape and topology optimization. Figure 1.2 shows a flowchart of the research approach. Step by step algorithms were developed using shape and topology optimization to identify a microstructure for a porous media that optimizes the given set of conditions such as maximizing dispersion of the solute or minimizing energy loss for both single and multiphase flow.

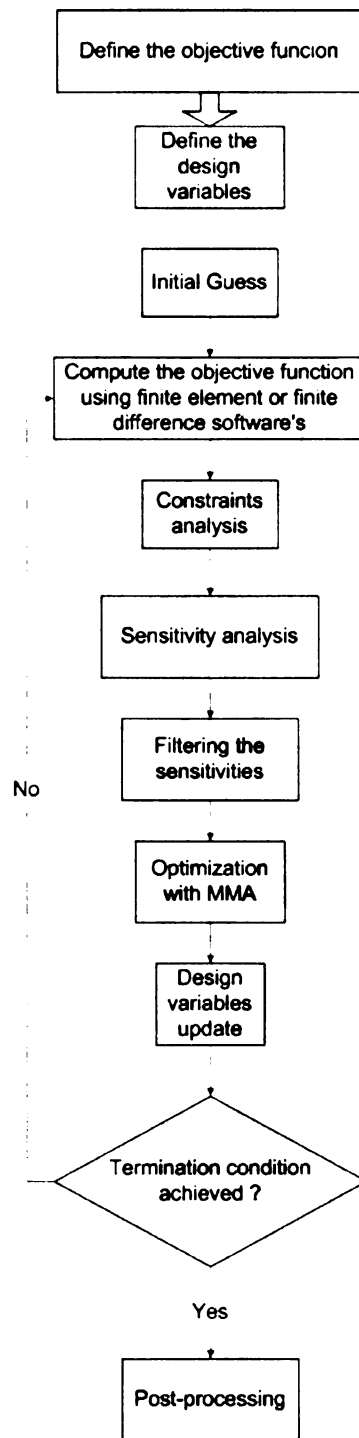


Figure 1.2 Flow chart providing an overview of the methodology.

1.4 Material design techniques

Shape and topology optimization techniques are used to determine the shape and layout of the solid region. Figure 1.3 shows examples of shape and topology optimization. Here shape optimization (Figure 1.3a) is used to find the optimal shape of the holes to avoid stress concentration under given load (Jorgen 2003, Sigmund 2000). Topology optimization (Figure 1.3b), on the other hand, is a layout optimization, which gives an optimal layout to avoid stress concentration under given load.

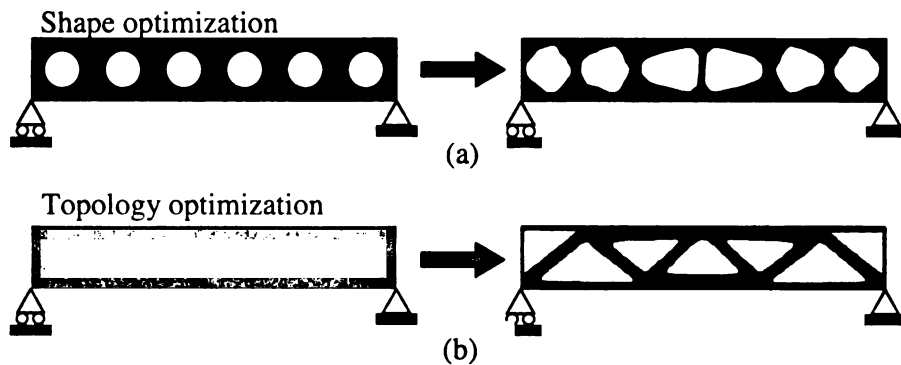


Figure 1.3. a-b. Examples of (a) shape optimization and (b) topology optimization from (Jorgen, 2003).

The algorithm for shape optimization tries to find an optimal shape from a given family of shapes, which will maximize or minimize the given objective function. The design variables are mainly the dimensions of the periodic cell and the solid region such as the radius for circular cross section, major and minor axis for elliptic cross section, and length and height for the rectangular cross section.

Topology optimization, on the other hand, mainly focuses on the layout of the fluid and the non-fluid region. The domain is divided into small domains called “pixels” and for each pixel the design variable ρ controls the local permeability of the medium as follows:

$$\rho(x) = \begin{cases} 0 & \text{if } x \in \text{Solid Region} \\ 1 & \text{if } x \in \text{Fluid Region} \end{cases} \quad (1.1)$$

For a given domain and boundary condition the algorithm tried to find the optimal layout of the solid and fluid region, which maximizes or minimizes the given objective function.

1.5 Dissertation layout

The layout of this dissertation is as follows:

In chapter 2 and 3, existing theories on fluid flow and solute transport in porous media are presented along with expressions for the effective properties of a porous material for single phase fluid flow and solute transport in porous media. The governing equations are solved using the finite element method and compared with experimental results.

Chapter 4 presents my findings for the optimal microstructures of porous media that maximizes the effective properties such as permeability and dispersivity. Shape optimization is used.

In Chapter 5 I try to find the optimal microstructure for porous media using shape optimization that maximizes dispersion while minimizing energy loss.

Topology optimization is used to find the microstructures for two objective functions: minimizing dissipation power in Chapter 6 and maximizing “dispersive power” in Chapter 7.

In chapter 8, I review the theory for multiphase flow in porous media and solve the governing equations using finite differences to find the optimal microstructure that will minimize dissipation power or energy loss for multiphase fluid flow using shape optimization. It is to be noted however that this problem is mathematically identical to the single phase flow problem as presented.

Finally, in Chapter 9 I summarize and discuss the results obtained from various optimization techniques shown in the previous chapters

CHAPTER 2

THEORY FOR SINGLE PHASE FLUID FLOW IN POROUS MEDIA

2.1 Introduction

The fluid flow in this work is assumed to be incompressible and non turbulent. The theory of homogenization, introduced by Bensoussan and Sanchez-Palencia (Bensoussan 1978, Sanchez-Palencia 1980), provides a general framework for deducing both the macro scale equations and the effective properties for the dynamics of rigid porous media. The main assumption in this theory is that there exist two well-separated length scales: the micro scale $l \approx O(x)$ and macro scale $L \approx O(X)$, where $l/L = \varepsilon \ll 1$. In this study the porous macrostructure is assumed to be homogeneous consisting of periodic micro cells having distinct solid and fluid regions. Figure (2.1) shows the microscopic length scale for different naturally found porous media.

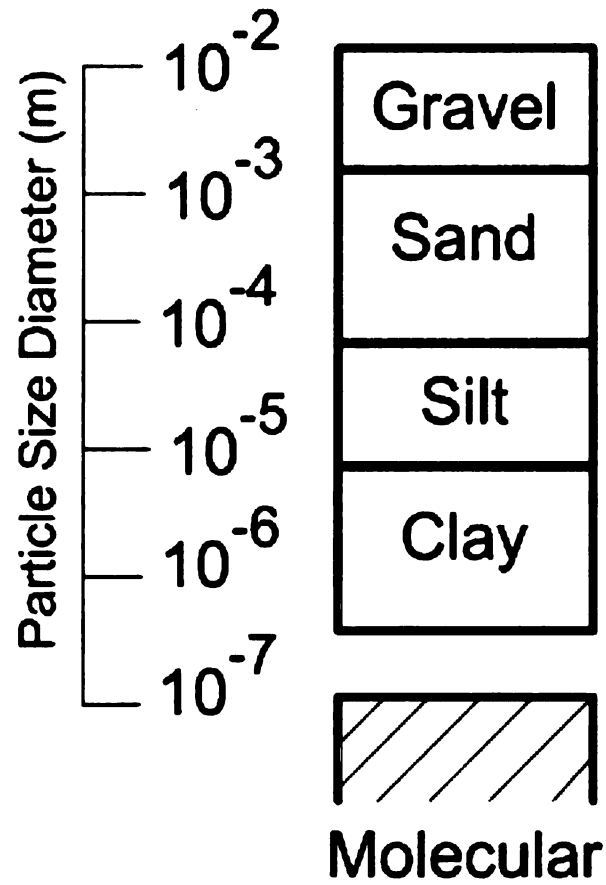


Figure 2.1 Schematic showing the particle pore diameter for porous media from (Kaviany 1991).

2.2 Derivation of Effective Permeability Tensor

The macroscopic domain (Ω_M) as shown in Figure 2.2 (a) is assumed to be homogeneous with periodic microscopic cells (Ω_m) as shown in Figure 2.2(b). The periodic cell has two distinct regions: a solid region (Ω_s) and a fluid region (Ω_f) such that $\Omega_m = \Omega_s \cup \Omega_f$ and $\Omega_s \cap \Omega_f = \emptyset$. The interface between the solid-fluid in each periodic cell is Γ_{sl} and the interface between two periodic cells is denoted by Γ_{cell} .

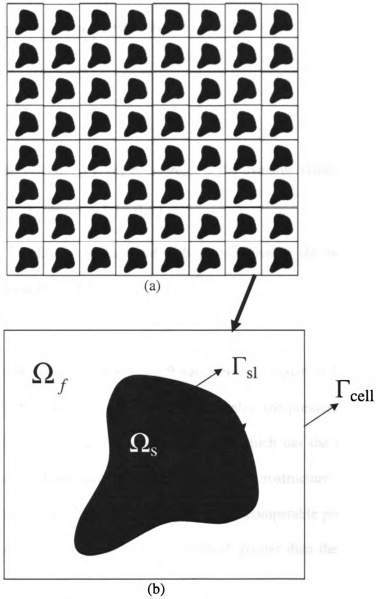


Figure 2.2. Schematic of a porous material (Ω_M) in (a) made of an assembly of periodic microscopic cells (Ω_m) (b). The interface between the solid-fluid in each periodic cell is Γ_{sl} and the interface between two periodic cells is denoted by Γ_{cell} .

For a rigid porous medium with incompressible Newtonian fluid of constant density, the governing equation for the fluid flow is Navier – Stokes equation (Mei 1991a, 1991b, 1992).

$$\mu \nabla^2 \mathbf{u} - \nabla p = \rho^f \mathbf{u} \cdot \nabla \mathbf{u} \text{ in } \Omega_f \quad (2.1)$$

$$\text{and } \nabla \cdot \mathbf{u} = 0 \text{ in } \Omega_f \quad (2.2)$$

where \mathbf{u} is the velocity, p is the pressure, μ is the dynamic viscosity of the fluid and ρ^f is the density of the fluid.

The boundary condition on the solid – fluid interface is the no slip boundary condition given by

$$\mathbf{u} = 0 \text{ on } \Gamma_{sl} \quad (2.3)$$

For a low Reynolds number flow, the left hand terms in equation 2.1 are equally important. Since there are two different scales, the pressure term has two contributions: the global applied pressure which has the length scale L and the local pressure variation due to the microstructure which has the length scale l . For generality, let there be two comparable pressure gradients. Then the global pressure must be much greater than the local pressure by the factor $O(1/\epsilon)$. These two pressure variations are referred as the driving pressure (global) and responding pressure (local) (Mei, 1992).

The multiple scale coordinates x (small scale) and X ($x=\epsilon X$ where X is the large scale) are introduced to relate the micro and macro length scale

respectively. In order to relate the vector and scalar quantities at different scales, asymptotic expansions for \mathbf{u} and p are used as follows

$$\mathbf{u} = \mathbf{u}^{(0)} + \varepsilon \mathbf{u}^{(1)} + \varepsilon^2 \mathbf{u}^{(2)} + \varepsilon^3 \mathbf{u}^{(3)} + \dots \quad (2.4)$$

$$p = p^{(0)} + \varepsilon p^{(1)} + \varepsilon^2 p^{(2)} + \varepsilon^3 p^{(3)} + \dots \quad (2.5)$$

where $\mathbf{u}^{(0)}, \mathbf{u}^{(1)}, \mathbf{u}^{(2)} \dots$ and $p^{(0)}, p^{(1)}, p^{(2)} \dots$ are Ω_m -periodic and ε is

small parameter (the ratio of the small scale over the large scale). The

superscripts $^{(0)}, ^{(1)} \dots$ denote terms associated with a corresponding power

of ε , i.e. $\varepsilon^0, \varepsilon^1 \dots$ in the asymptotic expansions. The gradient operator

related the two length scales as a function of ε is given as (Mei, 1995)

$$\nabla = \nabla_x + \varepsilon \nabla_X \quad (2.6)$$

where the subscripts x and X represent the small and large scales respectively.

Substituting the gradient operator and the perturbation expansions for \mathbf{u} and p in the Navier-Stokes equation and the incompressibility constraint, then

$$\begin{aligned} & \mu \left(\nabla_x + \varepsilon \nabla_X \right)^2 \left(\mathbf{u}^{(0)} + \varepsilon \mathbf{u}^{(1)} + \varepsilon^2 \mathbf{u}^{(2)} + \varepsilon^3 \mathbf{u}^{(3)} + \dots \right) - \\ & \left(\nabla_x + \varepsilon \nabla_X \right) \left(p^{(0)} + \varepsilon p^{(1)} + \varepsilon^2 p^{(2)} + \varepsilon^3 p^{(3)} + \dots \right) = \\ & \rho \left(\mathbf{u}^{(0)} + \varepsilon \mathbf{u}^{(1)} + \varepsilon^2 \mathbf{u}^{(2)} + \varepsilon^3 \mathbf{u}^{(3)} + \dots \right) \left(\nabla_x + \varepsilon \nabla_X \right) \\ & \left(\mathbf{u}^{(0)} + \varepsilon \mathbf{u}^{(1)} + \varepsilon^2 \mathbf{u}^{(2)} + \varepsilon^3 \mathbf{u}^{(3)} \right) \text{ in } \Omega_f \end{aligned} \quad (2.7)$$

$$\text{and } \left(\nabla_x + \varepsilon \nabla_X \right) \cdot \left(\mathbf{u}^{(0)} + \varepsilon \mathbf{u}^{(1)} + \varepsilon^2 \mathbf{u}^{(2)} + \varepsilon^3 \mathbf{u}^{(3)} + \dots \right) = 0 \text{ in } \quad (2.8)$$

Ω_f

From equation 2.7 and 2.8, keeping terms of $O(\varepsilon^0)$ then the following problem is identified

$$\mu \nabla_x^2 \mathbf{u}^{(0)} - \nabla_x p^{(1)} = \nabla_X p^{(0)} \text{ in } \Omega_f \quad (2.9)$$

$$\text{and } \nabla_x \cdot \mathbf{u}^{(0)} = 0 \text{ in } \Omega_f \quad (2.10)$$

In Equation (2.9) $p^{(0)}$ is the global pressure applied in the macroscopic scale, whereas $p^{(1)}$ is the local pressure and varies in microscale only.

The needed no slip boundary conditions are derived by substituting the asymptotic expansion of \mathbf{u} in equation (2.3) as

$$\mathbf{u}^{(0)} = \mathbf{u}^{(1)} = \dots = 0 \text{ on } \Gamma \text{ (solid fluid interface),} \quad (2.11)$$

$$\mathbf{u}^{(0)}, \mathbf{u}^{(1)} \dots \text{ and } p^{(0)}, p^{(1)} \dots \text{ are } \Omega_m \text{-periodic.} \quad (2.12)$$

$\mathbf{u}^{(0)}, p^{(1)}$ and $p^{(0)}$ can be written in dimensionless form $\hat{\mathbf{u}}^{(0)}, \hat{p}^{(1)}$

and $\hat{p}^{(0)}$ related by $\hat{\mathbf{u}}^{(0)} = \mathbf{u}^{(0)} / \langle \mathbf{u}^{(0)} \rangle, \hat{p}^{(1)} = p^{(1)} / P$ and

$\hat{p}^{(0)} = p^{(0)} / P$, where P is the characteristics pressure. The length scale x and X are scaled with characteristic macroscopic length L . Equations (2.9) and (2.10) can be written in dimensionless form as follows,

$$\left(\frac{\mu \langle \mathbf{u}^{(0)} \rangle}{PL} \right) \nabla_x^2 \hat{\mathbf{u}}^{(0)} - \nabla_x \hat{p}^{(1)} = \nabla_X \hat{p}^{(0)} \text{ in } \Omega_f \quad (2.13)$$

$$\text{and } \nabla_x \cdot \hat{\mathbf{u}}^{(0)} = 0 \text{ in } \Omega_f \quad (2.14)$$

where $\left(\frac{\mu \langle \mathbf{u}^{(0)} \rangle}{PL} \right)$ is a dimensionless number.

Equation (2.9) relates the microscopic fluid flow with the macroscopic pressure gradient. The two terms on the left hand side of equation (2.9) are depended on the small scale where as the right hand side term $\nabla_X p^{(0)}$ is a function of large scale. Assuming that $\mathbf{u}^{(0)}$ and $p^{(1)}$ depends on the large scale pressure gradient, $\mathbf{u}^{(0)}$ and $p^{(1)}$ can also be expressed in terms of $p^{(0)}$ from Darcy's equation as described by (Benssoussan et al, 1977, and Mei 1991a)

$$\mathbf{u}^{(0)} = -\mathbf{U} \cdot \nabla_X p^{(0)} \text{ in } \Omega_f \quad (2.15)$$

And

$$p^{(1)} = \mathbf{a} \cdot \nabla_X p^{(0)} \text{ in } \Omega_f \quad (2.16)$$

where \mathbf{U} is the characteristic velocity tensor and \mathbf{a} is the characteristics pressure tensor obtained from the solution of

$$\mu \nabla_x^2 \mathbf{U} - \nabla_x \mathbf{a} = \mathbf{I} \text{ in } \Omega_f \quad (2.17)$$

and

$$\nabla_x \cdot \mathbf{U} = 0 \text{ in } \Omega_f \quad (2.18)$$

The domain is the periodic cell and the boundary conditions applied are no slip condition at the solid liquid interface and periodic boundary conditions for \mathbf{U} and \mathbf{a} on Ω_f . \mathbf{U} and \mathbf{a} in dimensionless form can be written as $\hat{\mathbf{U}}$ and $\hat{\mathbf{a}}$ related by $\hat{\mathbf{U}} = \mathbf{U} / (L^2 / \mu)$ and $\hat{\mathbf{a}} = \mathbf{a} / L$, where L is the characteristic macroscopic length. The length scale x and X are scaled with characteristic macroscopic length L .

$$\nabla_x^2 \hat{\mathbf{U}} - \nabla_x \hat{\mathbf{a}} = \mathbf{I} \text{ in } \Omega_m \quad (2.19)$$

and

$$\nabla_x \cdot \hat{\mathbf{U}} = 0 \text{ in } \Omega_m \quad (2.20)$$

The effective permeability of the porous media is computed from

$$\mathbf{K} = \mu \langle \mathbf{U} \rangle \text{ in } \Omega_M \quad (2.21)$$

where the averaging operator is defined as

$$\langle \mathbf{f} \rangle = \frac{1}{\Omega_m} \int_{\Omega_f} \mathbf{f} d\Omega_m \quad (2.22)$$

and in dimensionless form,

$$\hat{\mathbf{K}} = \langle \hat{\mathbf{U}} \rangle \text{ in } \Omega_M \quad (2.23)$$

Equations (2.8 - 2.9) and Equations (2.19 – 2.20) are similar yet different in many ways. In Equations (2.8 - 2.9) the solution for $\mathbf{u}^{(0)}$ depends on the boundary conditions applied on the macroscale (macroscopic pressure gradient) and the microstructure whereas \mathbf{U} is independent of the macroscopic boundary conditions. Also for a computed value of \mathbf{U} , $\mathbf{u}^{(0)}$ can be computed from equation (2.16). It is convenient and computationally faster to solve equations (2.8 – 2.9) when flow parameters such as $\mathbf{u}^{(0)}$ and $p^{(1)}$ are of primary focus. On the other hand if one needs to compute the effective permeability it is convenient to solve Equations (2.19-2.20) as shown below.

2.3 Computation of Effective Permeability Tensor

In this section, the commercial software Comsol[®] is used to solve the characteristic velocity equations (2.20) and (2.21), for a given microstructure of dimension 0.002m with circular solid region of radius 0.00062m. The domain was discretized using unstructured triangular mesh with an average element size of $4e^{-5}$ and is shown much further below in Figure 4.2. The physical properties of the fluid are taken as dynamic viscosity μ to be 0.001 Pa.s, density of fluid ρ^f to be 1000 Kg/m^3 . The effective permeability is computed from Equation (2.22).

Figure 2.3 shows the longitudinal permeability for a square microstructure in m^2 . The effective permeability computed for the microstructures shown in Figure 2.3 is $\mathbf{K} = 3.9(10^{-5}) \begin{bmatrix} 1 & \varepsilon_c \\ \varepsilon_c & 1 \end{bmatrix} m^2$,

where $\varepsilon_c = 4.07(10^{-3})$. When compared with the intrinsic permeability calculated from Kozeny-Carmen equation (Bird et al. 2001), the results are in reasonable argument. The intrinsic permeability is given by the Kozeny – Carmen equation is given as

$$k_{kc} = \frac{n^2}{2s^3} \quad (2.24)$$

where n is the porosity and s is the specific surface which is expressed as the ratio of the pore surface area to the total volume of the periodic cell. From Equation (2.24) the intrinsic permeability computed for the microstructure mentioned above is $k_{kc} = 1.78(10^{-12}) m^2$. Permeability is related to the intrinsic permeability not only on the viscosity but also on the density of the fluid at the temperature of measurement by $k_{kc} = \frac{K\mu}{\rho^f g}$.

From the above equation the permeability if computed as $k_{kc} = 1.75(10^{-5}) m^2$ which is comparable with the results obtained using Equations 2.20 and 2.21. Since the axial velocity is directly proportional to the longitudinal permeability, Figure 2.3 also shows the contour for axial velocity for an applied pressure.

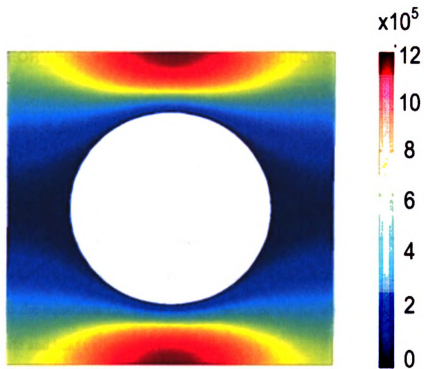


Figure 2.3 Contour plot of the distribution of the longitudinal component of the permeability tensor (μU) for round cylinder in a square periodic domain. The results are presented in m^2 .

CHAPTER 3

THEORY FOR SOLUTE TRANSFER IN POROUS MEDIA

3.1 Introduction

In many applications of porous media such as static mixers (solute transport), heat exchanger (heat transport), material for microchip (heat transfer), the dispersion of a solute or heat transfer is of critical importance. Since the governing equations for solute transport are often similar to the equations for heat transfer, the scope of the work applies to both solute and heat transport in porous media.

In this chapter, the governing equation for dispersion of solute in porous media are presented using the theory of homogenization. As discussed in the previous chapters, the theory of homogenization, as introduced by Bensoussan et al. and Sanchez-Palencia (Bensoussan et al. 1978, Sanchez-Palencia 1980), provides a general scheme for deducing both the macro scale equations and the effective properties for the dynamics of rigid porous media.

3.2 Derivation of Effective Dispersion Tensor

In the analysis below, the macroscopic domain (Ω_M) as shown in Figure 3.1 (a) is assumed to be homogeneous with periodic microscopic cells

(Ω_m) as shown in Figure 3.1(b). The periodic cell has two distinct regions: a solid region (Ω_s) and a fluid region (Ω_f) such that $\Omega_m = \Omega_s \cup \Omega_f$ and $\Omega_s \cap \Omega_f = \emptyset$. The interface between the solid-fluid in each periodic cell is Γ_{sf} and the interface between two periodic cells is denoted by Γ_{cell} .

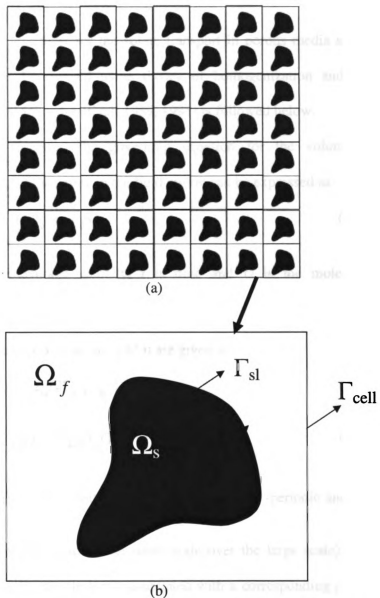


Figure 3.1. Schematic of macrostructure (Ω_M) (a) consisting of periodic microscopic cells (Ω_m) (b). The interface between the solid-fluid in each periodic cell is Γ_{sl} and the interface between two periodic cells is denoted by Γ_{cell} .

The governing equations for the solute transport in porous media at the macroscale can be derived using theory of homogenization and the presentation of (Mei and Auriault 1989, 1991) is followed below.

For solute transfer, the governing equation for the volumetric concentration c of the solute in the fluid region can be expressed as

$$\frac{\partial c}{\partial t} + \langle \mathbf{u} \rangle \cdot \nabla c = \nabla \cdot [D \cdot \nabla c] \text{ in } \Omega_f \quad (3.1)$$

where $\langle \mathbf{u} \rangle$ the average velocity, t is time and D is the molecular diffusivity of the fluid.

The asymptotic expansions for c and \mathbf{u} are given as

$$\mathbf{u} = \mathbf{u}^{(0)} + \varepsilon \mathbf{u}^{(1)} + \varepsilon^2 \mathbf{u}^{(2)} + \varepsilon^3 \mathbf{u}^{(3)} + \dots \quad (3.2)$$

$$c = c^{(0)} + \varepsilon c^{(1)} + \varepsilon^2 c^{(2)} + \varepsilon^3 c^{(3)} + \dots \quad (3.3)$$

where $\mathbf{u}^{(0)}, \mathbf{u}^{(1)}, \mathbf{u}^{(2)} \dots$ and $c^{(0)}, c^{(1)}, c^{(2)} \dots$ are Ω_m -periodic and ε is

small parameter (the ratio of the small scale over the large scale). The superscripts $^{(0)}, ^{(1)} \dots$ denote terms associated with a corresponding power of ε , i.e. $\varepsilon^0, \varepsilon^1 \dots$ in the asymptotic expansions. The gradient operator in terms of the two length scales is

$$\nabla = \nabla_x + \varepsilon \nabla_X \quad (3.4)$$

where the subscripts x and X represent the small and large scales respectively.

Substituting the differential term and expansion for c and \mathbf{u} in volumetric concentration equation,

$$\begin{aligned} & \frac{\partial \left(c^{(0)} + \varepsilon c^{(1)} + \varepsilon^2 c^{(2)} + \varepsilon^3 c^{(3)} + \dots \right)}{\partial t} + \\ & \left\langle \left(\mathbf{u}^{(0)} + \varepsilon \mathbf{u}^{(1)} + \varepsilon^2 \mathbf{u}^{(2)} + \varepsilon^3 \mathbf{u}^{(3)} + \dots \right) \cdot \left(\nabla_x + \varepsilon \nabla_X \right) \right. \\ & \left. \left(c^{(0)} + \varepsilon c^{(1)} + \varepsilon^2 c^{(2)} + \varepsilon^3 c^{(3)} + \dots \right) = \left(\nabla_x + \varepsilon \nabla_X \right) \cdot \right. \\ & \left. \left[D \cdot \left(\nabla_x + \varepsilon \nabla_X \right) \left(c^{(0)} + \varepsilon c^{(1)} + \varepsilon^2 c^{(2)} + \varepsilon^3 c^{(3)} + \dots \right) \right] \text{ in } \Omega_f \end{aligned} \quad (3.5)$$

Equating the terms at orders from $O(\varepsilon^0)$ and $O(\varepsilon^1)$ for steady state condition, then a zeroth and first order problems can be identified

$$O(\varepsilon^0): \quad \mathbf{u}^{(0)} \nabla_x c^{(0)} = D \nabla_x^2 c^{(0)} \quad (3.6)$$

$$\begin{aligned} O(\varepsilon^1): \quad & \mathbf{u}^{(0)} \nabla_x c^{(1)} + \mathbf{u}^{(1)} \nabla_x c^{(0)} + \mathbf{u}^{(0)} \nabla_X c^{(0)} = \\ & D \nabla_x \left(\nabla_x c^{(1)} + \nabla_X c^{(0)} \right) \end{aligned} \quad (3.7)$$

Following (Mei and Auriault 1989, 1991) $c^{(1)}$ can be expressed as a function of the macroscopic gradient of $c^{(0)}$ with the proportionality function \mathbf{N} as

$$c^{(1)} = -\mathbf{N} \cdot \nabla_x c^{(0)} \text{ in } \Omega_m \quad (3.8)$$

\mathbf{N} is further described as any periodic vector satisfying the following equations

$$\nabla_x \left(D(\mathbf{I} + \nabla_x \cdot \mathbf{N}) \right) - \mathbf{u}^{(0)} \nabla_x \cdot \mathbf{N} = \mathbf{u}^{(0)} - \langle \mathbf{u}^{(0)} \rangle / n \quad \text{in } \Omega_m \quad (3.9)$$

where n is the porosity, and

$$(\mathbf{I} + \nabla_x \cdot \mathbf{N}) \cdot \mathbf{n} = 0 \quad \text{on } \Gamma. \quad (3.10)$$

\mathbf{N} is Ω_m -periodic and $\langle \mathbf{N} \rangle = 0$.

From Equation (3.9) it becomes clear that \mathbf{N} depends on the fluctuating component of $\mathbf{u}^{(0)}$ ($\mathbf{u}^{(0)} - \langle \mathbf{u}^{(0)} \rangle / n$). Substituting the expression for $c^{(1)}$

from Equation (3.8) in Equation (3.7) and reorganizing the terms, then

$$\langle \mathbf{u} \rangle \cdot \nabla_X c^{(0)} = \nabla_X \cdot [\mathbf{D} \cdot \nabla_X c^{(0)}] \quad \text{in } \Omega_M \quad (3.11)$$

where $\langle \mathbf{u} \rangle = \langle \mathbf{u}^{(0)} \rangle + \langle \mathbf{u}^{(1)} \rangle$ and for weak inertia flow (where the

inertial force term is negligible) $\langle \mathbf{u}^{(1)} \rangle \approx 0$ (Mei and Auriault 1991). The solution for $c^{(0)}$ is obtained by solving the macroscopic problem.

\mathbf{D} is the effective dispersion tensor (Mei 1992) expressed as

$$\mathbf{D} = D \langle \mathbf{Z} \rangle \quad \text{in } \Omega_m \quad (3.12)$$

where \mathbf{Z} is “characteristic dispersivity tensor” given as,

$$\mathbf{Z} = \left(\frac{1}{2} \left(\nabla_x \mathbf{N} + \nabla_x \mathbf{N}^T \right) + \mathbf{I} \right) - \frac{1}{2} \left(\left(\mathbf{u}^{(0)} \mathbf{N} \right) + \left(\mathbf{u}^{(0)} \mathbf{N} \right)^T \right) \quad \text{in } \Omega_m \quad (3.13)$$

The domain for \mathbf{Z} is the periodic cell and the boundary conditions are that of no slip on Γ_{sl} and on the outer boundary $\partial\Omega_m$ of an Ω_m -cell, the

boundary condition is

$$\mathbf{n} \cdot \left(\nabla_X c^{(l-1)} + \nabla_X c^{(l)} \right) = 0 \text{ on } \Gamma_m, \quad (3.14)$$

where l is an integer used to represent the relevant scales, and $C^{(-1)} = 0$ and $C^{(l)}$ is Ω_m -periodic and the vector \mathbf{n} denotes the normal vector to Γ_m .

$c^{(0)}$, \mathbf{u} and \mathbf{D} can be written in dimensionless form $\hat{c}^{(0)}$, $\hat{\mathbf{u}}$ and $\hat{\mathbf{D}}$ related by $\hat{c}^{(0)} = c^{(0)}/C$, $\hat{\mathbf{u}} = \mathbf{u}/\langle \mathbf{u}^{(0)} \rangle$ and $\hat{\mathbf{D}} = \mathbf{D}/D$. Equation (3.10) can

be written in dimensionless form as

$$\left(\frac{\langle \mathbf{u}^{(0)} \rangle_L}{D} \right) \langle \hat{\mathbf{u}} \rangle \cdot \nabla_X \hat{c}^{(0)} = \nabla_X \cdot \left[\hat{\mathbf{D}} \cdot \nabla_X \hat{c}^{(0)} \right] \text{ in } \Omega_M \quad (3.15)$$

where $\left(\frac{\langle \mathbf{u}^{(0)} \rangle_L}{D} \right)$ is a dimensionless number.

It can be noted that in equation (3.11) the volumetric concentration equation is expressed over the macroscopic domain whereas the terms in the dispersion is defined in the microscopic domain. Hence it can be said that the solute transport in the macroscopic domain strongly depends on the microstructure of the porous media.

3.3 Computation of Effective Dispersion Tensor

In this work, the commercial software Comsol[®] is used to solve using finite elements the effective dispersion tensor given by Equation (3.11) for given boundary conditions and geometry as shown in Table (3.1) and Figure (3.2).

In the following examples, l ($h = l$) is the length of the microscopic cell and L ($H=L$) is the macro-scale domain length. The fluid properties are the viscosity μ and density ρ^f . A macroscopic pressure gradient is applied along the horizontal direction. Each periodic cell is identified by the geometric parameters such as l , h , a , b , and θ where l is the cell length, h is the cell height, a is the major axis or length of the solid region, b is the minor axis or height of the solid region, and θ is the angle between l and h in each cell.

Examples shown in this section limits θ to 90° to represent a square array. Given the physical properties and the values of a and b (major and minor axis), equation (3.11) is solved to obtain the effective dispersion tensor. The longitudinal (along the flow direction) effective dispersion tensor (D_{xx}) for two-dimensional, spatially periodic, arrays of circular cylinders is calculated over a range of Péclet number.

The Péclet number is a dimensionless number which relates the rate of advection of a flow to its rate of solute or mass diffusion or thermal diffusion. For thermal diffusion it is equivalent to the product of the

Reynolds number with the Prandtl number, and the product of the Reynolds number with the Schmidt number in the case of mass diffusion.

For mass diffusion Péclet number can be computed from

$$Pe = \frac{\langle \mathbf{u} \rangle d_p}{D} \frac{n}{1-n}, \quad (3.6)$$

where d_p is the “equivalent particle” diameter, $\langle \mathbf{u} \rangle$ is the intrinsic volume average velocity in the direction of the pressure field, n is the porosity. For thermal diffusion the molecular diffusivity term D is replaced by thermal diffusivity. The longitudinal effective dispersion tensor calculated using homogenization method is compared with experimental (data taken from Buyuktas 2003) and numerical (Edward 1991) results and shown in Figures (3.3) and (3.4).

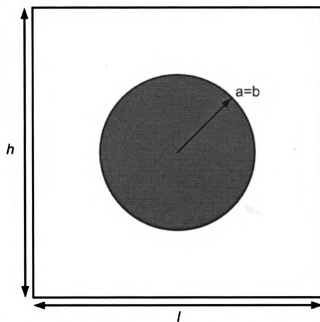


Figure 3.2 Schematic of a periodic microscopic cells. Dimensions of a , b , l , h are tabulated in Table (3.2) for a typical cells. “ a ” is the only parameter used in the optimization of a cylinder.

Table 3.1 Parameters corresponding to the geometry shown in Figure (3.2) and which are used in the solution of the dispersion tensor

Symbol	Value	Unit
l/h	1	[-]
l/L	0.002	[-]
a/b	1	[-]
n	0.8 and 0.4	[-]
$\Delta P / L$	1	Nm^{-3}
η	0.001	Pa-s
L	1	m

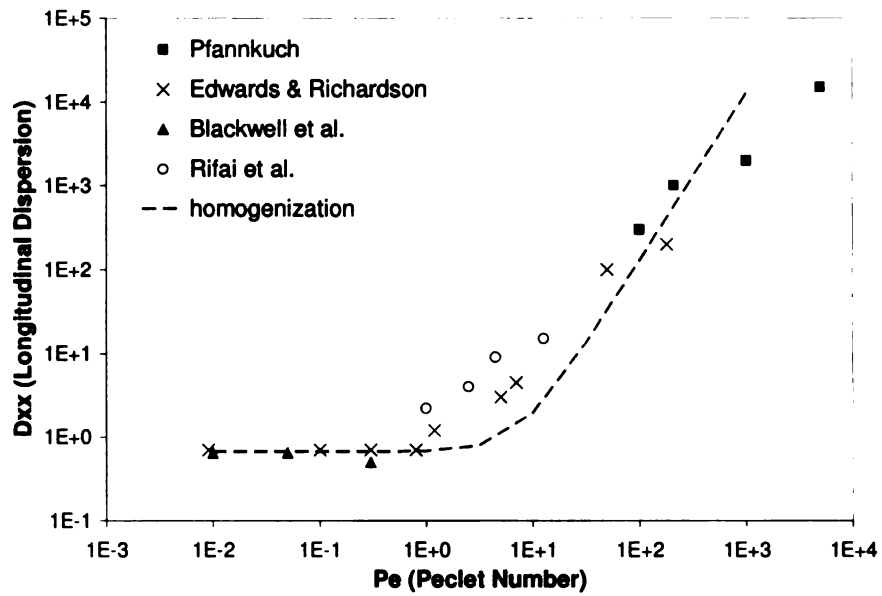


Figure 3.3 Comparison of dimensionless longitudinal effective dispersion tensor measured through experiments (data taken from Buyuktas and Wallender 2004) with numerical results obtained in this work using homogenization for a porosity of 0.8.

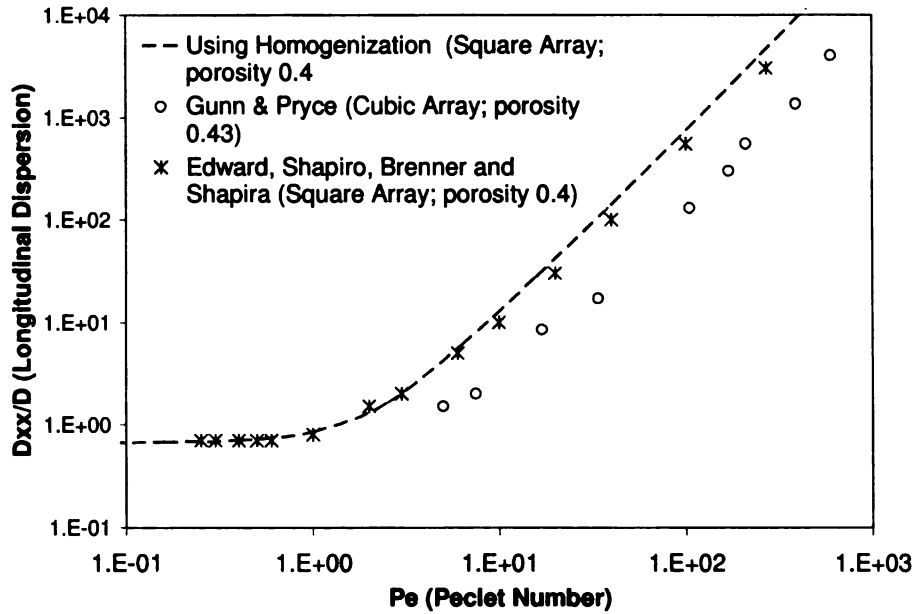


Figure 3.4 Comparison of dimensionless longitudinal effective dispersion tensor measured through experiments for a cubic array of a porosity 0.43 (Gunn and Pryce 1969) and numerical simulations obtained with square array of particles of porosity 0.4 (Edwards et al. 1991) with results obtained in this work using homogenization.

Figure (3.3) shows the relative agreement of the results obtained using homogenization method with various experimental results. Discrepancies with the experimental results are attributed to the fact that the experiments were done with disordered particles; whereas, this work is done using an array of particles equally spaced with periodic boundary condition. Also in homogenization, it is assumed that the Peclet number is of the order of 1 (low Reynolds number flow); and, hence, some significant variations with experimental results for higher Peclet number are expected.

This can be further compared with the numerical analysis based on Taylor dispersion theory as shown in Figure (3.4). In Figure (3.4), some discrepancies are observed with the experimental data (Gunn 1969). The disagreement between the present result and those of the experiments is due to the fact that their data from the experiments are for a three-dimensional cubic array; whereas, the present work is for two-dimensional, spatially periodic arrays of circular cylinders.

From the above comparison it appears that homogenization provides very reasonable values for the dispersion tensor for a Peclet number of order one.

CHAPTER 4

DESIGN OF POROUS MEDIA USING SHAPE OPTIMIZATION TO OPTIMIZE EFFECTIVE PROPERTIES

4.1 Introduction

Shape optimization is a well established method for design. Here the problem is applied to material design and posed in such a manner that the algorithm may find an optimal shape of the pores in the microstructure that will optimize the effective properties. The optimization problem is cast in the fashion of a standard shape optimization problem where various shapes described parametrically are studied. The Method of Moving Asymptotes as proposed by Krister Svanberg is used for optimization.. The derivatives of the objective function with respect to the design variables were computed using finite difference. The governing equations needed to solve the effective properties were derived in Chapters three and four and are solved using the finite element method.

4.2 Identifying the Periodic Cell

In the analysis, the macroscopic domain (Ω_M) is assumed to be homogeneous with periodic microscopic cells (Ω_m). The microscopic cell has two distinct regions: a solid region (Ω_s) and a fluid region (Ω_f)

such that $\Omega_m = \Omega_s \cup \Omega_f$ and $\Omega_s \cap \Omega_f = 0$. P , l and L are the characteristic pressure, micro length and macro length scales. Two scales are introduced: a small scale ($x \approx O(l)$) and a large scale ($X \approx O(L)$). Both scales are related by $X = x/\varepsilon$.

The homogeneous macroscopic domain shown in Figure (4.1) is formed of periodic microscopic cells as shown in Figure (4.2) and Figure (4.3). Each cell geometry is identified by the following parameters: l , h , a , b , and θ . l is the cell length, h is the cell height, a is the major axis or length of the solid region, b is the minor axis or height of the solid region, and θ is the angle between l and h in each cell. Three different shapes for the solid region such as circle ($a = b$), ellipse (Figure (4.2)), and rectangle (Figure (4.3)) are considered below.

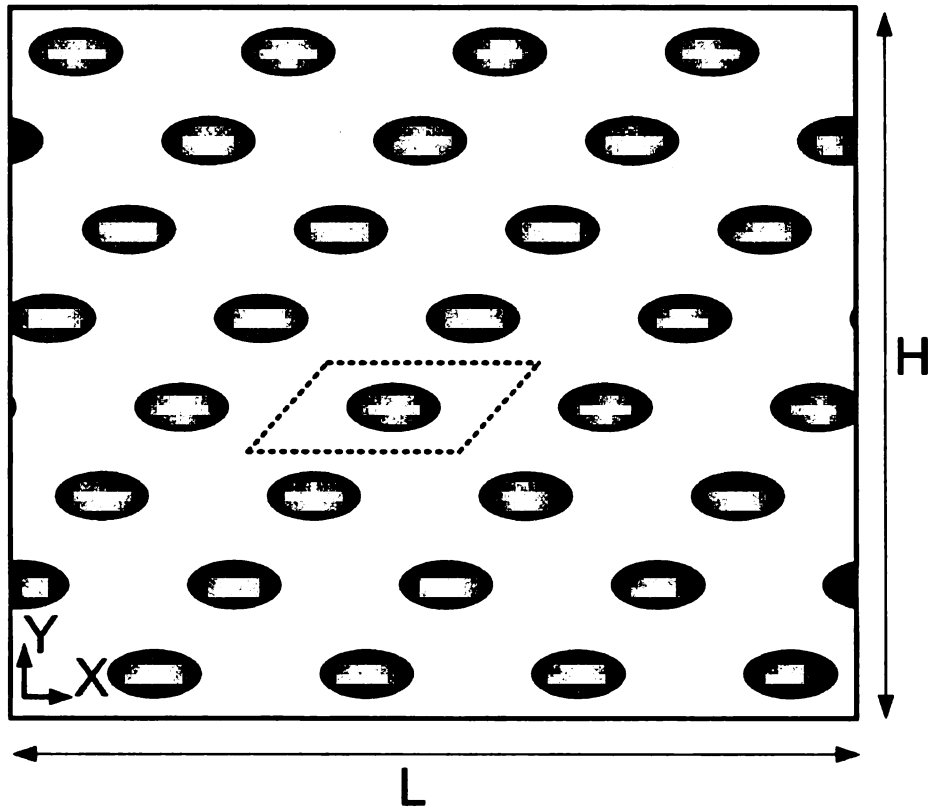


Figure 4.1 Schematic of of the arrangement of the cells in the macroscopic domain studied consisting of periodic microscopic cells as shown in dashed line.

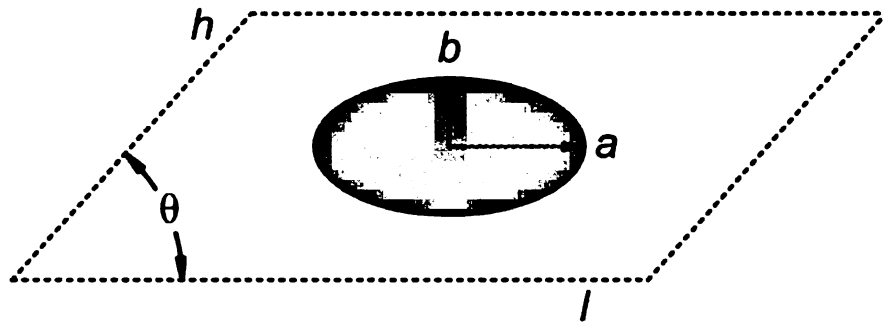


Figure 4.2 Schematic of periodic microscopic cells with an elliptic solid region.

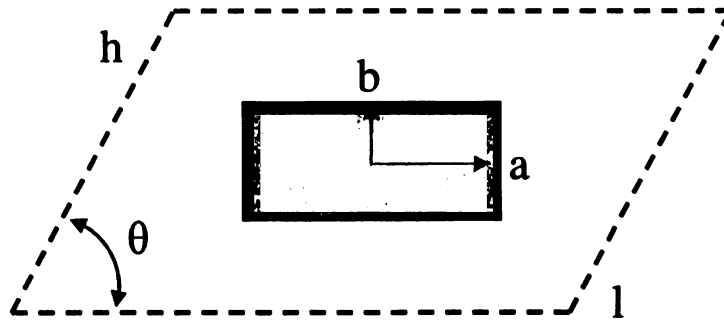


Figure 4.3 Schematic of periodic microscopic cells formed from a rectangular solid region

4.3 Formulation of the optimization problem

The aim is to find a microstructure of the periodic cell that maximizes some function of the effective properties with the added constraint of volume fraction using shape optimization. In the following section, the objectives functions are presented.

4.3.1 Maximize effective permeability

Filters constitute of the common applications of porous. It is common in such an application to be concerned with the pressure drop across the filter media. Hence the motivation behind the work in this section is to design a porous media that maximize the permeability for a given porosity or volume fraction of solid i.e. to seek a periodic cell that maximizes the permeability with isotropic flow symmetry as proposed by Guest (Guest 2007) for a given porosity or volume fraction of solid. The microstructure is modified such that the fluid in a porous media only flows in the direction of the applied pressure gradient, and hence follows a reduction in the loss of energy in fluid flow.

The isotropic effective permeability is defined as

$$k\mathbf{I} = \mathbf{K} \text{ in } \Omega_m \quad (4.1)$$

The complete formulation of the optimization problem is stated as follows:

Find the optimal value of θ , l , a and b for a g fixed of h , that will

maximize: Isotropic Effective Permeability

where isotropic permeability is expressed as $k - \varepsilon_p$

Here k and ε_p are computed from

$$k = \frac{1}{2} \sum_{i=1}^2 K_{ii} \quad (4.2)$$

and

$$\varepsilon_p = \left(\frac{1}{k}\right)^2 \left(\sum_{i=1}^2 \left(K_{ii} - K_{(i+1)(i+1)} \right)^2 + \sum_{i=1}^2 \sum_{j=2}^1 \left(K_{ij} \right)^2 \right) \quad (4.3)$$

where K_{ij} is computed from equations (2.18).

subjected to: volumetric and geometric constraints

$$\text{Constraint 1: } \frac{\Omega_s}{\Omega_m} \geq V_{frac} \quad (4.4)$$

$$\text{Constraint 2: } a < \frac{l}{2}$$

$$\text{Constraint 3: } b < \frac{h \sin \theta}{2}$$

where Ω_s is the volume of the solid region, Ω_m is the total volume of the cell, and V_{frac} is value ($0 < V_{frac} < 1$) specifying the minimum solid volume.

The first constraint in equation (4.4) restricts the minimum volume of solid region to V_{frac} . The next two constraints are imposed to insure the continuity of each phase.

4.3.1.1 Example Problems

This section shows examples of shape optimization that maximizes effective permeability as described in section 4.3.1. The solutions were obtained by casting the problem in the fashion of a standard shape optimization problem. The derivatives of the objective function with respect to the design variables were computed using a forward finite difference method as shown below,

$$\frac{\partial \text{Obj}}{\partial \text{dv}} = \frac{\text{Obj}_{\text{dv} + \delta \text{dv}} - \text{Obj}_{\text{dv}}}{\delta \text{dv}} \quad (4.5)$$

where “Obj” is the objective function and “dv” is the design variable. The derivatives of the constraints with respect to the design variables were computed analytically. The objective function was computed by solving the governing equations for the effective properties using the finite element method. The domain was discretized using approximately 6000 triangular elements in an unstructured mesh with an element size of $4e^{-5}$ m as shown in Figure (4.4).

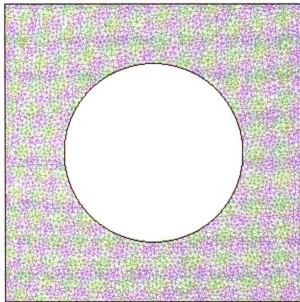


Figure 4.4 Schematic of the unstructured triangular mesh used for finite element analysis.

The Method of Moving Asymptotes (MMA) is used for optimization. The results shown in this section are all for a limiting volume fraction of 0.3 and fixed value of 0.002 m for h . The physical properties of the fluid are taken as dynamic viscosity μ to be 0.001 Pa.s, density of fluid ρ^f to be 1000 Kg/m³. The dependence of the step size and initial conditions in the optimization algorithm were verified by varying it for two different cases. For case 1 the step size is set to 0.1 and an initial aspect ratio is 1, radius (major axis, minor axis) set to 5×10^{-4} m and θ value to 90°. For case 2 the step size is set to 0.5 and an initial aspect ratio is 1 (fixed height of 0.002m), radius (or major axis, minor axis) set to 7×10^{-4} m, and θ value to 90°. The iteration history for the different cases are shown in Figure (4.5 – 4.7) for circular, elliptic and rectangular solid regions.

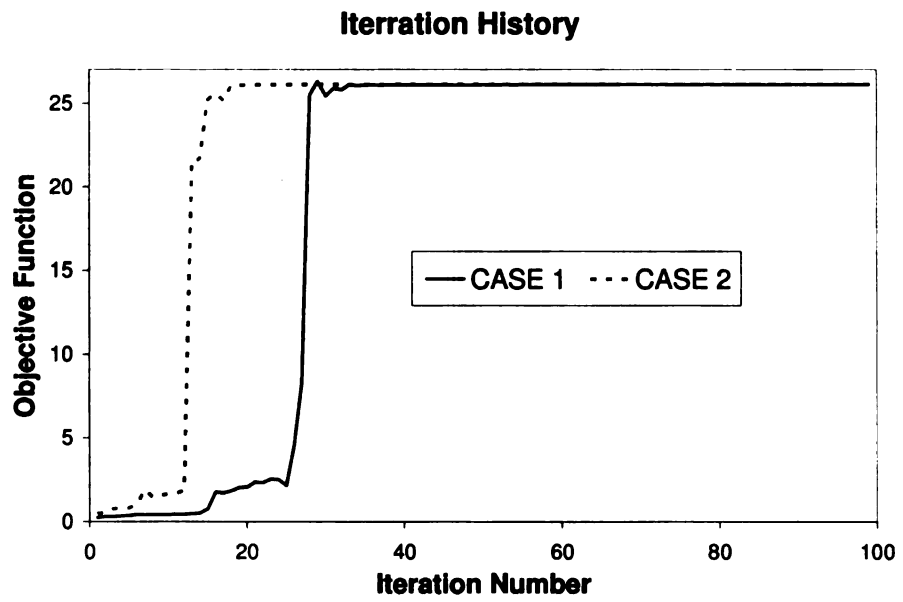


Figure 4.5 Graph of the iteration history for circular solid region with varied step size and initial conditions.

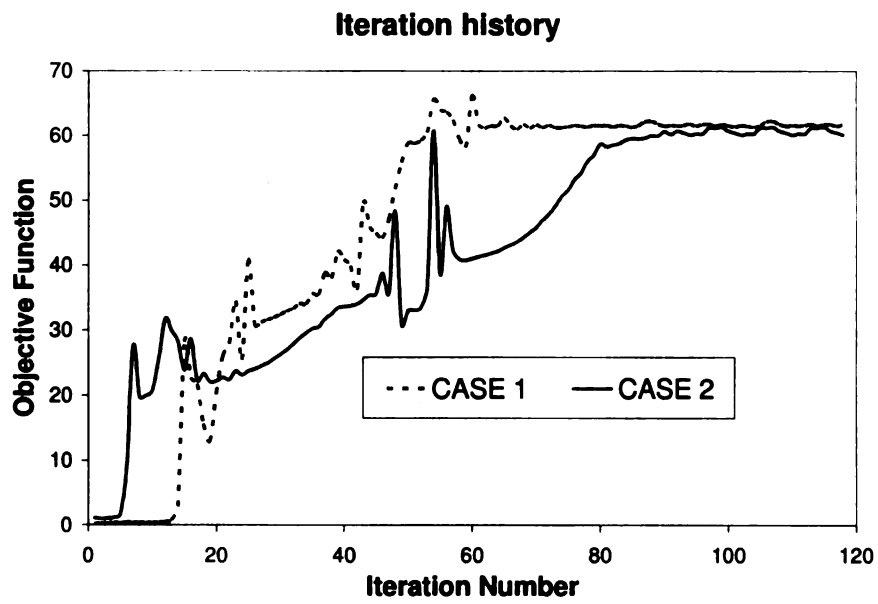


Figure 4.6 Graph of the iteration history for elliptic solid region with varied step size and initial conditions.

Iteration History

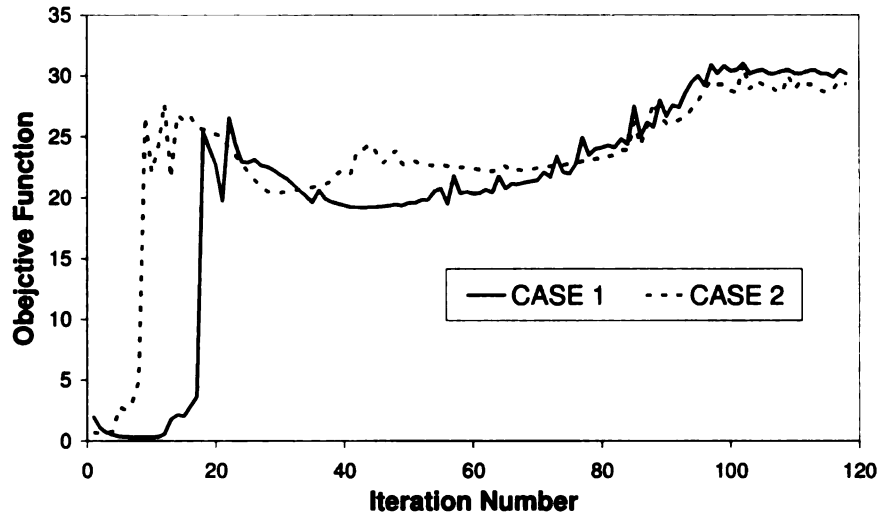
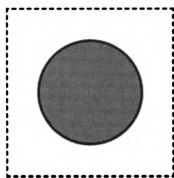


Figure 4.7 Graph of the iteration history for rectangular solid region with varied step size and initial conditions.

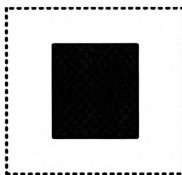
The optimal microstructure of the porous medium for the desired objective function to maximize isotropic effective permeability as discussed in section 4.3.1 for volume fraction of 0.3 for solid region is shown in Figure (4.8). The dimensions of the microstructures are shown in Table (4.1).



(a)



(b)



(c)

Figure 4.8. a-c. Schematic of the optimal periodic cells obtained after optimization. Dimensions of the periodic cells are shown in Table (4.1)

Table 4.1 Dimensions of the microstructures shown in Figure (4.8)

Figure (4.8)	l/h	a/h	b/h	θ
(a)	1	0.31		89.6
(b)	0.65	0.19	0.33	89.6
(c)	1.07	0.25	0.28	89.6

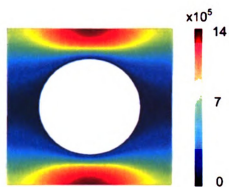
The effective permeability computed for the microstructures shown in Figure (4.8) a, b and c are;

$$\mathbf{K} = 3.9(10^{-5}) \begin{bmatrix} 1 & \varepsilon_c \\ \varepsilon_c & 1 \end{bmatrix} m^2, \quad \mathbf{K} = 2.5(10^{-5}) \begin{bmatrix} 1 & \varepsilon_e \\ \varepsilon_e & 1 \end{bmatrix} m^2 \quad \text{and}$$

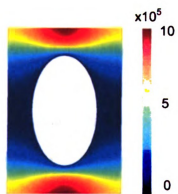
$$\mathbf{K} = 3.5(10^{-5}) \begin{bmatrix} 1 & \varepsilon_r \\ \varepsilon_r & 1 \end{bmatrix} m^2$$

where $\varepsilon_c = 4.07(10^{-3})$, $\varepsilon_e = 2.22(10^{-3})$, and $\varepsilon_r = 1.35(10^{-3})$

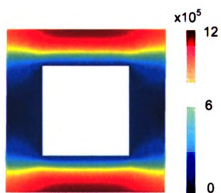
respectively. Figure (4.9) shows a contour of the distribution of longitudinal permeability (μU_{11}). It is observed in Figure (4.8) that the microstructure forms a square array for both the cases with circular and rectangular microstructure. Among the three microstructures, the circular microstructure gives the maximum effective permeability; but the diagonal terms of the permeability tensor are considerably higher than the other microstructures. Overall, the microstructure with rectangular solid region shows the best result. This may be due to the fact that it can be considered as a flow in a channel. It can be noted that for a given pressure gradient the velocity will have similar profile as the longitudinal permeability.



(a)



(b)



(c)

Figure 4.9. a-c. Schematic of distribution of longitudinal permeability (μU_{11}) for microstructures shown in Figure (4.5)

4.3.2 Maximizing the effective dispersivity

Dispersion of a solute can be of importance for applications involving reactors. The governing equations for solute transport are similar to the equation for heat transfer.. Industrial examples of solute or heat transport in porous media include static mixers (solute transport), heat exchanger (heat transport), and material for microchip (heat transfer). For numerous applications it is important how to disperse the solute or heat as fast as possible. In this section, the optimization algorithm seeks a periodic cell that maximizes the dispersion tensor. Maximizing the dispersion tensor maximizes the solute or heat transfer. The objective function is posed in a manner such that the algorithm also finds the required pressure gradient to maximize the isotropic dispersivity, which can be defined as

$$d\mathbf{I} = \mathbf{D} \quad (4.6)$$

The complete formulation of the optimization problem is stated as follows:

Find the optimal value of θ , l , a , b , $\nabla_X p^{(0)}$ and $\nabla_Y p^{(0)}$ for a given value of h , that will

maximize: Isotropic Effective Dispersivity

where isotropic effective dispersivity is expressed as $d - \varepsilon_d$

Here d and ε_d are computed from

$$d = \frac{1}{2} \sum_{i=1}^2 D_{ii} \quad (4.7)$$

and

$$\varepsilon_d = \left(\frac{1}{d}\right)^2 \left(\sum_{i=1}^2 \left(D_{ii} - D_{(i+1)(i+1)} \right)^2 + \sum_{i=1}^2 \sum_{j=2}^1 \left(D_{ij} \right)^2 \right) \quad (4.8)$$

D_{ij} is computed from solving equation (3.12).

subjected to: volumetric and geometric constraints

$$\text{Constraint 1: } \frac{\Omega_s}{\Omega_m} \geq V_{frac} \quad (4.9)$$

$$\text{Constraint 2: } a < \frac{l}{2}$$

$$\text{Constraint 3: } b < \frac{h \sin \theta}{2}$$

where Ω_s is the volume of the solid region, Ω_m is the total volume of the cell, and V_{frac} is value ($0 < V_{frac} < 1$) specifying the minimum solid volume.

The first constraint in equation (4.9) restricts the minimum volume of solid region to V_{frac} . The next two constraints are imposed to insure the continuity of each phase.

4.3.2.1 Example Problems

This section shows examples of shape optimization that will maximize the dispersivity as described in section 4.3.2. The solutions were obtained by casting the problem in the fashion of a standard shape optimization

problem . The derivatives of the objective function with respect to the design variables were computed using forward finite difference method as shown below,

$$\frac{\partial \text{Obj}}{\partial \text{dv}} = \frac{\text{Obj}_{\text{dv} + \delta \text{dv}} - \text{Obj}_{\text{dv}}}{\delta \text{dv}} \quad (4.10)$$

where “Obj” is the objective function and “dv” is the design variable. The derivatives of the constraints with respect to the design variables were computed analytically. The objective function was computed by solving the governing equations for the effective properties using the finite element method. The domain was discretized using an unstructured triangular mesh with 6000 elements of an average size of $4e^{-5}$ m as shown in Figure (4.4) The Method of Moving Asymptotes (MMA) as proposed by Krister Svanberg is used for optimization.

The results shown in this section are all for a limiting volume fraction of 0.3 and fixed value of 0.002 m for h . The physical properties of the fluid are taken as dynamic viscosity μ to be 0.001 Pa.s, density of fluid ρ^f to be 1000 Kg/m^3 , molecular diffusivity D set to $10^{-9} \text{ m}^2/\text{s}$. The dependence of the step size and initial value were in the optimization algorithm were verified by varying it those for two different cases. For case 1 the step size is set to 0.1 and initial aspect ratio is 1 (fixed height 0.002m), radius (or major axis, minor axis) set to 5×10^{-4} m and θ value to 90° . For case 2 the

step size is set to 0.5 and initial aspect ratio is 1, radius (or major axis, minor axis) set to 7×10^{-4} m and θ value to 90° . The iteration history for the different cases are shown in Figure (4.10 – 4.12) for circular, elliptic and rectangular solid region.

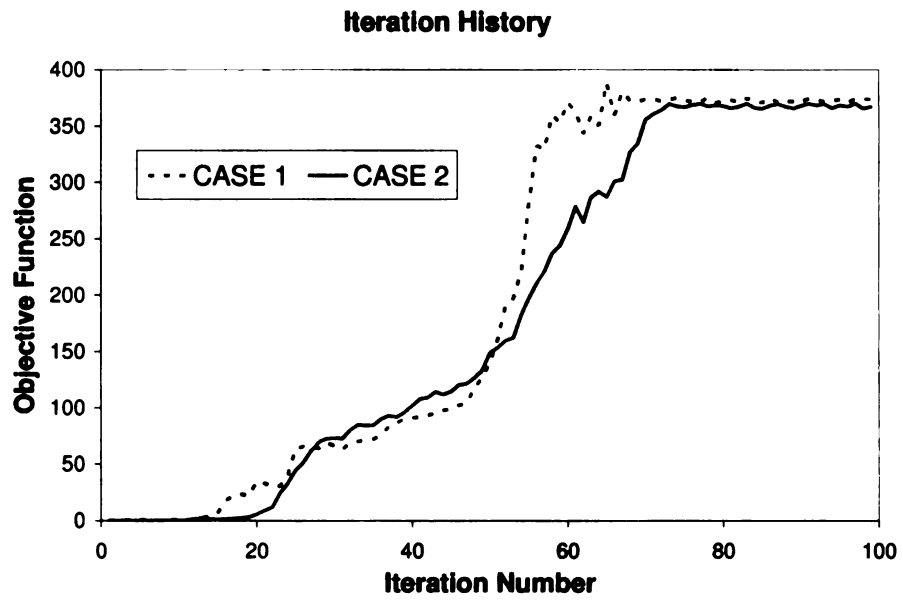


Figure 4.10 Graph of the iteration history for circular solid region with varied step size and initial conditions.

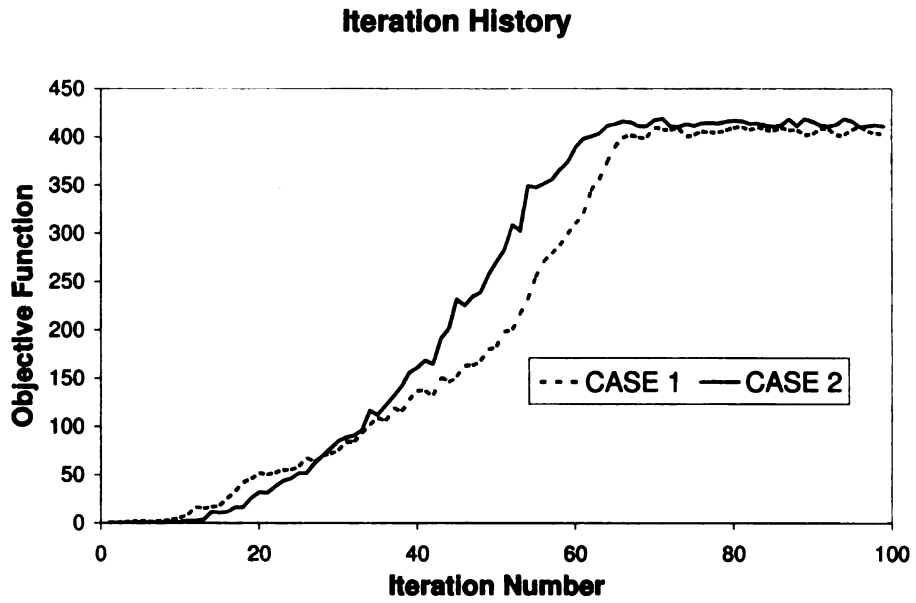


Figure 4.11 Graph of the iteration history for elliptic solid region with varied step size and initial conditions.

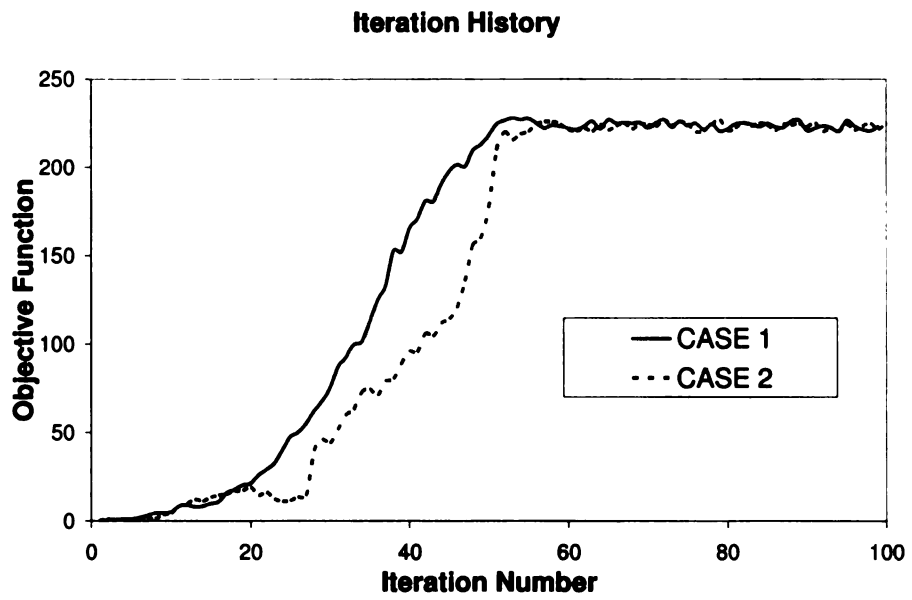


Figure 4.12 Graph of the iteration history for rectangular solid region with varied step size and initial condition.

The optimal microstructures of the porous medium for the desired objective function to maximize isotropic effective dispersive as discussed in section 4.3.2 for volume fraction of 0.3 are shown in Figure (4.13). The dimensions of the microstructures are shown in Table (4.2).

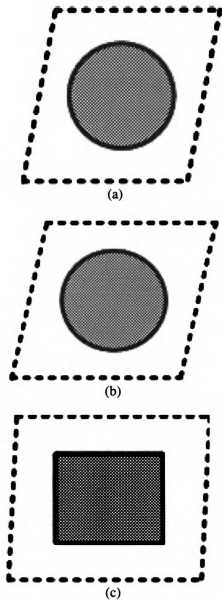


Figure 4.13. a-c. Schematic of the optimal periodic cells obtained after optimization with dimensions tabulated in Table (4.2)

Table 4.2 Dimensions of the microstructures as shown in Figure (4.13)

Figure (4.13)	l/h	a/h	b/h	θ
(a)	0.94	0.30		79.3
(b)	1.07	0.33	0.31	73.4
(c)	1.18	0.33	0.27	87.3

The optimal pressure gradients computed are $\begin{bmatrix} \nabla_X p^{(0)} \\ \nabla_Y p^{(0)} \end{bmatrix} = \begin{bmatrix} -1 \\ -0.9 \end{bmatrix} \text{N/m}^3$,

$$\begin{bmatrix} \nabla_X p^{(0)} \\ \nabla_Y p^{(0)} \end{bmatrix} = \begin{bmatrix} -1.3 \\ -0.5 \end{bmatrix} \text{N/m}^3 \text{ and } \begin{bmatrix} \nabla_X p^{(0)} \\ \nabla_Y p^{(0)} \end{bmatrix} = \begin{bmatrix} -0.7 \\ -0.4 \end{bmatrix} \text{N/m}^3 \text{ for Figure}$$

(4.13) a, b, and c respectively. The effective dispersion tensor computed for the periodic cell shown in Figure (4.13) a, b, and c are

$$\mathbf{D} = 1.5(10^{-8}) \begin{bmatrix} 1 & \alpha_c \\ \alpha_c & 1 \end{bmatrix} \text{m}^2/\text{s}, \quad \mathbf{D} = 1.67(10^{-8}) \begin{bmatrix} 1 & \alpha_e \\ \alpha_e & 1 \end{bmatrix} \text{m}^2/\text{s} \text{ and}$$

$$\mathbf{D} = 1.33(10^{-8}) \begin{bmatrix} 1 & \alpha_r \\ \alpha_r & 1 \end{bmatrix} \text{m}^2/\text{s}$$

where $\alpha_c = 2.0(10^{-2})$, $\alpha_e = 1.80(10^{-2})$ and $\alpha_r = 6.02(10^{-2})$ respectively.

One notable observation made from Figure (4.13): the angle between the length and the height goes to a lower value for circular and elliptic cross section. But for a rectangular cross section, the θ value approaches 90. This complements the previous argument that it forms a channel flow; and hence, it requires a comparative smaller pressure gradient to optimize the dispersion tensor, which is of the same magnitude of the other micro structures.

Figure (4.14) shows a contour of the distribution of the longitudinal component of the dispersion tensor (Z_{11}) in m^2/s . It can be noted from Figure (4.14) that the longitudinal term in the dispersion tensor is high in the horizontal direction, hence higher solute or heat transfer in the given direction. Figure (4.15) shows the velocity vectors which are periodic in nature.

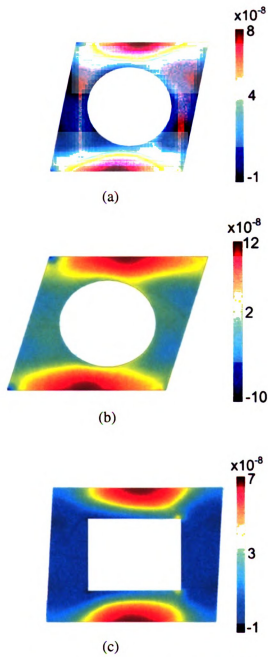
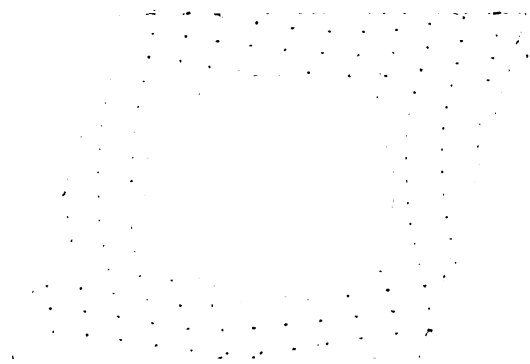


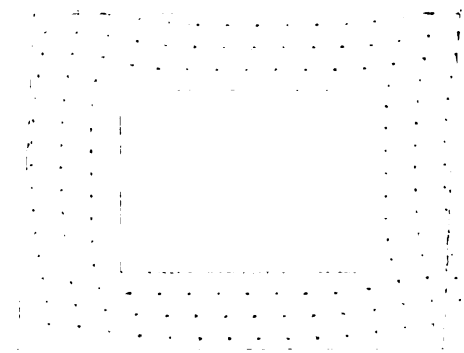
Figure 4.14 a-c. Schematic of distribution of longitudinal dispersivity (Z_{11}) for microstructures shown in Figure (4.7)



(a)



(b)



(c)

Figure 4.15 a-c. Schematic of velocity for microstructures shown in Figure (4.7)

4.4 Discussion

In this chapter a methodology to find the optimal microstructure for two different conditions; maximize effective permeability and effective dispersivity using shape optimization.

Attempts are made to maximize the effective properties by modifying the shape of the periodic cell. The magnitude of effective permeability computed is comparable to the work done by Guest and Prévost (Guest 2007). It is observed in Figure (4.8) that the microstructure forms a square array for both the cases with circular and rectangular microstructure. Among the three microstructures, the circular microstructure gives the maximum effective permeability; but the diagonal terms of the permeability tensor are considerably higher than the other microstructures. Overall, the microstructure with rectangular solid region shows the best result. This may be due to the fact that it can be considered as a flow in a channel.

In the next optimization example, the effective dispersion tensor is maximized. Here we try to maximize the effective property not only by modifying the shape of the periodic cell but also by finding the appropriate boundary condition. One notable observation made from Figure (4.13) is that the angle between the length and the height goes to a lower value for circular and elliptic cross section. But for a rectangular cross section, the θ value approaches 90. This complements the previous

argument that it forms a channel flow; and hence, it requires a comparative smaller pressure gradient to optimize the dispersion tensor, which is of the same magnitude of the other micro structures.

Finally, it can be concluded from the examples that a small change in geometry changes the effective properties significantly.

CHAPTER 5

DESIGN OF POROUS MEDIA USING SHAPE OPTIMIZATION TO MAXIMIZE “DISPERSIVE POWER” AND MINIMIZE DISSIPATION POWER

5.1 Introduction

A porous medium may have to satisfy more than one desired criteria and such problem is studied in this chapter. The desired criteria studied are maximizing the “dispersive power” and minimizing the dissipation power. The possible applications for such a medium include a static mixer (fluid flow and solute transfer), a heat exchanger (fluid flow - heat transfer), where the objective is to mix or disperse the solute (or heat) with minimum energy loss.

The problem is cast in the fashion of a standard shape optimization problem where various shapes described parametrically are studied. The periodic cells are defined in similar manner as described in Section 4.1.

5.2 Optimization of “dispersive power” and dissipation power

The topic of interest of this section is to find a microscopic geometry that will minimize the dissipation power while maximizing “dispersive power”.

Two different approaches were taken to find the optimal microstructure that minimize dissipation power and maximize dispersive power. In the first approach the pressure gradient was fixed and in the second approach the pressure gradient was kept as a design variable. The motivation behind two separate approaches was to understand the effect of the pressure gradient on microstructure in dispersion of fluid.

The complete formulation of the optimization problem for first approach is stated as

Problem definition 1:

Find θ , l , a and b for a given value of h , $\nabla_X p^{(0)}$ and $\nabla_Y p^{(0)}$ that will

$$\text{minimize: } \mathfrak{J}_{dissipation} - \mathfrak{J}_{dispersive}$$

The complete formulation of the optimization problem for second approach is stated as

Problem definition 2:

Find θ , l , a , b , $\nabla_X p^{(0)}$ and $\nabla_Y p^{(0)}$ for a given value of h , that will

$$\text{minimize: } \mathfrak{J}_{dissipation} - \mathfrak{J}_{dispersive}$$

Optimization algorithm MMA always minimize the objective function and since we are interested in minimizing $\mathfrak{J}_{dissipation}$ and maximizing $\mathfrak{J}_{dispersive}$, we include a negative sign before dispersive power term.

subjected to: volumetric and geometric constraints

$$\text{Constraint 1: } \frac{\Omega_s}{\Omega_m} \geq V_{frac}$$

$$\text{Constraint 2: } a < \frac{l}{2} \tag{5.1}$$

$$\text{Constraint 3: } b < \frac{h \sin \theta}{2}$$

where Ω_s is the volume of the solid region, Ω_m is the total volume of the cell, and V_{frac} is value ($0 < V_{frac} < 1$) specifying the minimum solid volume. The first constraint in equation (5.1) restricts the minimum volume of solid region to V_{frac} . Constraints 2 and 3 are imposed to insure the continuity of each phase.

$\mathfrak{J}_{dissipation}$ is the normalized value of dissipation power (Borrvall 2003). An expression for the dissipation energy for the fluid in the unit cell is derived from a mechanical energy balance. This is obtained by multiplying equation (2.9) with $\mathbf{v}^{(0)}$, where $\mathbf{v}^{(0)}$ is any weighted periodic

velocity satisfying equation (2.10) and boundary condition as shown in equation (2.12), and integrating over the entire domain

$$\mu \int_{\Omega_m} \nabla_x \mathbf{u}^{(0)} : (\nabla_x \mathbf{v}^{(0)})^T d\Omega - \int_{\Omega_m} p^{(1)} \text{div} \mathbf{v}^{(0)} d\Omega = \int_{\Omega_m} \nabla_X p^{(0)} \cdot \mathbf{v}^{(0)} d\Omega \quad (5.2)$$

where the double dot operator ($:$) is defined here as $\boldsymbol{\alpha} : \boldsymbol{\beta} = \alpha_{ij} \beta_{ji}$. The

first term in equation (5.2) is the viscous power and is responsible for dissipating the energy during fluid flow. This term is also called the dissipation power. After setting $\mathbf{v}^{(0)} = \mathbf{u}^{(0)}$

then, (5.3)

$$\mathfrak{S}_{dissipation} = \mu \int_{\Omega_m} \nabla_x \mathbf{u}^{(0)} : (\nabla_x \mathbf{u}^{(0)})^T d\Omega$$

The dissipation power is scaled with the square of the trace of the effective permeability after the expression for the velocity field is substituted

The dissipation power can be written in a dimensionless form as follows

$$\mathfrak{S}_{dissipation} = \int_{\Omega_m} \nabla_x \hat{\mathbf{u}}^{(0)} : (\nabla_x \hat{\mathbf{u}}^{(0)})^T d\Omega \quad (5.4)$$

$\mathfrak{S}_{dispersive}$ is the normalized value of “dispersive power”, which is computed by multiplying equation (3.10) with $c^{(0)}$, and integrating over

the entire domain, the following expression for “dispersive power” is obtained after using Green’s theorem:

$$\langle \mathbf{u} \rangle \int_{\Omega_m} \nabla_X c^{(0)} \cdot c^{(0)} d\Omega = \int_{\Omega_m} \nabla_X c^{(0)} \cdot \mathbf{D} \cdot \left[\nabla_X c^{(0)} \right]^T d\Omega \quad (5.5)$$

The right hand term is dispersive power term.

$$\mathfrak{S}_{dispersive} = \int_{\Omega_m} \nabla_X c^{(0)} \cdot \mathbf{D} \cdot \left[\nabla_X c^{(0)} \right]^T d\Omega, \quad (5.6)$$

where \mathbf{D} is the effective dispersion tensor, which can be computed from

$$\mathbf{D} = D \left\langle \left(\frac{1}{2} \left(\nabla_x \mathbf{N} + \nabla_x \mathbf{N}^T \right) + \mathbf{I} \right) - \frac{1}{2} \left(\left(\mathbf{u}^{(0)} \mathbf{N} \right) + \left(\mathbf{u}^{(0)} \mathbf{N} \right)^T \right) \right\rangle$$

The dispersive power term is scaled with the product of the trace of the dispersion and the trace of the concentration gradient. Dispersive power can be written in dimensionless terms as follows

$$\hat{\mathfrak{S}}_{dispersive} = \int_{\Omega_m} \nabla_X \hat{c}^{(0)} \cdot \hat{\mathbf{D}} \cdot \left[\nabla_X \hat{c}^{(0)} \right]^T d\Omega, \quad (5.7)$$

5.3 Example Problems

This section shows few examples of shape optimization for the objective functions described in section 5.2.1 and 5.2.2. The solutions were obtained by casting the problem in the fashion of a standard shape optimization problem as before. The derivatives of the objective function with respect

to the design variables were computed using forward finite difference method as

$$\frac{\partial \text{Obj}}{\partial dv} = \frac{\text{Obj}_{dv + \delta dv} - \text{Obj}_{dv}}{\delta dv} \quad (5.8)$$

where “Obj” is the objective function and “dv” is the design variable. The derivatives of the constraints with respect to the design variables were computed analytically.

The objective function was computed by solving the governing equations for the effective properties using finite element method. The domain was discretized using unstructured triangular mesh of element size of $4e^{-5}$ m as shown in Figure (4.1).

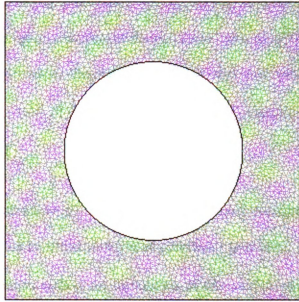


Figure 5.1 Schematic of the unstructured triangular mesh used for finite element analysis.

The Method of Moving Asymptotes (MMA) as proposed by Krister Svanberg is used for optimization. The results shown in this section are all for a limiting volume fraction of 0.3 and fixed value of 0.002m for h . The physical properties of the fluid are taken as dynamic viscosity μ to be 0.001 Pa.s , density of fluid ρ^f to be 1000 Kg/m³ , molecular diffusivity D set to 10^{-9} m²/s.

5.3.1 Optimization of dispersive power and dissipation power for a given base dimension and pressure gradient

As mentioned earlier, the motivation of this work is not only to find the optimal microstructure for given boundary conditions but also to understand the effect of pressure gradient on the objective function. Computations have been performed for two different shapes of the solid region (circular and elliptic solid region) for two given boundary conditions,

1. The concentration gradient is parallel to the flow field.
2. The concentration gradient is normal to the flow field.

For all the above-mentioned cases, the pressure gradient is varied while keeping the values of h .

Several optimal microstructures of the porous media for parallel and cross flow are shown in Figure (5.2 a-h). The dimensions of the microstructures as shown in Figure (5.2 a-h) are tabulated in Table (5.1) where l , h , a , b and θ are the length, height, major axis, minor axis and

angle between length and height for the periodic cell.. The macroscopic equation is solved for a domain of $1 \times 1 \text{ m}^2$ with a horizontal concentration gradient of 1 mol/m^3 and the pressure gradient has a unit of N/m^3 applied along horizontal direction. Periodic cells obtained when the concentration gradient is applied parallel to the flow field are shown in Figure (5.2 a-d). Periodic cells obtained when the concentration gradient is applied normal to the flow field are shown in Figure (5.2 e-f). The applied pressure gradients are -2 in Figure (5.2 a, c, e, g) and -0.5 in Figure (5.2 b, d, f, h) N/m^3 . Figure (5.2 a, b, e, f) represents the circular and Figure (5.2 c, d, g, h) represents the elliptic solid region. From figure 5.2 we see the optimized results shows a square array in most of the cases.

Further comparison of the magnitude of the objective functions versus pressure gradient is provided in Figures (5.3) and (5.4).

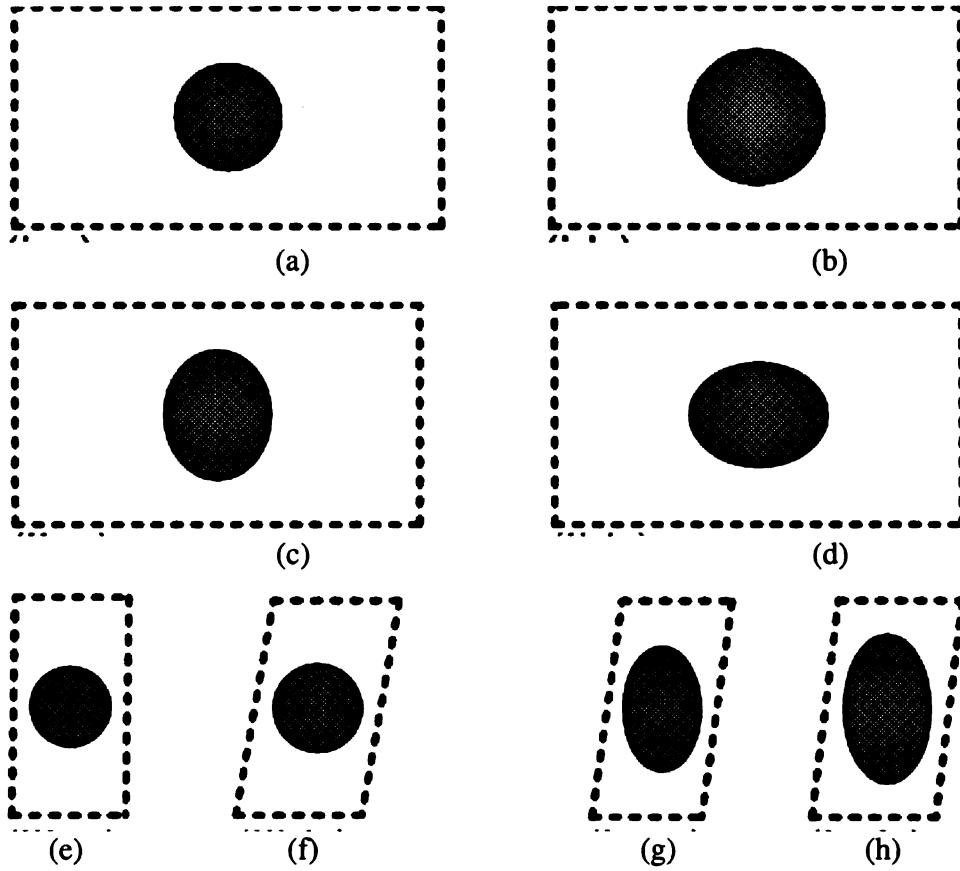


Figure 5.2 a-h Schematic of the optimal periodic cells obtained after optimization for the dimensions tabulated in Table (5.1)

Table 5.1 Dimensions of the periodic cells shown in Figure (5.2)

Figure (5.2)	l/h	a/h	b/h	θ
(a)	1.939	0.231		90
(b)	1.864	0.297		90
(c)	1.840	0.233	0.285	90
(d)	1.852	0.304	0.226	90
(e)	0.516	0.172		89
(f)	0.573	0.191		80
(g)	0.498	0.165	0.276	82
(h)	0.564	0.188	0.331	83

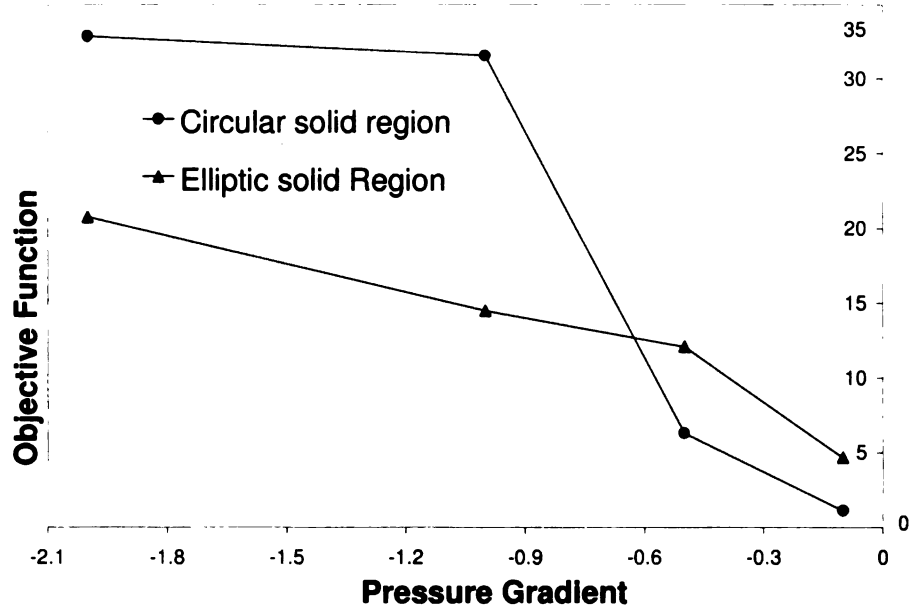


Figure 5.3 Computed values of the objective functions for a parallel flow configuration.

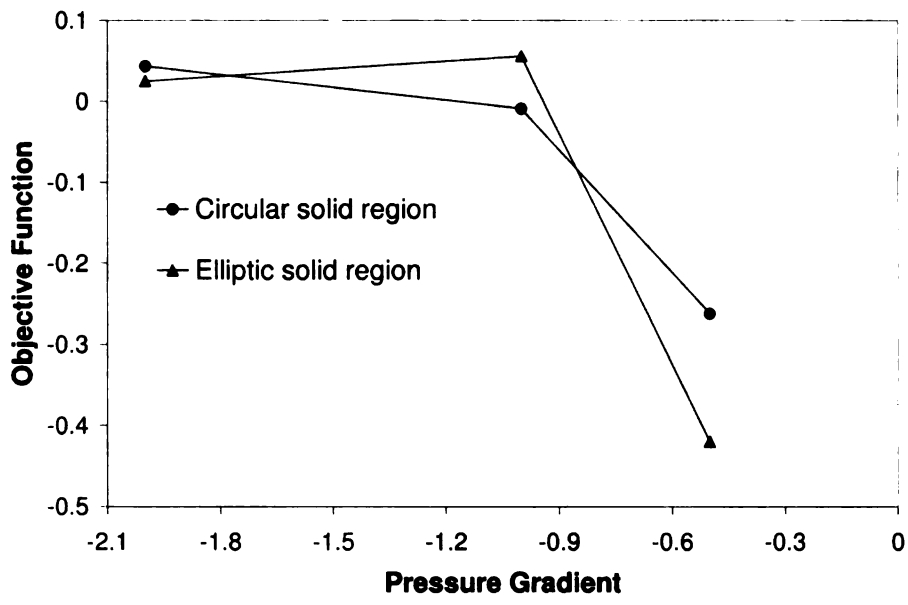


Figure 5.4 Computed values of the objective functions for a cross flow configuration.

It is seen in Figures (5.3) and (5.4) that the magnitude of $\mathfrak{S}_{dissipation} - \mathfrak{S}_{dispersive}$ decreases for a decrease in pressure gradient. This can be explained with reference to equation (5.3) and (5.4). Since the dissipation power directly proportional to the pressure term, for a higher pressure gradient a higher value of dissipation power is expected.

5.3.2 Optimization of the “dispersive power” and the dissipation power for a given base dimension

In the previous section the variation of objective function with pressure gradient is studied. In this section, I am interested in finding the optimal pressure gradient that satisfies both the desired criterion; maximize “dispersive power” and minimize dissipation power. The optimal microstructures of the porous medium for the desired objective function as described in section 5.1 for volume fraction of 0.3 for solid phase and prescribed molecular diffusivity of 10^{-9} m/s² are shown in Figure (5.5). The macroscopic equation is solved for a domain of 1x1 m² with a horizontal concentration gradient of 1 mol/m³.

The dependence of the step size and initial values in the optimization algorithm were verified by varying those for two different cases. For case 1 the step size is set to 0.1 and initial aspect ratio is 1, the radius (major axis, minor axis) is set to 5×10^{-4} m and θ to a value of 90°. For case 2 the step size is set to 0.5 and initial aspect ratio is 1, the radius (major axis,

minor axis) set to $7 \times 10^{-4} \text{m}$ and θ to a value to 90° . The iteration history for the different cases are shown in Figure (4.10 – 4.12) for circular, elliptic and rectangular solid region.

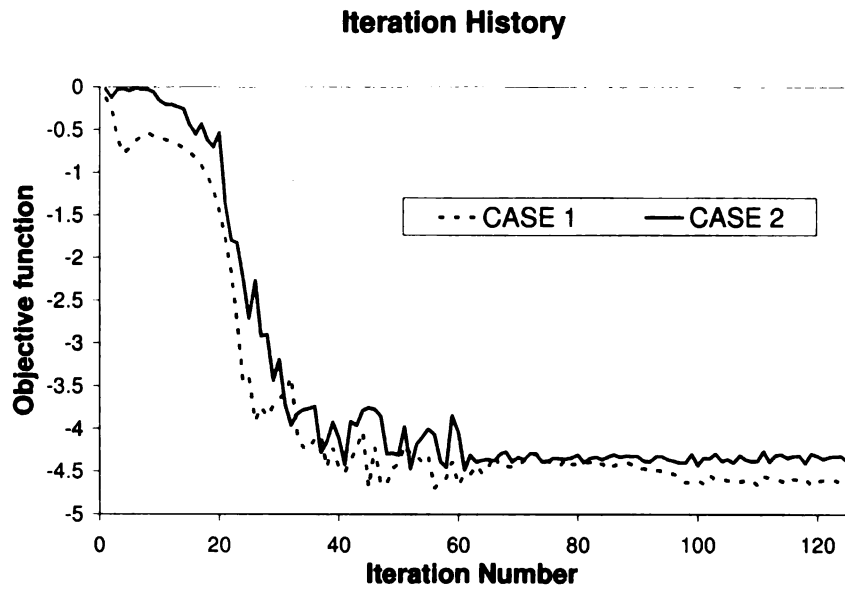


Figure 5.5 Graph of the iteration history for the circular solid region with a varied step size and initial conditions.

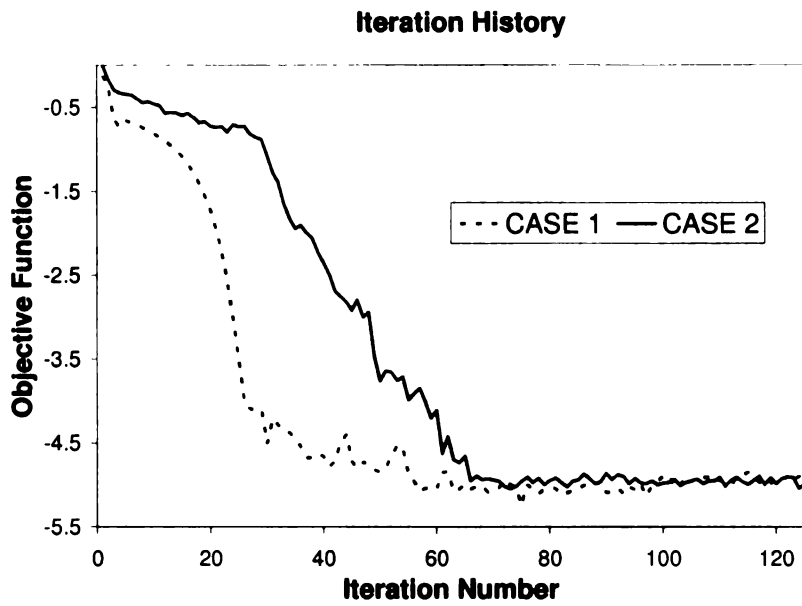


Figure 5.6 Graph of the iteration history for the elliptic solid region with a varied step size and initial conditions.

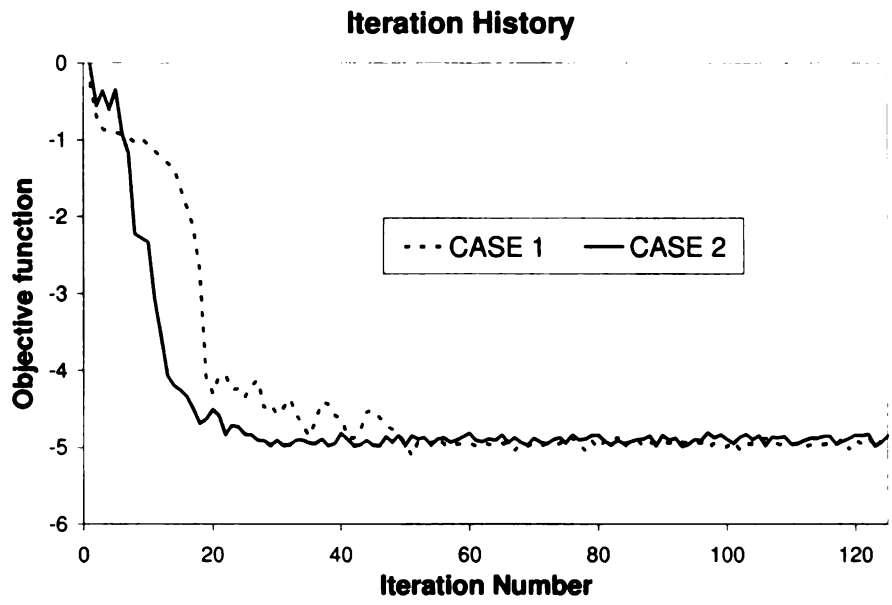
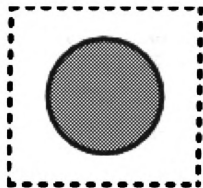
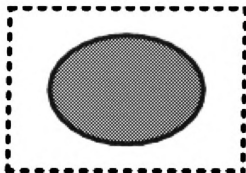


Figure 5.7 Graph of the iteration history for the rectangular solid region with a varied step size and initial conditions.

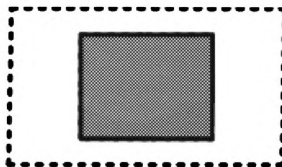
The dimensions of the microstructures are shown in Table (5.2) where l , h , a , b and θ are the length, height, major axis, minor axis and angle between length and height for the periodic cell. The optimal values of normalized dissipation power and normalized dispersion power evaluated are tabulated in Table (5.3).



(a)



(b)



(c)

Figure 5.8. a-c. Schematic of the optimal periodic cells obtained after optimization with the dimensions tabulated in Table (5.2)

Table 5.2 Dimensions of the microstructures as shown in Figure (5.8).

Figure (5.8)	l/h	a/h	b/h	θ
(a)	1.07	0.32		89
(b)	1.44	0.47	0.33	89
(c)	1.74	0.42	0.33	89

Table 5.3 Optimized value of normalized dissipation power and normalized dispersion power for the microstructures as shown in Figure (5.8)

Figure (5.8)	$\mathcal{J}_{dissipation}$	$\mathcal{J}_{dispersive}$
(a)	0.01427	4.63
(b)	0.007658	4.96
(c)	0.000772	4.93

The optimal pressure gradient computed are

$$\begin{bmatrix} \nabla_X p^{(0)} \\ \nabla_Y p^{(0)} \end{bmatrix} = \begin{bmatrix} 8(10^{-6}) \\ -0.7 \end{bmatrix} \text{N/m}^3, \quad \begin{bmatrix} \nabla_X p^{(0)} \\ \nabla_Y p^{(0)} \end{bmatrix} = \begin{bmatrix} 8(10^{-6}) \\ -0.4 \end{bmatrix} \text{N/m}^3 \quad \text{and}$$

$$\begin{bmatrix} \nabla_X p^{(0)} \\ \nabla_Y p^{(0)} \end{bmatrix} = \begin{bmatrix} 8(10^{-6}) \\ -0.1 \end{bmatrix} \text{N/m}^3 \text{ for Figure (5.8) a, b, and c respectively.}$$

The average effective permeability and the average dispersion tensor computed for the periodic cells shown in Figure (5.8) a, b, and c are

$$\mathbf{K} = 3.41(10^{-5}) \begin{bmatrix} 1 & \varepsilon_c \\ \varepsilon_c & 1.38 \end{bmatrix} \text{m}^2,$$

$$\mathbf{D} = 5.4(10^{-9}) \begin{bmatrix} 1 & 1.31 \\ 1.31 & 3 \end{bmatrix} \text{m}^2/\text{s}$$

$$\mathbf{K} = 3.07(10^{-5}) \begin{bmatrix} 1 & \varepsilon_e \\ \varepsilon_e & 1.81 \end{bmatrix} \text{m}^2,$$

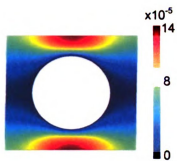
$$\mathbf{D} = 5.20(10^{-9}) \begin{bmatrix} 1 & 1.31 \\ 1.31 & 3 \end{bmatrix} \text{m}^2/\text{s},$$

$$\text{and } \mathbf{K} = 1.91(10^{-5}) \begin{bmatrix} 1 & \varepsilon_r \\ \varepsilon_r & 7.62 \end{bmatrix} \text{m}^2,$$

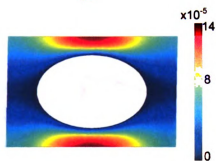
$$\mathbf{D} = 4.50(10^{-9}) \begin{bmatrix} 1 & 1.56 \\ 1.56 & 3 \end{bmatrix} \text{m}^2/\text{s},$$

where $\varepsilon_c = 1.4(10^{-2})$, $\varepsilon_e = 2.12(10^{-2})$, $\varepsilon_r = 1.61(10^{-1})$ respectively.

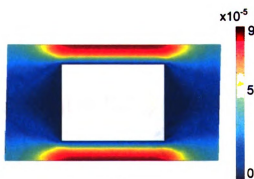
Figures (5.9) and (5.10) show a contours of the longitudinal component of the effective permeability and dispersivity



(a)

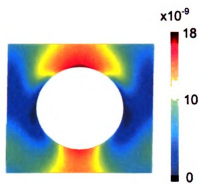


(b)

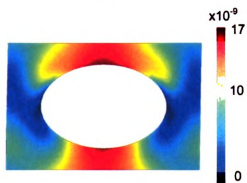


(c)

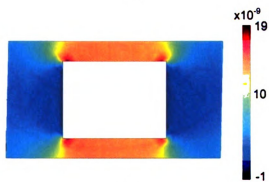
Figure 5.9 a-c. Contours of the longitudinal component of the permeability (μU_{11}) for the microstructures shown in Figure (5.8)



(a)

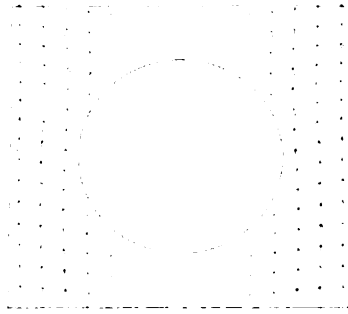


(b)



(c)

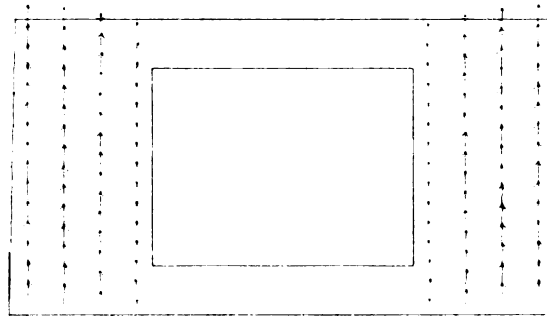
Figure 5.10 a-c. Contours of the longitudinal component of the dispersivity (Z_{11}) for the microstructures shown in Figure (5.8)



(a)



(b)



(c)

Figure 5.11 a-c. Plots of the velocity vectors in microstructure corresponding to Figure (5.8)

5.4 Discussion

In this chapter a methodology to find the optimal microstructure that maximize mixing and minimize energy loss using shape optimization is presented

A goal is also to find a periodic cell that provides a better solute dispersion while minimizing the energy loss for a fixed or a variable pressure gradient. It is seen in Figures (5.3) and (5.4) that the magnitude of $\mathfrak{J}_{dissipation} - \mathfrak{J}_{dispersive}$ decreases for a decrease in pressure gradient. For a higher pressure gradient, a higher value of dissipation power is expected compared to the dispersive power. For a flow normal to the concentration gradient, the optimization process does not converge to a finite value for a very low pressure gradient (-0.1 N/m^3). This may be due to the fact that the applied pressure gradient is not sufficient to disperse the solute though out the domain. Also since because of the nature of the problem the final results are highly dependent on initial value and sometimes the solution is not the global solution. Furthermore the sensitivity of $\mathfrak{J}_{dissipation} - \mathfrak{J}_{dispersive}$ are approximated using finite difference method, which may cause some additional errors.

In the second analysis it can be observed from Table (5.3) that for the microstructure with a rectangular solid region, the energy loss due to dissipation is the least and that the solute dispersion is comparable to the

other microstructures. Since the pressure gradient is also included as the design variable, it takes the advantage of a higher transverse effective permeability (K_{22}) and adjusts itself to minimize the energy loss. In other words it minimizes the pressure gradient in the horizontal direction and diverts the flow in vertical direction. This is also because the height was fixed; whereas, other dimensions could vary.

The results obtained using shape optimization for minimizing dissipation power and maximizing “dispersion power” ,in which the pressure gradient is a design variable, can be compared with the microstructure formed by a square array of same porosity. The comparison shows significant improvements in reducing energy losses in the fluid flow and increased mixing. Figure (5.12) shows the macroscopic

layout with an applied pressure gradient
$$\begin{bmatrix} \nabla_X p_x \\ \nabla_X p_y \end{bmatrix} = \begin{bmatrix} 8(10^{-6}) \\ 0.4 \end{bmatrix}$$

obtained for elliptic cross section (Figure 5.8 (b)). The macroscopic velocity field computed from the Darcy’s equation is compared at the cross section shown by dashed line in Figure (5.13). When compared with the microstructure form by square array of same porosity, the optimized microstructure results in a higher velocity field as shown in Figure (5.14).

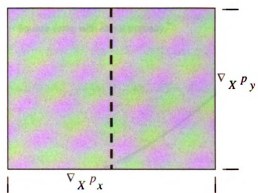


Figure 5.12 Schematic of the macroscopic layout with applied boundary conditions

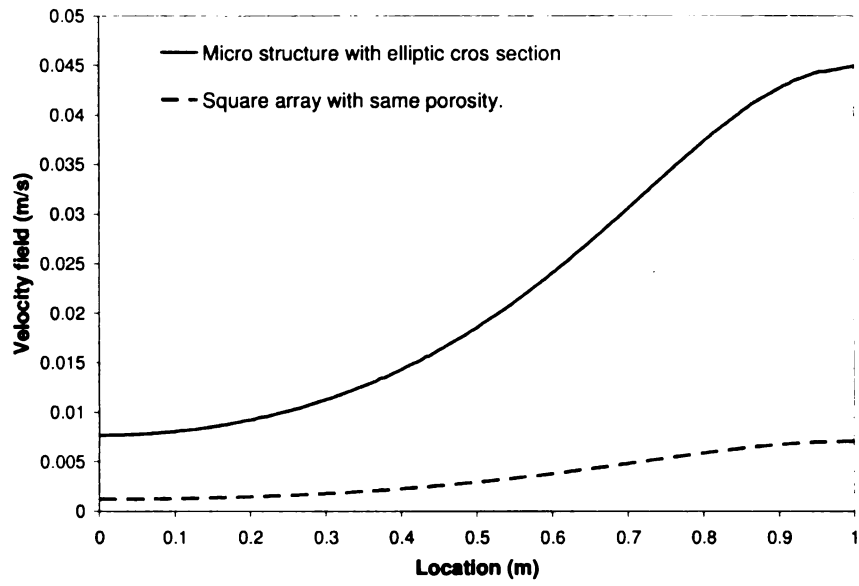
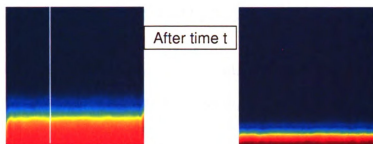


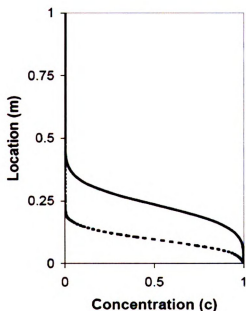
Figure 5.13 Comparison of the velocity fields for a domain with a microstructure formed with the optimized elliptic cross section with the velocity field for a square array of same porosity.

The objective function in this chapter is set in such a way that it also maximizes the “dispersive power” or mixing. Figure (5.11) shows higher solute dispersion at time t for the optimized microstructure. The concentration are compared for both the cases and shown in Figure (5.11 c).



(a)

(b)



(c)

Figure 5.14 a-c. Comparison of solute dispersion after time $t = 0.02$ sec for the macroscopic domain formed with a microstructure of elliptic cross section cylinders (a) obtained from shape optimization with the microstructure obtained from a square array (b) of same porosity. The magnitude of c is shown in right (c).

CHAPTER 6

TOPOLOGY OPTIMIZATION OF FLUID FLOW IN POROUS MEDIA TO MINIMIZE DISSIPATION POWER

6.1 Introduction

Topology optimization is a layout optimization technique that was originally developed to design mechanical structures (Bendsøe and Kikuchi, 1988). Its scope was rapidly expanded to the diverse field such as optics and acoustics (Bendsøe and Sigmund 2003, Eschenauer 2001, Jensen 2003, 2004) and recently it has been applied in the field of fluid flow by Borrvall and Petersson (Borrvall 2003). Most of the above mentioned works were mainly applied to macroscopic layout problems. With further development of the homogenization theory, topology optimization was used to find the layout of the microstructure or the base cell of the material. Few such noted works are: Sigmund (Sigmund and Torquato 1996) to design microstructure for material that yield negative thermal expansion, Larsen (Larsen 1996) to design material that yields negative Poisson's ratio and Diaz and Bénard (Diaz and Bénard 2003) to design material that matches prescribed elastic properties.

The formulation of the problem is given in the following section. The Method of Moving Asymptotes (MMA) as proposed by Krister Svanberg

(Svanberg 1978, 2002) is used for optimization. The derivatives of the objective function and the constraints with respect to the design variables were computed using adjoint method as proposed by Olesen, Okkel and Bruus (Olesen 2006). Figure (6.1) shows the flowchart of step by step approach to find the optimal microstructure using topology optimization.

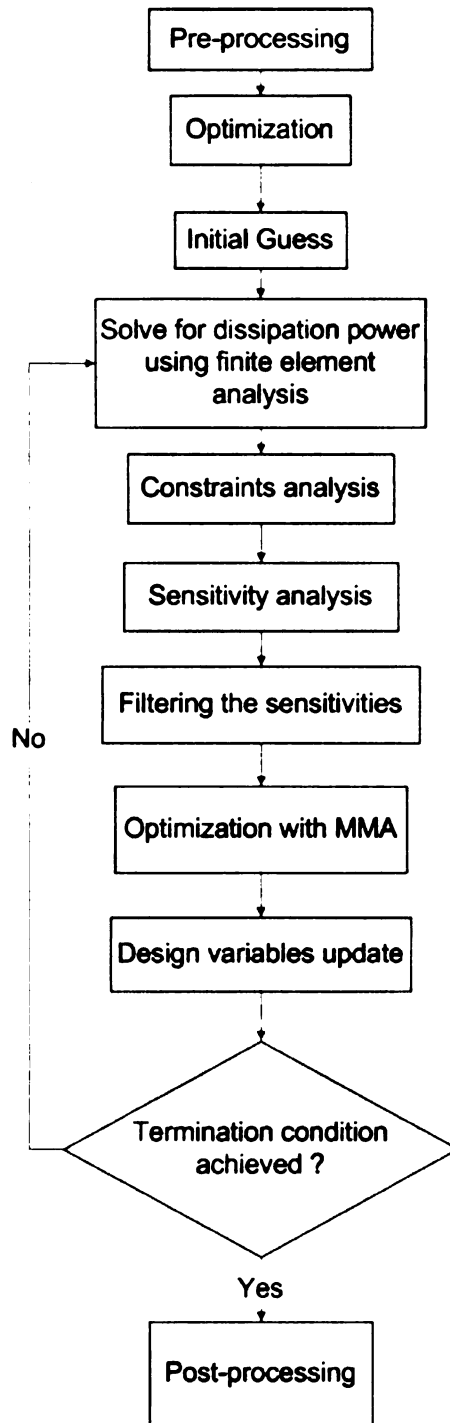


Figure 6.1 Flowchart showing the steps of the algorithm based on topology optimization for designing microstructures.

6.2 Formulation of the optimization problem

In the analysis, the macroscopic domain (Ω_M) is assumed to be homogeneous with periodic microscopic cells (Ω_m). The microscopic cell has two distinct regions: a solid region (Ω_s) and a fluid region (Ω_f) such that $\Omega_m = \Omega_s \cup \Omega_f$ and $\Omega_s \cap \Omega_f = \emptyset$. The interface between the solid-fluid in each periodic cell is Γ_{sf} and the interface between two periodic cells is denoted by Γ_{cell} .

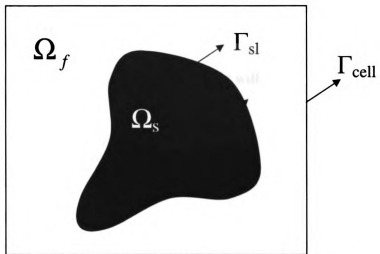


Figure 6.2. Schematic of a periodic microscopic cell (Ω_m). The interface between the solid-fluid in each periodic cell is Γ_{sl} and the interface between two periodic cells is denoted by Γ_{cell} .

6.2.1 Minimizing Dissipation power

The objective in this section is to minimize the energy losses or the dissipation power.

Find the optimal layout for the periodic cell that will

minimize: $\int dissipation$

subjected to: volumetric and geometric constraints

$$\text{Constraint: } \frac{\Omega_s}{\Omega_m} \geq V_{frac} \quad (6.1)$$

where Ω_s is the volume of the solid region, Ω_m is the total volume of the cell, and V_{frac} is value ($0 < V_{frac} < 1$) specifying the minimum solid volume. The constraint in equation (6.1) restricts the minimum volume of solid region to V_{frac} .

The governing equations here are the homogenized Navier-Stokes equation and the incompressibility constraint as derived in Chapter 2. To generalize the above governing equation for both solid and fluid phase, the fluid flow through the solid region is subjected to a friction force, which is proportional to the fluid velocity. The governing equations for the zeroth order problem are given by

$$\mu \nabla_x^2 \mathbf{u}^{(0)} - \nabla_x p^{(1)} = \nabla_X p^{(0)} - \alpha \mathbf{u}^{(0)} \text{ in } \Omega_m \quad (6.2)$$

and

$$\nabla_x \cdot \mathbf{u}^{(0)} = 0 \text{ in } \Omega_m \quad (6.3)$$

where $\nabla_X p^{(0)}$ is the pressure gradient across the macroscopic domain and is applied as a source term (a known quantity). These governing equations are valid for both solid and fluid regions. The penalty term α , which is a function of the design variable ρ , allows to set the velocity equal to zero in a solid domain. The design variable ρ controls the phase of the medium as follows;

$$\rho(x) = \begin{cases} 0 & \text{if } x \in \Omega_s \\ 1 & \text{if } x \in \Omega_f \end{cases} \quad (6.4)$$

Following reference Borrvall (Borrvall 2003) and Olesen (Olesen 2005), the penalty term α and design variable ρ are related by the convex interpolation.

$$\alpha(\rho) \equiv \alpha_{\min} + (\alpha_{\max} - \alpha_{\min}) \frac{q[1-\rho]}{q+\rho} \quad (6.5)$$

where q is a real and positive parameter used to tune the shape of the penalty term and taken as 0.01. In this work α_{\min} is taken as zero and

α_{\max} is a large number (10^5). The dependence of α on q is shown in

Figure (6.3). For $q = 1$, it gives a linear plot from α_{\max} to α_{\min} over the

range of ρ . For lower value of q (0.01), α value is close to α_{\min} for ρ

varying from 0.2-1. This approach is done to penalize the grey material

formation, which is a mixture of solid and fluid and promote either the fluid or liquid phases.

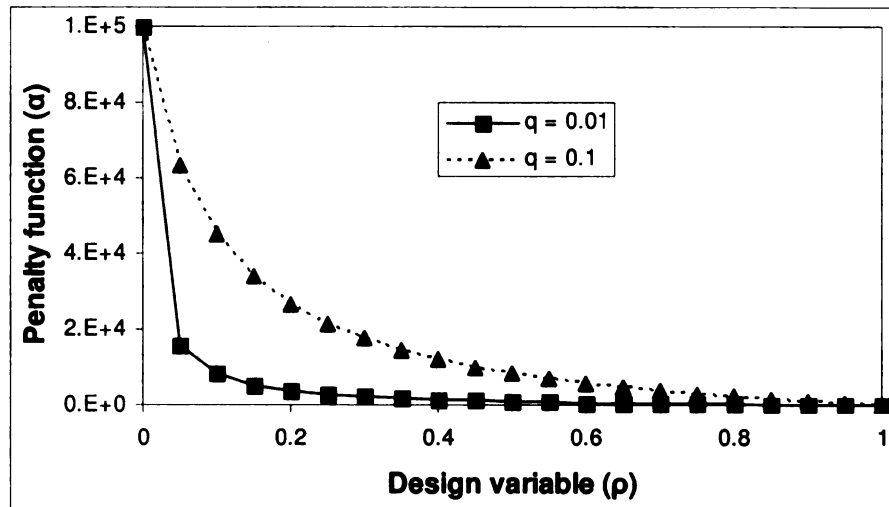


Figure 6.3 Plot showing the dependence of α on q .

The boundary condition are that of periodic flow through the boundaries of the cell and no slip boundary condition at the solid fluid interface of the inclusion.

$$\mathbf{u}^{(0)} = \mathbf{u}^{(1)} = \dots = 0 \text{ on } \Gamma \text{ (solid-fluid interface),} \quad (6.6)$$

$\mathbf{u}^{(0)}, \mathbf{u}^{(1)} \dots$ and $p^{(0)}, p^{(1)} \dots$ are Ω_m -periodic.

The $\mathfrak{S}_{dissipation}$ is the dissipation energy for the fluid in the unit cell and is derived from mechanical energy balance. Just as before, it is obtained by multiplying equation (6.2) with $\mathbf{v}^{(0)}$, where $\mathbf{v}^{(0)}$ is any weighted periodic velocity satisfying equation (6.3) and boundary condition as shown in equation (6.6), and integrating over the entire domain After setting $\mathbf{v}^{(0)} = \mathbf{u}^{(0)}$

$$\mathfrak{S}_{dissipation} = \mu \int_{\Omega_m} \nabla_x \mathbf{u}^{(0)} : (\nabla_x \mathbf{u}^{(0)})^T d\Omega \quad (6.8)$$

In dimensionless form equation 6.8 can be rewritten as,

$$\hat{\mathfrak{S}}_{dissipation} = \int_{\Omega_m} \nabla_x \hat{\mathbf{u}}^{(0)} : (\nabla_x \hat{\mathbf{u}}^{(0)})^T d\Omega \quad (6.9)$$

where $\hat{\mathbf{u}}^{(0)}$ is the dimensionless form of $\mathbf{u}^{(0)}$ related by

$$\hat{\mathbf{u}}^{(0)} = \mathbf{u}^{(0)} / \langle \mathbf{u}^{(0)} \rangle.$$

6.2.2 Implementation Issues

To promote a discontinuous microstructure and avoid cases of a continuous solid region, the layout is divided into two initial zones. Zone 1 is formed only by fluid material and forms the outer boundary of the periodic cell, whereas Zone 2 is formed on both solid and fluid material as shown in Figure (6.4). In Zone 1 the α value is taken as zero.

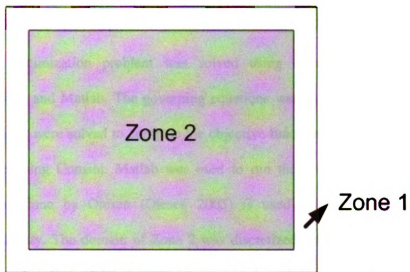


Figure 6.4 Schematic of a periodic microscopic cells with a liquid zones imposed on Zone 1 above to avoid a continuous solid region between the cells.

6.3 Example Problems

The optimization problem was solved using commercial software's Comsol and Matlab. The governing equations were mentioned in earlier sections were solved to compute the objective function and the sensitivity were using Comsol. Matlab was used to run the optimization process. Work done by Olesen (Olesen 2005) is used here to compute the sensitivity. The domain of Zone 2 was discretized using an unstructured triangular mesh of 50 elements along each boundary as shown in Figure (6.5).

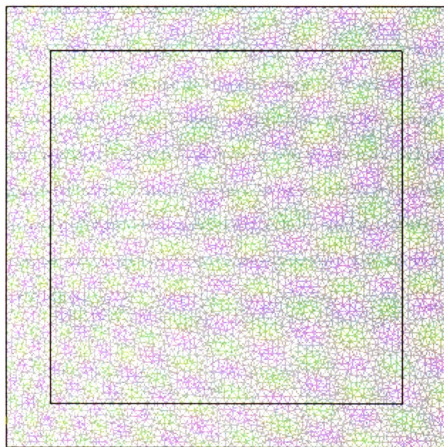


Figure 6.5 Schematic of the unstructured triangular mesh used for the finite element analysis.

6.3.1 Minimizing Dissipation Power

In this section, the optimized microstructures for the porous media for different boundary condition are computed. Figure (6.6) and (6.7) shows the microstructure obtained when a macroscopic pressure gradient of 1N/m^2 is applied in the horizontal direction with volume fraction of solid region is limited to 0.5 and 0.7. In Figure 6.6 we see that for lower volume fraction of solid the microstructure forms a elliptic solid region, whereas for higher volume fraction it forms a rectangular shape solid region with curved edges.

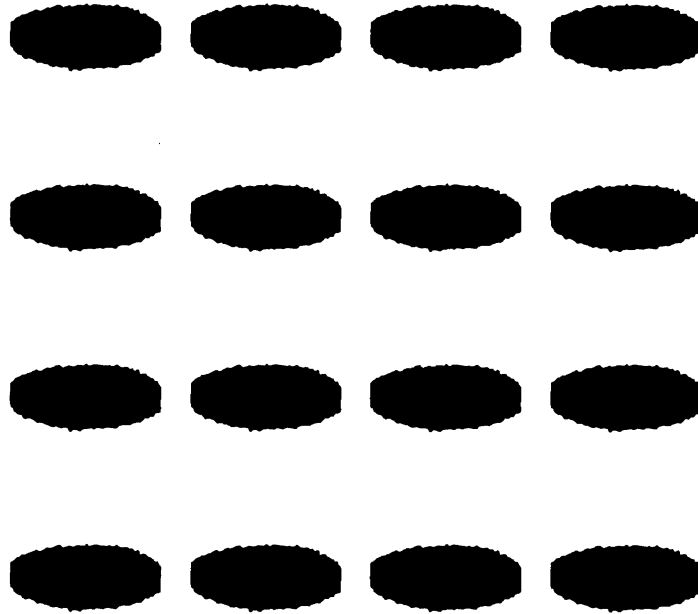


Figure 6.6 Schematic of microstructure layout for volume fraction 0.5 and with macroscopic pressure gradient of 1N/m^2 in horizontal direction

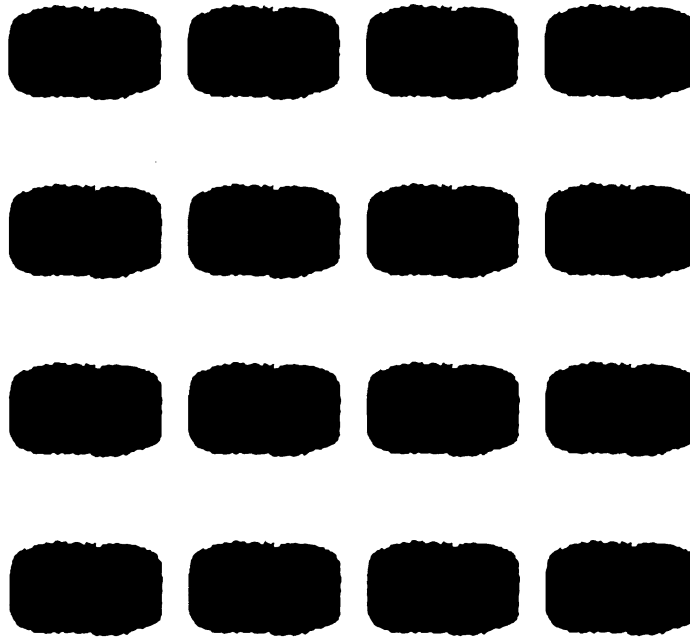


Figure 6.7 Schematic of microstructure layout for volume fraction 0.7 with macroscopic pressure gradient of 1N/m^2 in horizontal direction

Figure (6.8) – (6.14) shows the microstructure obtained when macroscopic pressure gradient of 1N/m^2 is applied in both horizontal and vertical direction with volume fraction of solid region is limited to 0.1, to 0.8.

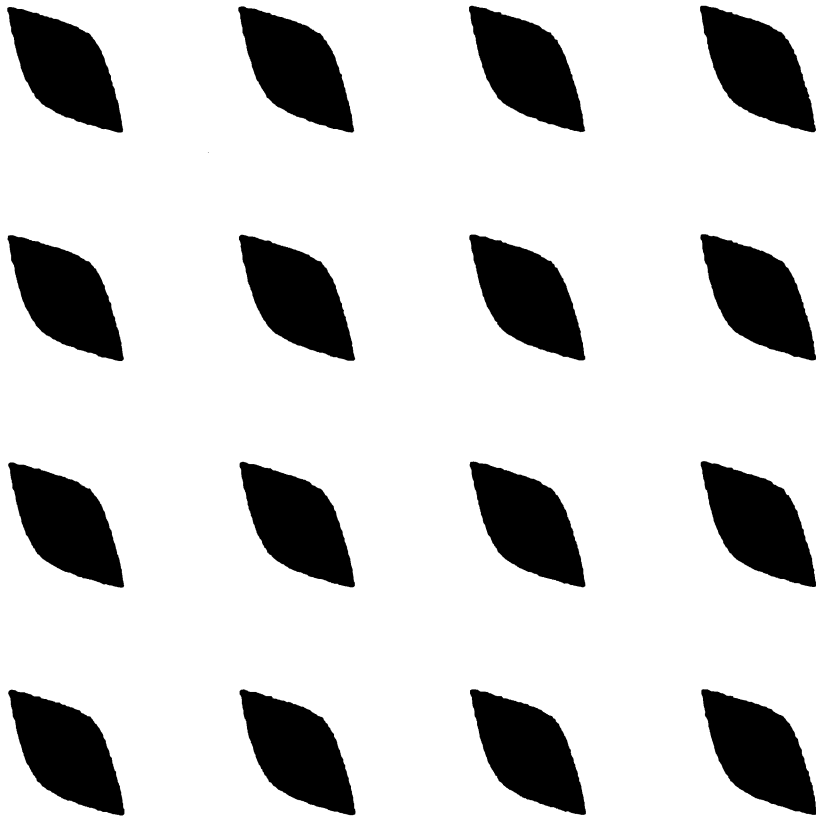


Figure 6.8. Schematic of the microstructure layout for a volume fraction 0.2 with an equal macroscopic pressure gradient of 1N/m^2 in the horizontal and vertical directions.

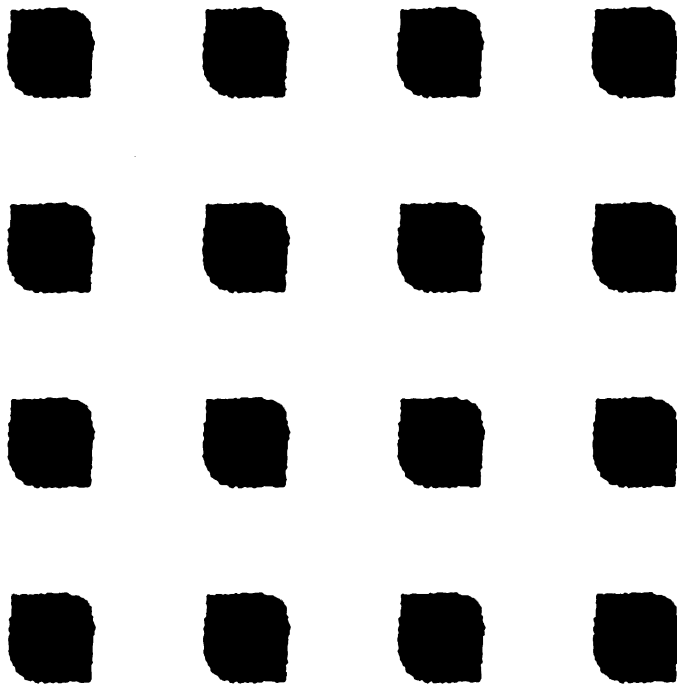


Figure 6.9. Schematic of the microstructure layout obtained for a volume fraction of 0.3 with an equal macroscopic pressure gradient of 1N/m^2 in the horizontal and the vertical directions

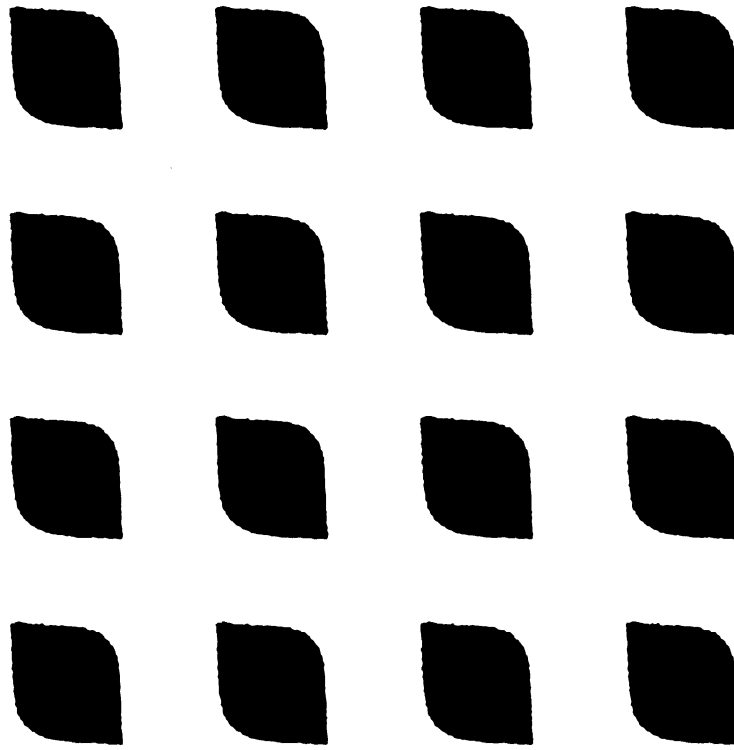


Figure 6.10. Schematic of a microstructure layout for volume fraction 0.4 with equal macroscopic pressure gradient of 1N/m^2 in the horizontal and the vertical directions.

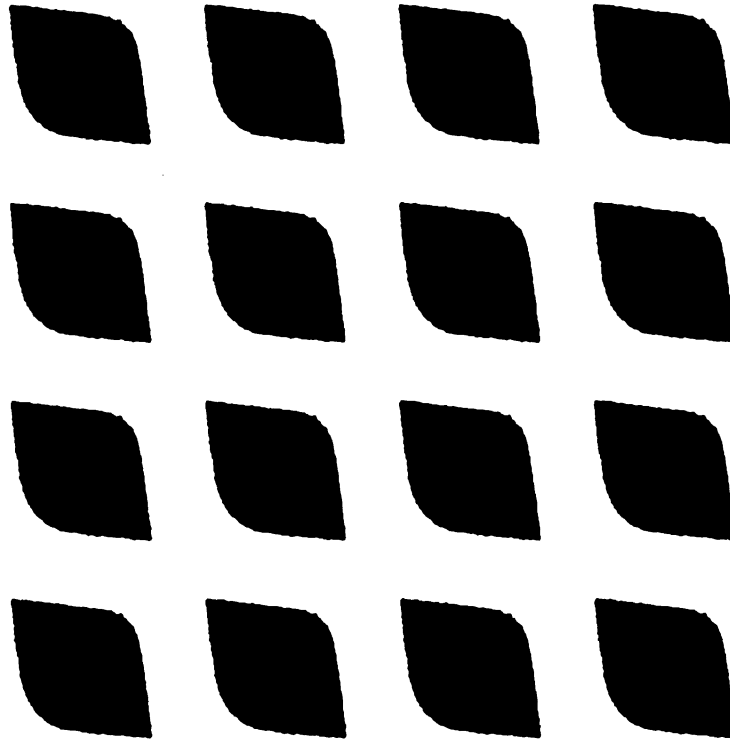


Figure 6.11 Schematic of the microstructure layout for a volume fraction 0.5 with equal macroscopic pressure gradients of 1N/m^2 in the horizontal and vertical directions.

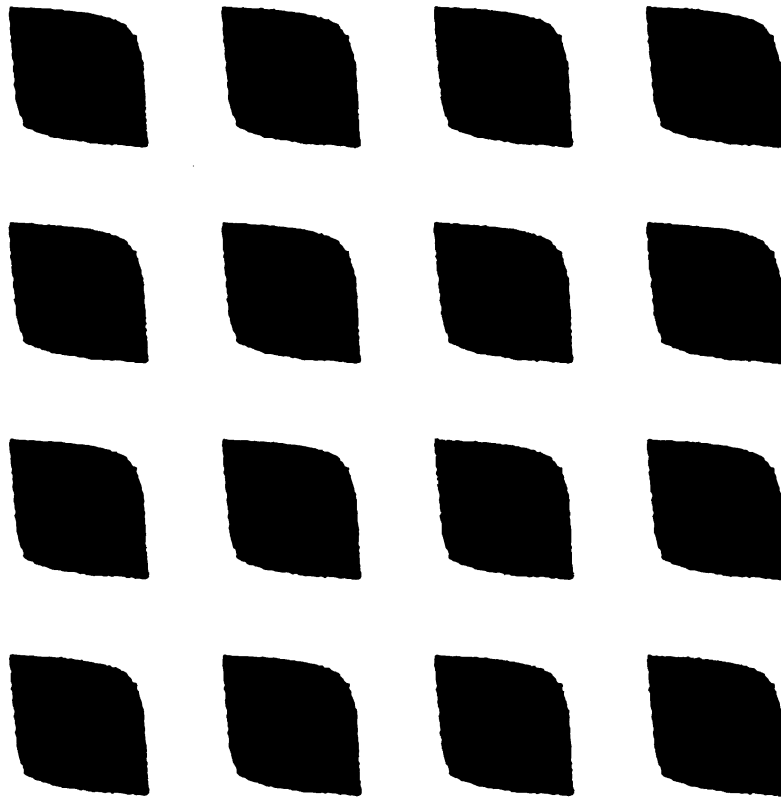


Figure 6.12. Schematic of the microstructure layout for a volume fraction 0.6 with equal macroscopic pressure gradients of 1N/m^2 in the horizontal and vertical directions.

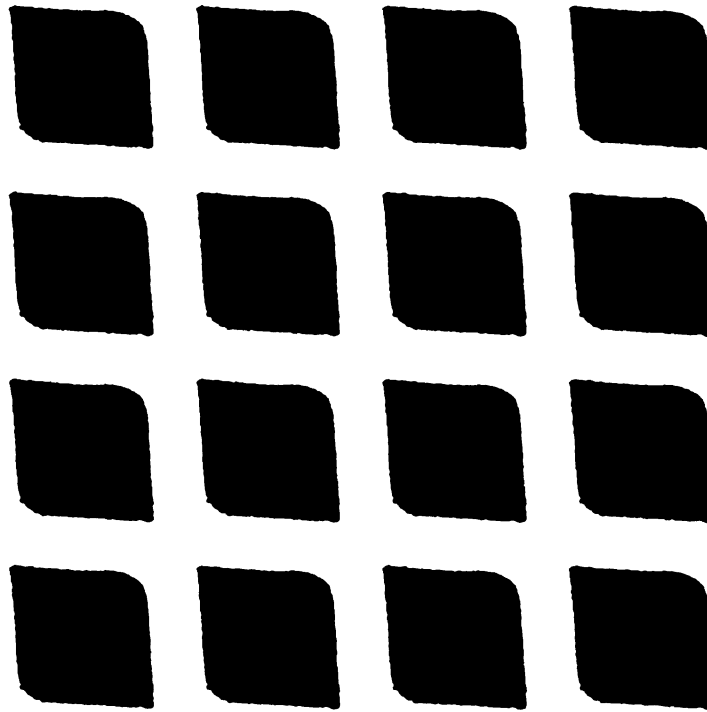


Figure 6.13 Schematic of the microstructure layout for volume fraction of 0.7 with equal macroscopic pressure gradients of 1N/m^2 in the horizontal and vertical directions.

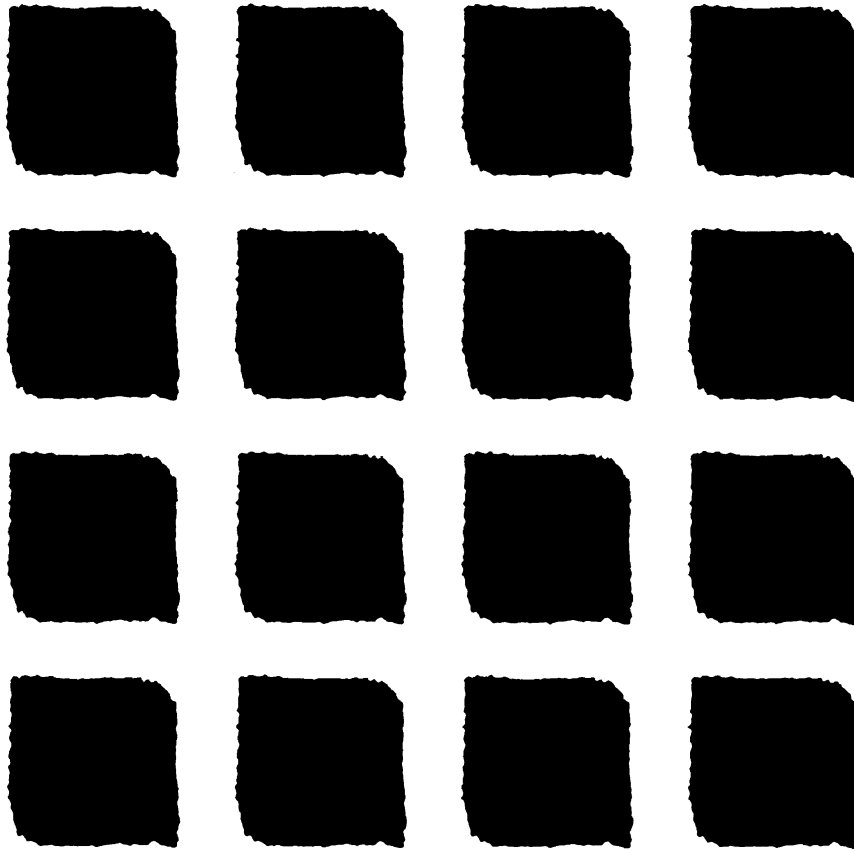


Figure 6.14. Schematic of the microstructure layout for a volume fraction 0.8 with equal macroscopic pressure gradient of 1N/m^2 in the horizontal and vertical directions.

6.4 Discussion

In this chapter I tried to find an optimal microstructure to minimize the energy losses using topology optimization.

The results show that the elliptic cross section for a lower volume fraction has the least energy loss. This also agrees with the results obtained from shape optimization. For a higher volume fraction, the optimized layout obtained appears as a rectangle with smooth corners. This validates the previous argument made in Chapter 5 that the microstructure may form a channel flow. When the macroscopic pressure gradient is applied along both the horizontal and vertical direction, the optimized layout forms the shape of leaf. In this layout the specific surface which is expressed as the ratio of the pore surface area to the total volume of the periodic cell is less and hence increasing the permeability.

When optimized microstructures obtained from topology optimization were compared with the square array of same porosity, it shows the same trend. When the macroscopic flow is compared for optimized microstructure and square array formed by circular solid region with same porosity, a higher magnitude of velocity is obtained for the optimized microstructure as shown in Figure (6.6). Figure (6.15) shows the macroscopic domain and the applied boundary condition

where $\begin{bmatrix} \nabla_X p_x \\ \nabla_X p_y \end{bmatrix} = \begin{bmatrix} 1 \\ 0 \end{bmatrix}$. Figure (6.16) shows the macroscopic velocity

profile for both the optimized microstructure and the un-optimized microstructure for $V_{frac} = 0.5$ at the dashed line shown in Figure (6.16). Here the un-optimized microstructure is formed by square periodic cell with circular solid region of identical porosity as the optimized microstructure.

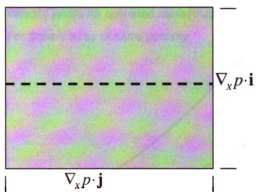


Figure 6.15 Schematic of the macroscopic layout with applied boundary conditions

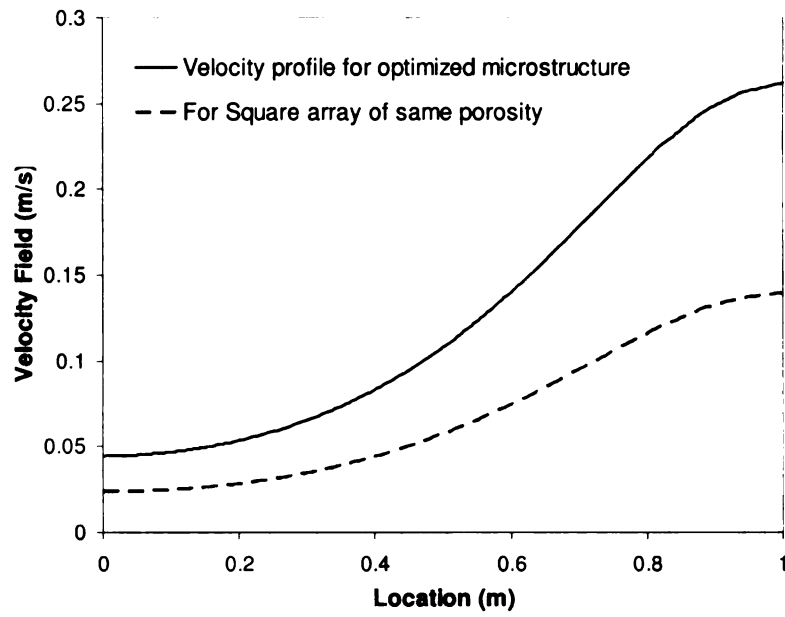


Figure 6.16 Comparison of the velocity profiles in the macroscopic domain for a microstructure formed from a cross section obtained from topology optimization with the velocity field obtained for a square array of same porosity

CHAPTER 7

TOPOLOGY OPTIMIZATION OF SOLUTE TRANSPORT IN POROUS MEDIA TO MAXIMIZE “DISPERSIVE POWER”

7.1 Introduction

Solute transport in porous media and finding the optimal layout using topology optimization is the subject of this section. Topology optimization is a layout optimization technique that was originally developed to design mechanical structures (Bendsøe and Kikuchi, 1988). Topology optimization was then used to find the layout of the microstructure or the base cell of the material. Examples of such works include Sigmund (Sigmund and Torquato 1996) who propose to design microstructures of materials with negative thermal expansion, Larsen (Larsen 1996) to design material that yields negative Poisson’s ratio and Diaz and Bénard (Diaz and Bénard 2003) to design material that matches prescribed elastic properties.

The problem is formulated in a similar manner to a standard optimization problem, in which the Method of Moving Asymptotes (MMA) is used for optimization. The derivatives of the objective function with respect to the design variables were computed using an adjoint method as proposed by Olesen, Okkel and Bruus (Olesen 2006). Figure

(7.1) shows the flowchart of step by step approach to find the optimal microstructure using topology optimization.

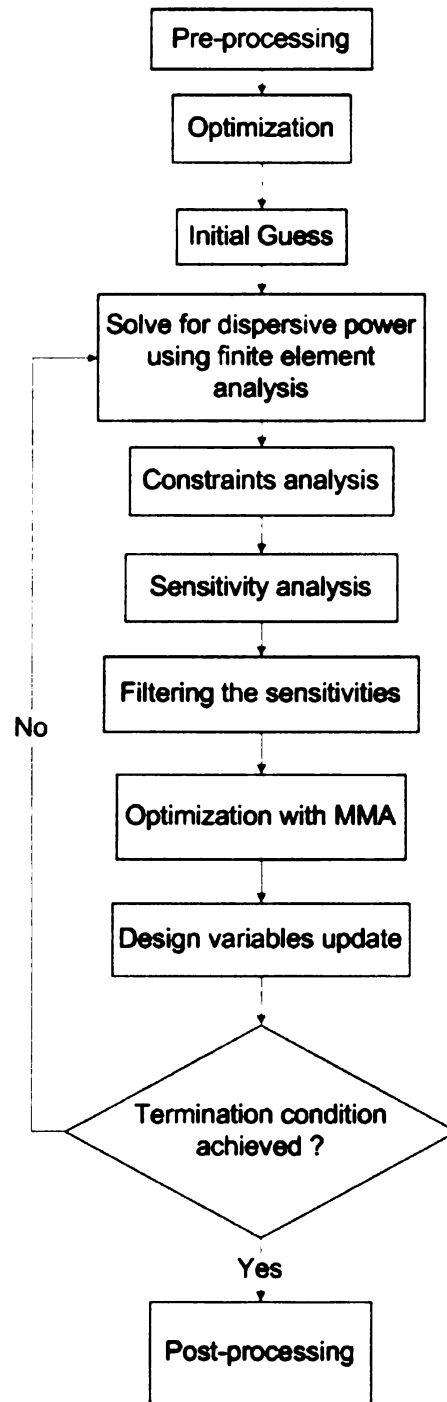


Figure 7.1 Flowchart of the topology optimization methodology employed

7.2 Formulation of the optimization problem

In the analysis, the macroscopic domain (Ω_M) is assumed to be homogeneous with periodic microscopic cells (Ω_m). The microscopic cell has two distinct regions: a solid region (Ω_s) and a fluid region (Ω_f) such that $\Omega_m = \Omega_s \cup \Omega_f$ and $\Omega_s \cap \Omega_f = 0$. The interface between the solid-fluid in each periodic cell is Γ_{sl} and the interface between two periodic cells is denoted by Γ_{cell} .

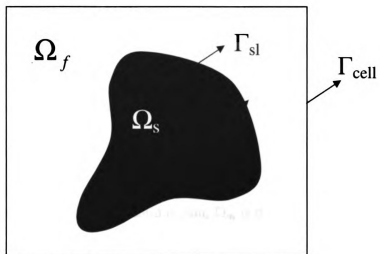


Figure 7.2 Schematic of a periodic microscopic cell.

7.2.1 Maximizing “Dispersive power”

The main objective here is to maximize mixing or “dispersive power”.

$$\text{max: } \mathcal{S}_{dispersive}$$

subjected to: volumetric and geometric constraints

$$\frac{\Omega_s}{\Omega_m} \geq V_{frac} \quad (7.1)$$

where Ω_s is the volume of the solid region, Ω_m is the total volume of the cell, and V_{frac} is value ($0 < V_{frac} < 1$) specifying the minimum solid volume. The constraint in equation (7.1) restricts the minimum volume of solid region to V_{frac} .

The governing equation for the solute transport along with the Stokes equation and the incompressibility constraints are for the volumetric concentration c of the solute in the fluid region expressed as

$$\langle \mathbf{u} \rangle \cdot \nabla_X c^{(0)} = \nabla_X \cdot \left[\mathbf{D} \cdot \nabla_X c^{(0)} \right] \quad (7.2)$$

where $\langle \mathbf{u} \rangle = \langle \mathbf{u}^{(0)} \rangle + \langle \mathbf{u}^{(1)} \rangle$ and for weak inertia flow $\langle \mathbf{u}^{(1)} \rangle \approx 0$

(Mei and Auriault 1991). $\mathbf{u}^{(0)}$ is computed from the homogenized Navier-Stokes equation and the incompressibility constraint as derived in Chapter 2.

\mathbf{D} in Equation (7.2) is the effective dispersion tensor (Mei 1992)

expressed as

$$\mathbf{D} = D\langle \mathbf{Z} \rangle \quad (7.3)$$

where \mathbf{Z} is “characteristic dispersivity tensor” given as,

$$\mathbf{Z} = \left(\frac{1}{2} (\nabla_x \mathbf{N} + \nabla_x \mathbf{N}^T) + \mathbf{I} \right) - \frac{1}{2} \left(\left(\mathbf{u}^{(0)} \mathbf{N} \right) + \left(\mathbf{u}^{(0)} \mathbf{N} \right)^T \right) \quad (7.4)$$

And D is the molecular diffusivity and \mathbf{N} is any vector satisfying the equations

$$\nabla_x \left(D(\mathbf{I} + \nabla_x \cdot \mathbf{N}) \right) - \mathbf{u}^{(0)} \nabla_x \cdot \mathbf{N} = \mathbf{u}^{(0)} \quad (7.5)$$

$$-\langle \mathbf{u}^{(0)} \rangle / n - \alpha (\nabla_x \mathbf{N} + 1) \text{ in } \Omega_m \quad (7.6)$$

where n is the porosity, and

$$D(\mathbf{I} + \nabla_x \cdot \mathbf{N}) \cdot \mathbf{n} = 0 \text{ on } \Gamma.$$

\mathbf{N} is Ω_m -periodic and $\langle \mathbf{N} \rangle = 0$.

Additional governing equations to solve $\mathbf{u}^{(0)}$ are the homogenized Navier-Stokes equation and the incompressibility constraint as derived in Chapter 2. For generality the fluid flow through the solid region is subjected to a friction force, which is proportional to the fluid velocity.

$$\mu \nabla_x^2 \mathbf{u}^{(0)} - \nabla_x p^{(1)} = \nabla_X p^{(0)} - \alpha \mathbf{u}^{(0)} \text{ in } \Omega_m \quad (7.7)$$

$$\nabla_x \cdot \mathbf{u}^{(0)} = 0 \text{ in } \Omega_m \quad (7.8)$$

where $\nabla_X p^{(0)}$ is the pressure gradient across the macroscopic domain and is applied as an source term. The above governing equations are valid in both solid and fluid phases since the penalty term α , which is a function of the design variable ρ , is used to extend the domain of validity to all the cell domain. The design variable ρ controls the phase of the medium as follows;

$$\rho(x) = \begin{cases} 0 & \text{if } x \in \Omega_s \\ 1 & \text{if } x \in \Omega_f \end{cases} \quad (7.9)$$

Following reference Borrvall (Borrvall 2003) and Olesen (Olesen 2005), the penalty term α and design variable ρ are related by the convex interpolation.

$$\alpha(\rho) \equiv \alpha_{\min} + (\alpha_{\max} - \alpha_{\min}) \frac{q[1-\rho]}{q+\rho} \quad (7.10)$$

where q is a real and positive parameter used to tune the shape of the penalty term and taken as 0.01. In this work α_{\min} is taken as zero and

α_{\max} is a large number (10^5).

The boundary conditions are

$$\mathbf{u}^{(0)} = \mathbf{u}^{(1)} = \dots = 0 \text{ on } \Gamma \text{ (solid fluid interface),} \quad (7.11)$$

$\mathbf{u}^{(0)}, \mathbf{u}^{(1)} \dots$ and $p^{(0)}, p^{(1)} \dots$ are Ω_m -periodic.

$\mathfrak{S}_{dispersive}$ is the normalized value of “dispersive power”,

which is computed by multiplying equation (7.2) with $c^{(0)}$, and integrating

over the entire domain, the following expression for the “dispersive power” is obtained after using Green’s theorem:

$$\langle \mathbf{u} \rangle \int_{\Omega_m} \nabla_X c^{(0)} \cdot c^{(0)} d\Omega = \int_{\Omega_m} \nabla_X c^{(0)} \cdot \mathbf{D} \cdot \left[\nabla_X c^{(0)} \right]^T d\Omega \quad (7.12)$$

The right hand term is the dispersive power term.

$$\mathfrak{S}_{dispersive} = \int_{\Omega_m} \nabla_X c^{(0)} \cdot \mathbf{D} \cdot \left[\nabla_X c^{(0)} \right]^T d\Omega, \quad (7.13)$$

In dimensionless form, equation (7.13) can be written as,

$$\hat{\mathfrak{S}}_{dispersive} = \int_{\Omega_m} \nabla_X \hat{c}^{(0)} \cdot \hat{\mathbf{D}} \cdot \left[\nabla_X \hat{c}^{(0)} \right]^T d\Omega, \quad (7.14)$$

where $\hat{c}^{(0)}$ and $\hat{\mathbf{D}}$ are dimensionless form of $c^{(0)}$ and \mathbf{D} related by $\hat{c}^{(0)} = c^{(0)} / C$ and $\hat{\mathbf{D}} = \mathbf{D} / D$.

7.2.2 Implementation Issues

A factor that had to be considered in formulating the problem for the optimization is that the microstructure should be discontinuous as shown in Figure (7.2) to model pores in a porous material. To avoid cases of continuous solid regions, the layout is divided into two initial zones. Zone 1 is formed only by fluid material and forms the outer boundary of the periodic cell, whereas Zone 2 is formed on both solid and fluid material as shown in Figure (7.3). In Zone 1 α value is taken as zero.

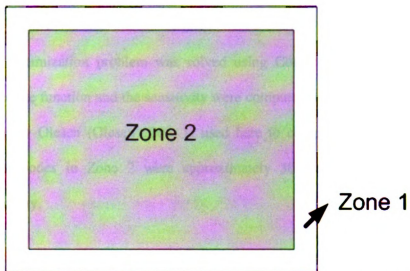


Figure 7.3 Schematic of a periodic microscopic cells with the zones to avoid continuous solid region

7.3 Example Problems

The optimization problem was solved using Comsol and Matlab. The objective function and the sensitivity were computed using Comsol. Work done by Olesen (Olesen 2005) is used here to compute the sensitivity. Total nodes in Zone 2 were approximately 30 elements along each boundary.

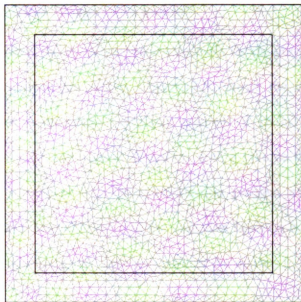


Figure 7.4 Schematic of the unstructured triangular mesh used in the finite element analysis.

7.3.1 Maximizing “Dispersive power”

In this section, the optimized microstructures for the porous media that minimize dispersion are shown. Figure (7.5) shows the microstructure obtained when a macroscopic pressure gradient of 1N/m^2 is applied in both the horizontal and vertical directions with a volume fraction of the solid region limited to 0.7. The concentration gradient of 1 mol/m^3 is applied in horizontal direction and the objective function is set in such a way that the microstructure should maximize the mixing in the horizontal direction.

A sharp change in the microstructure is seen when the volume fraction is reduced to 0.3 as shown in Figure (7.6).

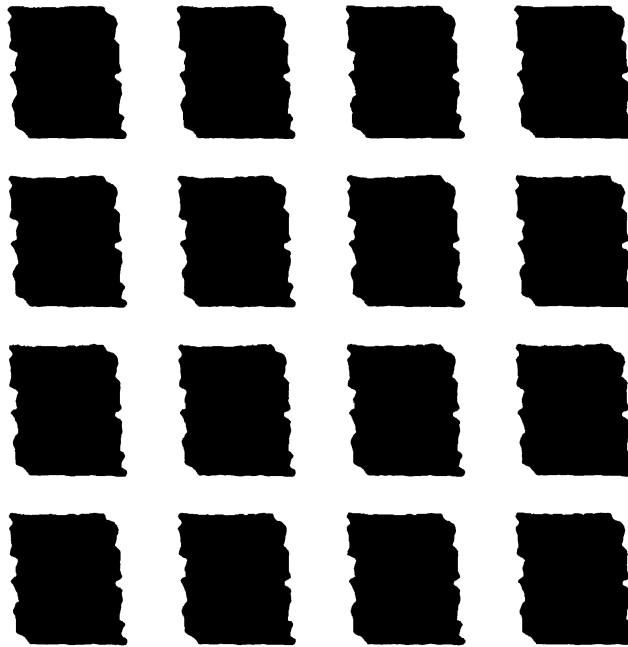


Figure 7.5 Schematic of microstructure layout for volume fraction 0.7 with equal macroscopic pressure gradient of 1N/m^2 in the horizontal and vertical directions and a concentration gradient in the horizontal direction.

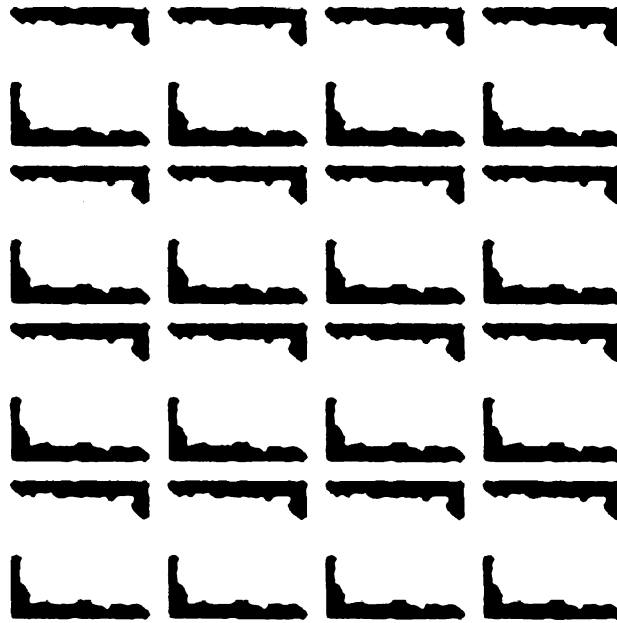


Figure 7.6 Schematic of the microstructure layout for a volume fraction 0.3 with equal macroscopic pressure gradient of 1N/m^2 in the horizontal and vertical directions and a concentration gradient in the horizontal direction

7.4 Discussion

In this chapter we tried to find an optimal microstructure to maximize mixing using topology optimization. Due to the limitations of the solver used, the results for maximizing dispersive power cannot be solved for a fine-mesh. The results obtained and shown in this chapter provide a hint of the appearance of the porous medium. In the results shown in Figures (7.5) – (7.6) the inflow is at negative 45 degree to the horizontal and the aim was to distribute the solute in the horizontal direction. In Figure (7.6) the microstructure diverts the flow as much as possible to the horizontal direction. For a lower volume fraction the solid materials form a wall around the boundary of zone 1 and zone 2 to restrict the flow in vertical direction. For a higher velocity in horizontal direction the longitudinal dispersion tensor will be higher and hence maximize the solute flow in that direction.

CHAPTER 8

THEORY FOR MULTIPHASE FLUID FLOW IN POROUS MEDIA

8.1 Introduction

Practical applications of porous materials often involve two or more fluids. For example, use of porous material as a filter in the petroleum industry often involve oil and water. As discussed in Chapter 1, naturally occurring porous materials are heterogeneous there have been many theoretical attempts to deduce the phenomenological equations by starting from the micro-scale based on the idealized models of the microstructure. In this chapter we review the existing theories for deriving the Stokes equation for two phase flow in the micro-scale and derive the phenomenological equations that describe the macroscopic behavior of the porous media. The governing equations are developed using mixture model. Shape optimization is used to determine the optimal microstructure for porous media that will minimize the dissipation power, for a given flow condition.

8.2 Derivation of Effective Permeability Tensor using Mixture Model

In two phase flow problems, the average velocity of one phase is typically distinctly different from the other phase (Kleinstreuer 2003). Also, one or more physical properties such as density or viscosity of each phase distinctly differ in magnitude. The macroscopic domain (Ω_M) is assumed to be homogeneous with periodic microscopic cells (Ω_m). The microscopic cell has two distinct regions: a solid region (Ω_s) and a mixture fluid region (Ω_{fmix}) such that $\Omega_m = \Omega_s \cup \Omega_{fmix}$ and $\Omega_s \cap \Omega_{fmix} = 0$. The Mixture model computes the average behavior of a two phase flow field as a single phase flow that is rather general and useful as shown in Figure (8.1), where the mean density (ρ_{mix}^f) can be expressed as a function of the volume fraction V_f ($V_f = V_2/V$). The effective mixture density in terms of volume fraction is given as

$$\rho_{mix}^f = V_f \rho_2^f + (1 - V_f) \rho_1^f \quad (8.1)$$

where the indices mark the individual phases $i=1$ (carrier fluid) and $i=2$ (dispersed phase). For example ρ_1^f is the density for fluid phase 1 and ρ_2^f is the density for fluid phase 2.

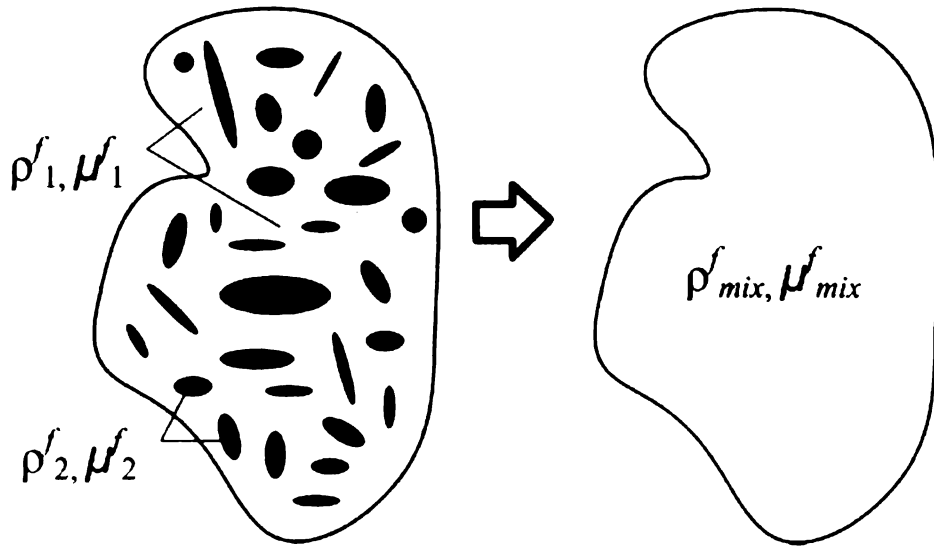


Figure 8.1 Schematic of the process of representing a two phase flow with an equivalent a single phase flow model.

The average steady-state mixture continuity and momentum equations (Ishii, 2006) are given as

$$\nabla \cdot \left(\rho_{mix}^f \mathbf{u}_{mix} \right) = 0 \text{ in } \Omega_{fmix} \quad (8.2)$$

$$\mu_{mix}^f \nabla^2 \mathbf{u}_{mix} - \nabla p_{mix} = \quad (8.3)$$

$$\rho_{mix}^f \mathbf{u}_{mix} \cdot \nabla \mathbf{u}_{mix} + \nabla \cdot \left[\frac{V_f \rho_1^f \rho_2^f}{(1-V_f) \rho_{mix}^f} \tilde{\mathbf{u}}_{21}^2 \right] \text{ in } \Omega_{fmix}$$

where \mathbf{u}_{mix} is defined as

$$\mathbf{u}_{mix} = \frac{\rho_1^f (1-V_f)}{\rho_{mix}^f} \mathbf{u}_1 + \frac{\rho_2^f V_f}{\rho_{mix}^f} \mathbf{u}_2 \quad (8.4)$$

Gravity and mass transfer between two fluids are ignored. $\tilde{\mathbf{u}}_{21}$ is the slip velocity between two fluid phases. It is also assumed that the solid phase is chemically inert. For Newtonian fluids the momentum transfer due to shear stresses within fluid is negligible as compared with the momentum transfer to the solid matrix (Allen 1985). So

$$\nabla \cdot \left[\frac{V_f \rho_1^f \rho_2^f}{(1-V_f) \rho_{mix}^f} \tilde{\mathbf{u}}_{21}^2 \right] \approx 0 \quad (8.5)$$

and equation 8.3 reduces to

$$\mu_{mix}^f \nabla^2 \mathbf{u}_{mix} - \nabla p_{mix} = \rho_{mix}^f \mathbf{u}_{mix} \cdot \nabla \mathbf{u}_{mix} \text{ in } \Omega_{fmix} \quad (8.6)$$

The perturbation expansion for \mathbf{u}_{mix} and p_{mix} is as follows,

$$\mathbf{u}_{mix} = \mathbf{u}_{mix}^{(0)} + \varepsilon \mathbf{u}_{mix}^{(1)} + \varepsilon^2 \mathbf{u}_{mix}^{(2)} + \varepsilon^3 \mathbf{u}_{mix}^{(3)} \quad (8.7)$$

$$p_{mix} = p_{mix}^{(0)} + \varepsilon p_{mix}^{(1)} + \varepsilon^2 p_{mix}^{(2)} + \varepsilon^3 p_{mix}^{(3)} \quad (8.8)$$

The differential term related the two length scales as a function of ε

$$\nabla = \nabla_x + \varepsilon \nabla_X \quad (8.9)$$

Substituting perturbation expansions for \mathbf{u}_{mix} and p_{mix} in equation 8.6 and 8.2

$$\begin{aligned} & \mu_{mix}^f \left(\nabla_x + \varepsilon \nabla_X \right)^2 \left(\mathbf{u}_{mix}^{(0)} + \varepsilon \mathbf{u}_{mix}^{(1)} + \varepsilon^2 \mathbf{u}_{mix}^{(2)} + \varepsilon^3 \mathbf{u}_{mix}^{(3)} \right) - \quad (8.10) \\ & \left(\nabla_x + \varepsilon \nabla_X \right) \left(p_{mix}^{(0)} + \varepsilon p_{mix}^{(1)} + \varepsilon^2 p_{mix}^{(2)} + \varepsilon^3 p_{mix}^{(3)} \right) = \\ & \rho_{mix}^f \left(\mathbf{u}_{mix}^{(0)} + \varepsilon \mathbf{u}_{mix}^{(1)} + \varepsilon^2 \mathbf{u}_{mix}^{(2)} + \varepsilon^3 \mathbf{u}_{mix}^{(3)} \right) \cdot \\ & \left(\nabla_x + \varepsilon \nabla_X \right) \left(\mathbf{u}_{mix}^{(0)} + \varepsilon \mathbf{u}_{mix}^{(1)} + \varepsilon^2 \mathbf{u}_{mix}^{(2)} + \varepsilon^3 \mathbf{u}_{mix}^{(3)} \right) \end{aligned}$$

and

$$\left(\nabla_x + \varepsilon \nabla_X \right) \cdot \left(\rho_{mix}^f \left(\mathbf{u}_{mix}^{(0)} + \varepsilon \mathbf{u}_{mix}^{(1)} + \varepsilon^2 \mathbf{u}_{mix}^{(2)} + \varepsilon^3 \mathbf{u}_{mix}^{(3)} \right) \right) = 0 \quad (8.11)$$

Assuming the mixture density is not a function of macroscale X , from Equation 8.10 and 8.11, at orders from $O(\varepsilon^0)$ I get

$$\mu_{mix}^f \nabla_x^2 \mathbf{u}_{mix}^{(0)} - \nabla_x p_{mix}^{(1)} = \nabla_X p_{mix}^{(0)} \text{ in } \Omega_{fmix} \quad (8.12)$$

and

$$\nabla_X \cdot \mathbf{u}_{mix}^{(0)} = 0 \text{ in } \Omega_{fmix} \quad (8.13)$$

and $\mathbf{u}_{mix}^{(0)}, \mathbf{u}_{mix}^{(1)} \dots$ and $p_{mix}^{(0)}, p_{mix}^{(1)} \dots$ are Ω_m -periodic. $p^{(0)}$

is only a function of the large scale X . The needed boundary conditions are

$$\mathbf{u}_{mix}^{(0)} = \mathbf{u}_{mix}^{(1)} = \dots = 0 \text{ on } \Gamma \text{ (solid fluid interface),} \quad (8.14)$$

In equation 8.10 and 8.11, $\varepsilon = l/L \ll 1$ is the ratio of two well separated length scales: the micro scale $l \approx O(x)$ and macro scale $L \approx O(X)$. Here the macrostructure is assumed to be homogeneous consisting of periodic micro cells.

Equation 8.12 relates the microscopic fluid flow with the macroscopic pressure gradient. This is similar to the approach taken by Darcy to relate the fluid flow in porous media for a given macroscopic boundary condition. $\mathbf{u}_{mix}^{(0)}$ and $p_{mix}^{(1)}$ can also be expressed in terms of $p_{mix}^{(0)}$

from Darcy's equation,

$$\mathbf{u}_{mix}^{(0)} = -\mathbf{U}_{mix} \cdot \nabla_X p_{mix}^{(0)}, \quad (8.15)$$

and

$$p_{mix}^{(1)} = \mathbf{a}_{mix} \cdot \nabla_X p_{mix}^{(0)}, \quad (8.16)$$

where \mathbf{U}_{mix} is the characteristic mixture velocity and \mathbf{a}_{mix} is the characteristic mixture pressure can be obtained from the solution of

$$\mu_{mix}^f \nabla_x^2 \mathbf{U}_{mix} - \nabla_x \mathbf{a}_{mix} = \mathbf{I} \quad (8.17)$$

and

$$\nabla_x \cdot \mathbf{U}_{mix} = 0. \quad (8.18)$$

The boundary conditions applied are no slip and periodic boundary conditions for \mathbf{U}_{mix} and \mathbf{a}_{mix} .

The effective permeability of the porous media is computed from

$$\mathbf{K}_{mix} = \mu_{mix}^f \langle \mathbf{U}_{mix} \rangle \quad (8.19)$$

Equations (8.17 - 8.18) are similar to the single phase equations (2.9 – 2.10), where the velocity, pressure of a single phase is replaced by a mixture velocity and pressure. This equation is solved to the effective properties of the mixture fluid.

Shape optimization problem is used to find the optimal microstructure where various shapes described parametrically are studied. Since the governing equations are very similar to the governing equation for single phase fluid, this work can be taken as an extension of the shape optimization work done in earlier chapters. The Method of Moving Asymptotes as proposed by Krister Svanberg is used for optimization. The derivatives of the objective function with respect to the design variables were computed using finite differences.

8.3 Identifying the Periodic Cell

. In the analysis, the macroscopic domain (Ω_M) is assumed to be homogeneous. The microscopic cell (Ω_m) has two distinct regions: a solid region (Ω_s) and a mixture fluid region (Ω_{mix}) such that $\Omega_m = \Omega_s \cup \Omega_{mix}$ and $\Omega_s \cap \Omega_{mix} = 0$. P , l and L are the characteristic pressure, micro length and macro length scales. Two scales are introduced: a small scale ($x \approx O(l)$) and a large scale ($X \approx O(L)$). The multiscale coordinates are related by $X = \varepsilon x$ in the asymptotic expansion.

The homogeneous macroscopic domain is formed of periodic microscopic cells as shown in Figure (8.2). Each cell is identified by the geometric parameters such as l , h , a , b , and θ . L is the cell length, h is the cell height, a is the major axis or length of the solid region, b is the minor axis or height of the solid region, and θ is the angle between l and h in each cell. Three different shapes for the solid region such as circle ($a = b$), ellipse (Figure (8.3)), and rectangle (Figure (8.4)) are considered below.

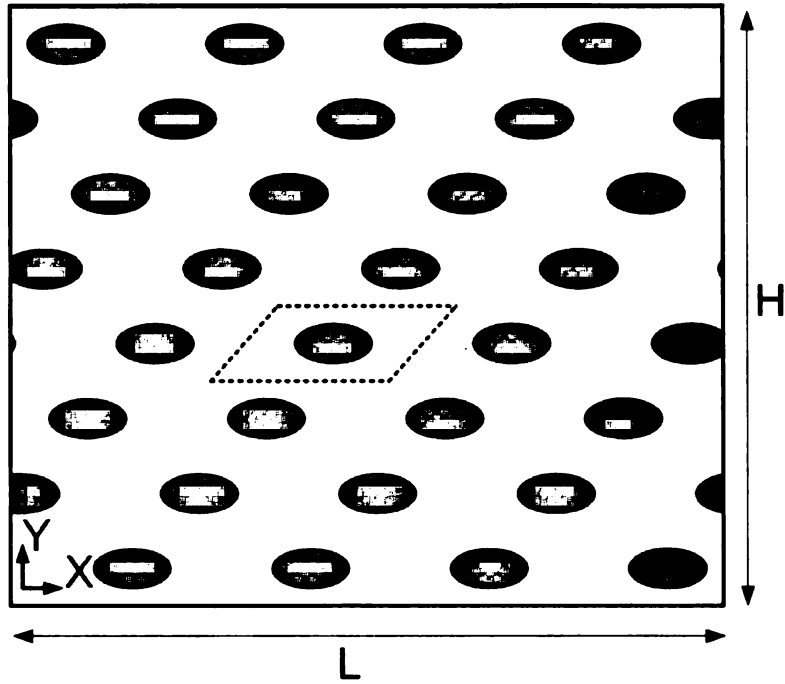


Figure 8.2 Schematic of a homogeneous macroscopic domain studied consisting of periodic microscopic cells.

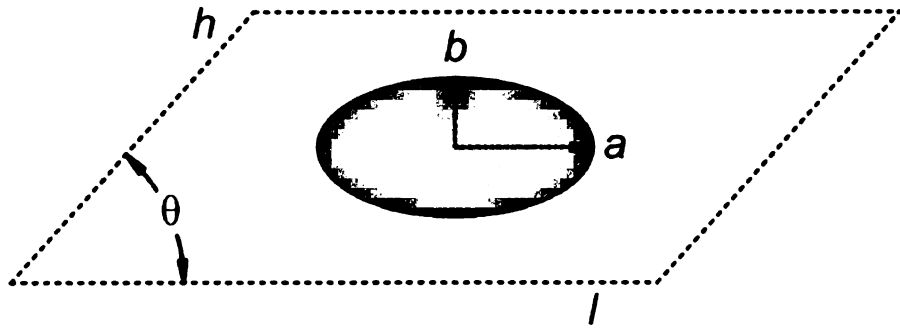


Figure 8.3 Schematic of periodic microscopic cells with an elliptic solid region

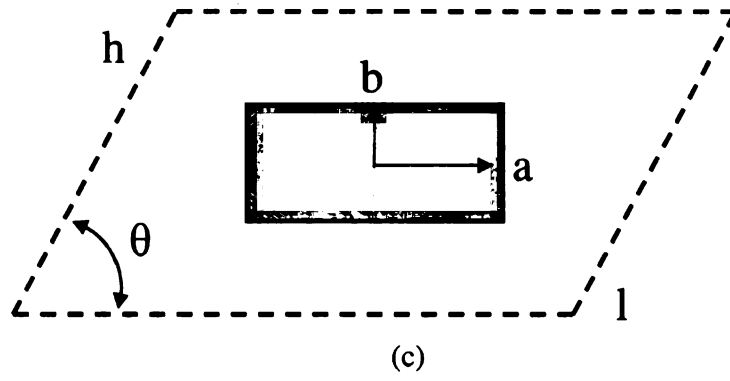


Figure 8.4 Schematic of periodic microscopic cells with a rectangular solid region

8.4 Formulation of the optimization problem

In this section the aim is to find a microstructure of the periodic cell that minimizes the dissipation power for multiphase fluid flow with the added constraint of volume fraction using shape optimization.

8.4.1 Minimize dissipation power for multiphase fluid flow

The complete formulation of the optimization problem is stated as follows:

Find θ , h , a and b for a given value of l , $\nabla_X p^{(0)}$ and $\nabla_Y p^{(0)}$ that will

minimize: $\mathfrak{J}_{dissipation}$

subjected to: volumetric and geometric constraints

$$\text{Constraint 1: } \frac{\Omega_s}{\Omega_m} \geq V_{frac} \quad (8.20)$$

$$\text{Constraint 1: } a < \frac{l}{2}$$

$$\text{Constraint 1: } b < \frac{h \sin \theta}{2}$$

where Ω_s is the volume of the solid region, Ω_m is the total volume of the cell, and V_{frac} is value ($0 < V_{frac} < 1$) specifying the minimum solid volume.

The first constraint in equation (8.20) restricts the minimum volume of

solid region to V_{frac} . The next two constraints are imposed to insure the continuity of each phase.

$\mathfrak{S}_{dissipation}$ is the normalized value of dissipation power for the mixture fluid, which is computed by multiplying equation (8.12) with $\mathbf{v}_{mix}^{(0)}$, where $\mathbf{v}_{mix}^{(0)}$ is any periodic mixture velocity satisfying equation (8.15) and the periodic boundary condition, and integrating over the entire domain

$$\mathfrak{S}_{dissipation} = \mu_{mix}^f \int_{\Omega_m} \nabla_x \mathbf{u}_{mix}^{(0)} : (\nabla_x \mathbf{v}_{mix}^{(0)})^T d\Omega \quad (8.21)$$

where the double dot operator ($:$) is defined here as $\boldsymbol{\alpha} : \boldsymbol{\beta} = \alpha_{ij} \beta_{ji}$.

8.5 Example Problems

The results shown in this section are all for a limiting volume fraction of 0.3 and fixed value of 0.002m for l . Mixture of water and crude oil are solved here for volume fraction of 0.2. The physical properties of water are density 1000 Kg/m³ and dynamic viscosity of 0.001 Pa.s. Physical properties of crude oil are density 915 Kg/m³ and dynamic viscosity of 0.02 Pa.s. The properties of water and crude oil are taken at 60° F. The macroscopic equation is solved for a domain of 1x1 m². The applied pressure gradient is 0.1 N/m³ applied along X axis.

8.5.1 Minimize dissipation power for multiphase fluid flow

The optimal microstructure of the porous medium for the desired objective function as discussed in section 8.3 for volume fraction of 0.3 for solid region is shown in Figure (8.5). The dimensions of the microstructures are shown in Table (8.1) where l , h , a , b and θ are the length, height, major axis, minor axis and angle between length and height for the periodic cell. The dependence of the step size and initial value were in the optimization algorithm were verified by varying it those for two different cases. For case 1 the step size is set to 0.1 and initial aspect ratio is 1, radius (major axis, minor axis) set to 5×10^{-4} m and θ value to 90° . For case 2 the step size is set to 0.5 and initial aspect ratio is 1, radius (major axis, minor axis) set to 7×10^{-4} m and θ value to 90° . The iteration history for the different cases are shown in Figure (8.5 – 8.6) for circular, elliptic and rectangular solid region.

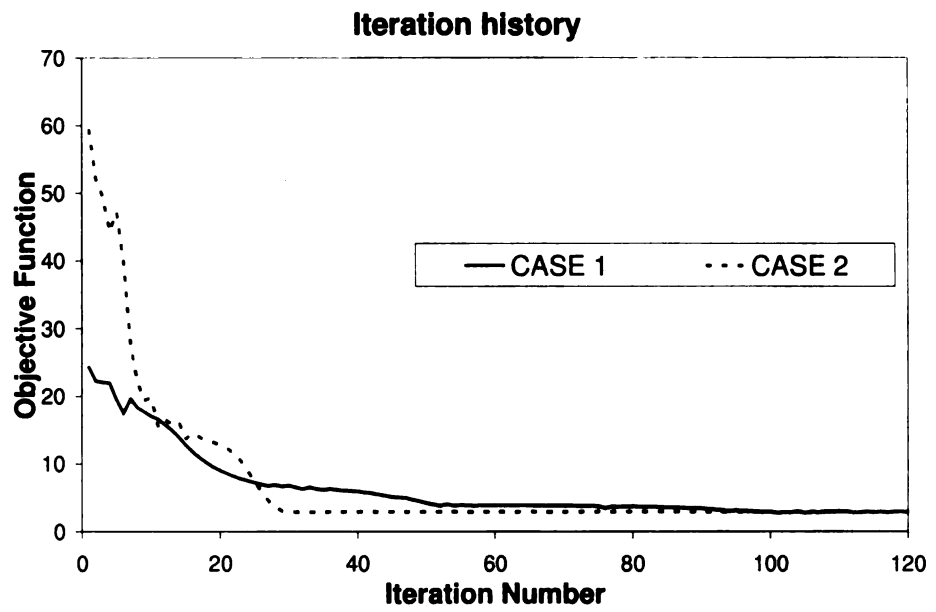


Figure 8.5 Schematic of the iteration history for a circular solid region with varied step size and initial conditions.

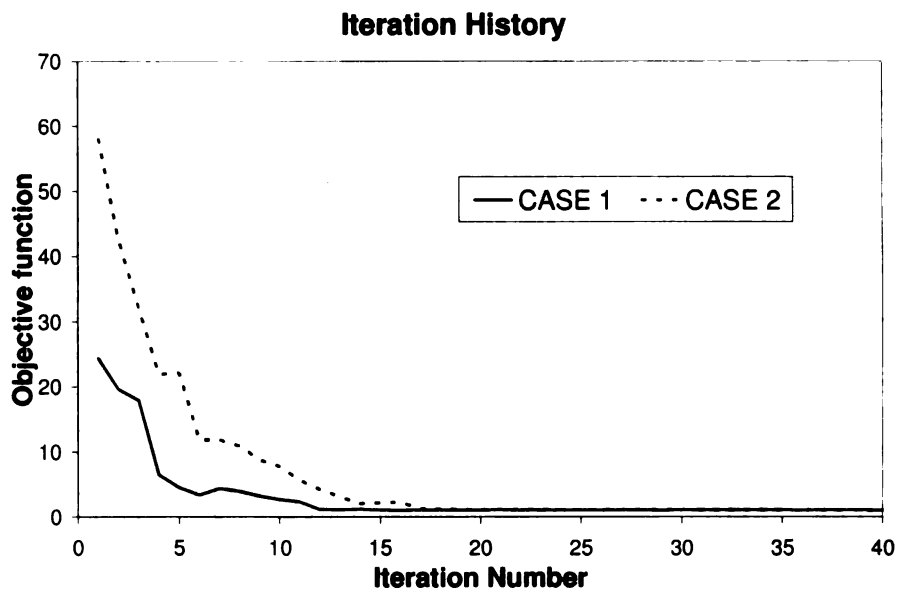


Figure 8.6 Schematic of the iteration history for an elliptic solid region with varied step size and initial conditions.

Iteration history

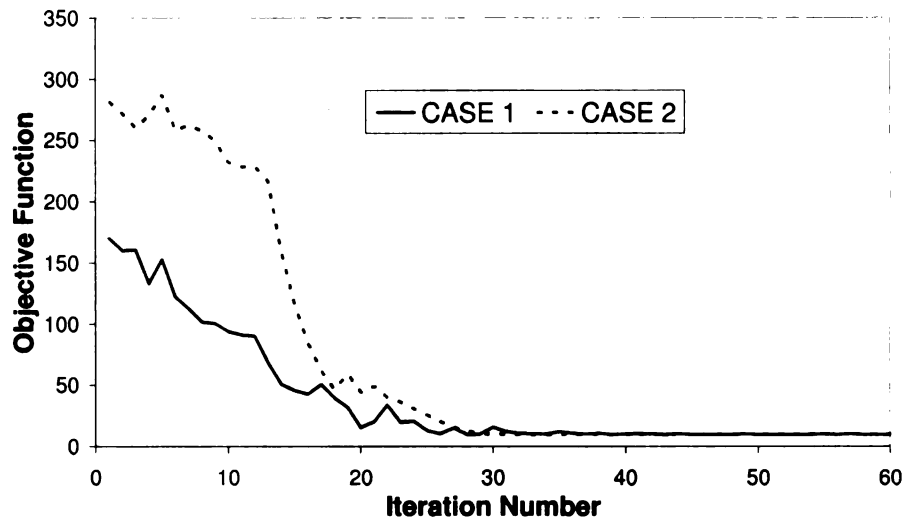


Figure 8.7 Schematic of the iteration history for a rectangular solid region with varied step size and initial conditions.

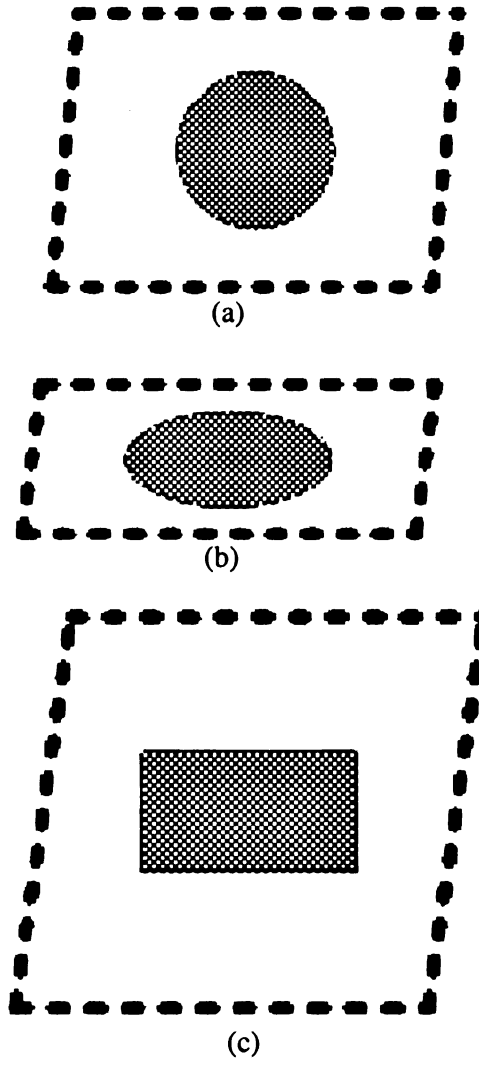


Figure 8.8 a-c. Schematic of the optimal periodic cells obtained after optimization

Table 8.1 Dimensions of the microstructures shown in Figure (8.5)

Figure (9.2)	h/l	a/l	b/l	θ
(a)	0.73	0.21		84.4
(b)	0.39	0.26	0.12	82.7
(c)	0.96	0.26	0.14	81.9

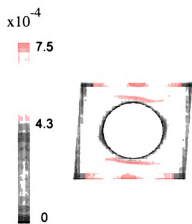
The average effective permeability computed for the microstructures

shown in Figure (8.8) a, b and c are $\langle \mathbf{K}_{mix} \rangle = 1(10^{-6}) \begin{bmatrix} 0.1358 & 0 \\ 0.0303 & 0 \end{bmatrix} \text{ m}^2$,

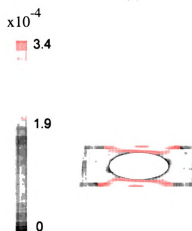
$\langle \mathbf{K}_{mix} \rangle = 1(10^{-6}) \begin{bmatrix} 0.4045 & 0 \\ 8.5826e-6 & 0 \end{bmatrix} \text{ m}^2$ and

$\langle \mathbf{K}_{mix} \rangle = 1(10^{-6}) \begin{bmatrix} 0.7727 & 0 \\ 0.0072 & 0 \end{bmatrix} \text{ m}^2$. Figure (8.9) shows the velocity

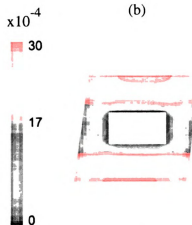
distribution for the mixture fluid.



(a)

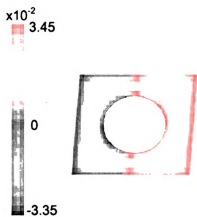


(b)

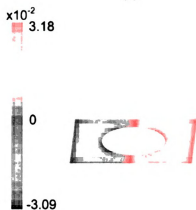


(c)

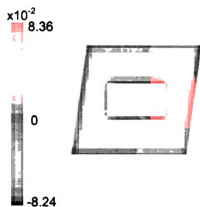
Figure 8.9 a-c. Schematic of velocity distribution of fluid mixture for microstructures shown in Figure (8.8)



(a)



(b)



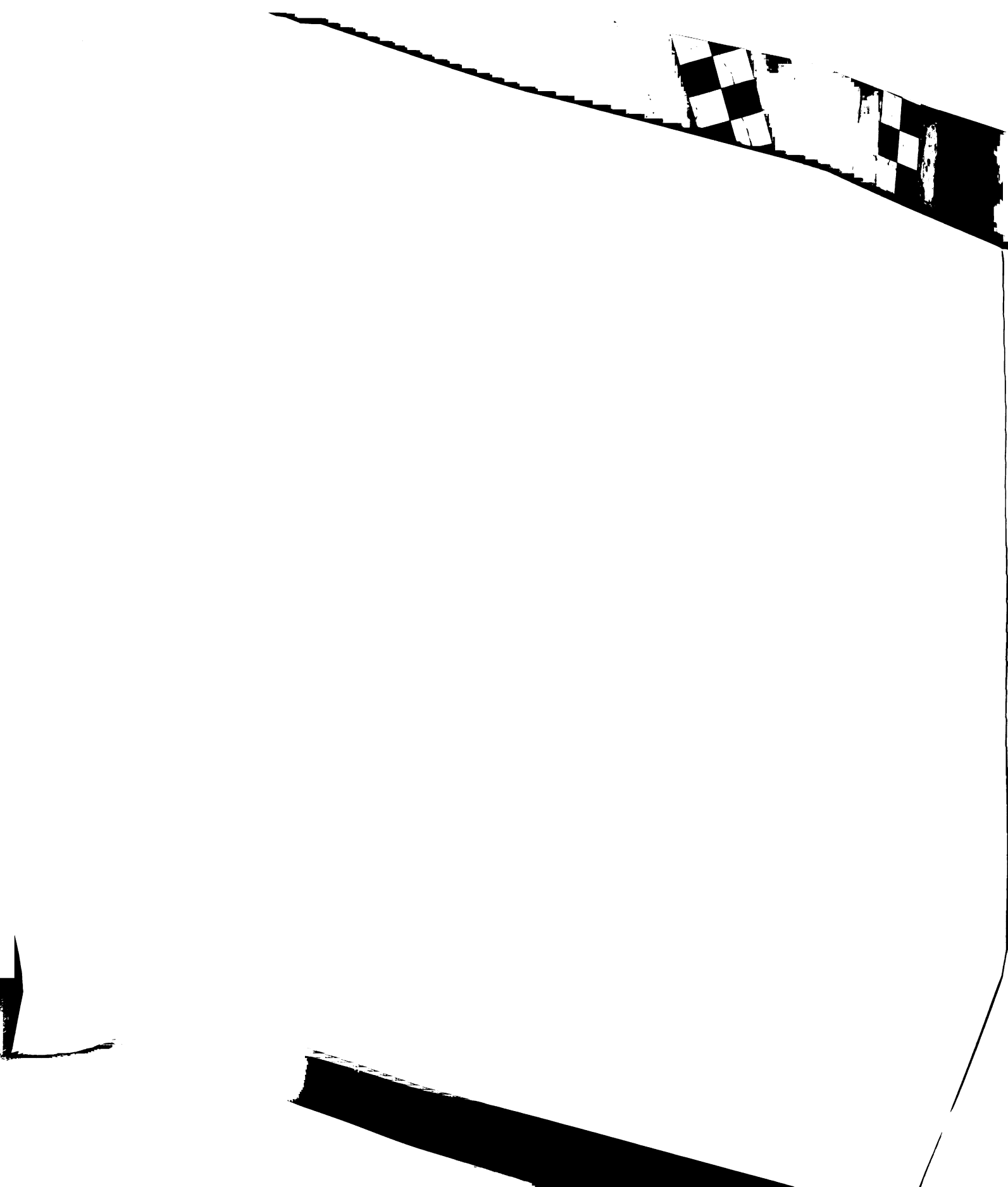
(c)

Figure 8.10 a-c. Schematic of pressure distribution of fluid mixture for microstructures shown in Figure (8.8)

The optimal values of normalized dissipation power evaluated are tabulated in Table (8.2). The dissipation power tabulated is normalized with the dissipation power for elliptic solid region. A possible reason for the high dissipation power observe in a rectangular solid region is because of the presence of a sharp edge. Also due to the flat surface the stagnation point is spread over a area which adds to the energy loss.

Table 8.2 Optimized value of normalized dissipation power and normalized dispersion power for the microstructures as shown in Figure (8.8)

Figure (8.8)	$\mathfrak{S}_{dissipation}$
(a)	2.85
(b)	1
(c)	9.83



8.6 Discussion

In the last two chapters a theory that governs the multiphase fluid flow in a porous media is presented and the partial differential equations are used in an algorithm to design porous media. The governing equation developed using mixture model gives a very approximate behavior of the multiphase fluid flow in a porous media and do not allow to show phase separation since the divergence of the slip velocity was set to zero. Commercial software Fluent was used to solve the differential equations using the finite volume method. After optimization, the microstructure with an elliptic microstructure shows the least energy loss. From Figure (8.8) it can also be added that for microstructure with elliptic solid region the velocity profile shows less variance as compared with other two microstructures. For a microstructure with rectangular solid region, the velocity profile is more that of a channel flow.

When the macroscopic flow is compared (figure 8.12) for optimized microstructure obtained from shape optimization with square array formed by circular solid region with same porosity, a higher magnitude of velocity is obtained for the optimized microstructure as shown in Figure (8.8). The mixture velocity is obtained from the Darcy's equation solved at the macroscopic domain shown in Figure (8.11). The applied boundary

condition where
$$\begin{bmatrix} \nabla_X p_x \\ \nabla_X p_y \end{bmatrix} = \begin{bmatrix} 0.1 \\ 0 \end{bmatrix}.$$

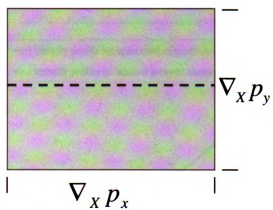


Figure 8.11 Schematic of the macroscopic layout with applied boundary conditions

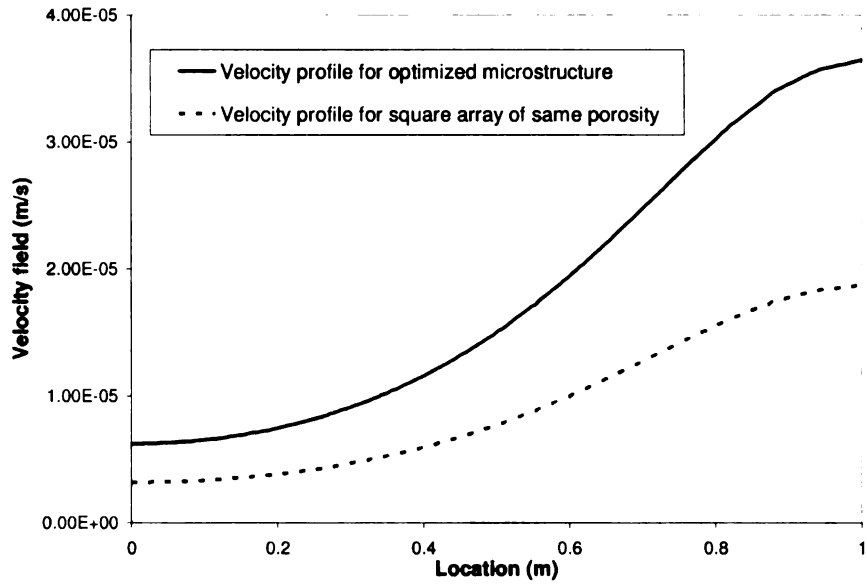


Figure 8.12. Comparison of velocity field in a macroscopic domain for microstructure form with the cross section obtained from shape optimization to minimize energy loss for multiphase flow with that formed by square arrays of the same porosity

CHAPTER 9

SUMMARY AND CONCLUSION

In this work, two methodologies based on the theory of homogenization, combined with two material design are presented, one is based on shape optimization, the other on topology optimization. The theory of homogenization is used to obtain the macroscopic equations and the microscopic equations. The effective properties such as permeability and dispersion of the porous media are computed using the finite element method and compared with experimental results. The method of moving asymptotes is used to find the optimal periodic cell that will satisfy a given criteria such as the maximization of some function of the effective properties, minimization of energy loss, or maximization of solute mixing using both shape optimization and topology optimization.

The expressions derived for the effective dispersion using theory of homogenization gives reasonable argument with experimental results. Figure (3.2) and (3.3) shows that for low Peclet number the computed values obtained from solving equation 3.11 matches closely with the experimental results.

Further work was done to find the optimal microstructure using shape optimization that maximizes the effective properties such as permeability and dispersivity. The magnitude of the effective permeability computed is

and dispersivity. The magnitude of the effective permeability computed is comparable to the work done by Guest and Prévost (Guest 2007). It is observed in Figure (4.8) that the microstructure forms a square array for both the cases with circular and rectangular microstructure. Among the three microstructures, the circular microstructure gives the maximum effective permeability; but the diagonal terms of the permeability tensor are considerably higher than the other microstructures. Overall, the microstructure with rectangular solid region shows the best result. This may be due to the fact that it can be considered as a flow in a channel. One notable observation made from the results obtained from shape optimization for maximizing dispersivity is from Figure (4.13): the angle between the length and the height goes to a lower value for circular and elliptic cross section. But for a rectangular cross section, the θ value approaches 90. This complements the previous argument that it forms a channel flow; and hence, it requires a comparative smaller pressure gradient to optimize the dispersion tensor, which is of the same magnitude of the other micro structures.

In the subsequent chapters I focused on finding optimal microstructure that will minimize the energy loss and maximize mixing. Figure (5.3) and (5.4) exhibits the dependence of pressure gradient on the objective function (minimize the energy loss and maximize mixing). When the results obtained using shape optimization for minimizing dissipation power and maximizing “dispersion power” where the pressure gradient is

a design variable, were compared with microstructure formed by square array of same porosity it showed significant improvement in reducing energy loss while fluid flow and increasing mixing as shown in Figure (5.11).

Similarly, when optimized microstructures obtained from topology optimization were compared with the square array of same porosity shows the same trend. When the macroscopic flow is compared for optimized microstructure and square array formed by circular solid region with same porosity, a higher magnitude of velocity is obtained for the optimized microstructure as shown in Figure (6.6 a).

The work done in the following chapter to find the optimized layout of the microstructure that will maximize mixing gave a mixed idea of how the optimized layout should look. In Figure (7.5) the microstructure layout is such that the flow is deviated toward the vertical direction. In all the results Figure (7.5) – (7.6) the inflow in at negative 45 degree to the horizontal and the aim here was to distribute the solute in the horizontal direction. In Figure (7.5) the microstructure diverts the flow as much as possible to the horizontal direction. For a lower volume fraction the solid materials form a wall around the boundary of zone 1 and zone 2 to restrict the flow in vertical direction. For a higher velocity in horizontal direction the longitudinal dispersion tensor will be higher and hence maximize the solute flow in that direction.

All the above mentioned work was done for single phase fluid flow. But in most of the application of porous media the fluid is not of single phase. In the last two chapters we developed theory that governs the multiphase fluid flow in a porous media and then solve those partial differential equations to design porous media. The governing equation developed using mixture model gives the approximate behavior of the multiphase fluid flow in a porous media. These governing equations were solved using finite difference method. After optimization microstructure with elliptic microstructure shows the least energy loss. From Figure (8.8) it can also be added that for microstructure with elliptic solid region the velocity profile shows less variance as compared with other two microstructures. When the macroscopic flow is compared for optimized microstructure obtained from shape optimization with square array formed by circular solid region with same porosity, a higher magnitude of velocity is obtained for the optimized microstructure as shown in figure (8.8). The methodology developed here can also be used to understand the effect of multiphase flow with variable volume fraction. This also gives an opportunity to study further in the field of multiphase flow to develop time depended expression for effective properties.

Further future work should be directed towards solving more problems of similar nature. In addition to the solved optimization problem, such methodology can be further extended to modeling complex materials such as poroelastic material for artificial bones or teeth. Also experiments with

prototype optimized material should be pursued to validate the results obtained from this work. From simulation perspective, further algorithms and techniques should be developed to solve for transient cases since for multiphase fluid the transient example will be more realistic as compared to the results shown in this work. Volume of fluid method should be further investigated using theory of homogenization to derive governing equations for different scales that will identify each phase separately at each time step. Finally for better understanding of the results further work should also be done in solving the same examples in three dimensional domain.

APPENDIX A

APPENDIX A

Appendix A shows the Matlab program used to solve the shape optimization problem to maximize isotropic permeability in Chapter 4.

```
function main
clear all
clc
This part of the code defines the number of variables, constraints and other parameters associated with it.
fname1 = ['G&P'];
fpt1 = fopen( fname1, 'wt');
volfrac = 0.3;
mcons = 3;%number of constraints
numdesvar = 4;%number of variables
xmin = [0.01,0.01, 0.01, 0.01]';%lower area limit on area
xmax = [1, 1, 1, 1]';%upper area limit on area
ITERMAX = 100;%maximum number of iteration
STEPSIZE = 0.1;%stepsize
A = 2;
R = 9.44E-4;
T = pi/2;
xval = [1,0.5,0.5,1]';%initial value of area
iter=1;
converged = 0;
s0=0.1;
xold2 = xval;
xold1 = xval;
low = xmin - s0 *(xmax - xmin);
upp = xmax + s0 *(xmax - xmin);
df0dx2 =zeros(numdesvar,1);
dfdx2=zeros(mcons,numdesvar);
a0mma = 1;
cmma = 1000*ones(mcons,1);
dmma = 0*ones(mcons,1);
amma = 0*ones(mcons,1);
obj3 = 0;
obj2 = 0;
obj1 = 0;
while iter < ITERMAX & converged == 0
alpha=zeros(numdesvar,1);
beta=zeros(numdesvar,1);
```



```

fname3 = ['K22-',int2str(iter)];
postplot(fem, ...
    'tridata',{'K22','cont','internal'}, ...
    'trimap','jet(1024)', ...
    'refine',3);
saveas(gcf, fname3,'jpg')
set(gcf,'outerposition',[10,10,400,400]);
fname4 = ['K12-',int2str(iter)];
postplot(fem, ...
    'tridata',{'K12','cont','internal'}, ...
    'trimap','jet(1024)', ...
    'refine',3);
saveas(gcf, fname4,'jpg')
set(gcf,'outerposition',[410,10,400,400]);
fname5 = ['K21-',int2str(iter)];
postplot(fem, ...
    'tridata',{'K21','cont','internal'}, ...
    'trimap','jet(1024)', ...
    'refine',3);
saveas(gcf, fname5,'jpg')
end
if converged1 <= 0.0001 & converged2 <= 0.0001 & converged3...
    <= 0.0001 & fval <= 0
    converged = 0;
else
    converged = 0;
end
iter = iter + 1;
xold2 = xold1;
xold1 = xval;
xval = xmma ;
obj3 = obj2;
obj2 = obj1;
obj1 = obj;
end
fclose(fpt1);
clear all
%%
%%
%%
Function to compute the constraints and its sensitivity with respect to the design variables
function [con, dcon] = constraint(AR, major_axis,...
    minor_axis, theta, volfrac,A,R,T )
B = 0.002;
con1 = 1-(pi*major_axis*minor_axis)/((volfrac)*AR*B^2);

```



```

%defining the partial differential equations
clear appl
appl.mode.class = 'FIPDEC';
appl.dim = {'K11','K12','K21','K22','A1','A2','K11_t','K12_t',...
    'K21_t','K22_t','A1_t','A2_t'};
appl.gporder = 4;
appl.cporder = 2;
appl.assignsuffix = '_c';
clear pnt
pnt.constr = {0,{0;0;0;0;'A1';'A2'}};
pnt.ind = [1,2,1,1,1,1,1,1];
appl.pnt = pnt;
clear bnd
bnd.type = {'neu','dir'};
bnd.h = {1,{1;0;0;0;0;1;0;0;0;0;1;0;0;0; ...
    0;1;0;0;0;0;0;0;0;0}};
bnd.ind = [1,1,1,1,2,2,2,2];
appl.bnd = bnd;
clear equ
equ.be = {{{0;0},{0;0},{0;0},{0;0},{0;0},{0;0}; ...
    {0;0},{0;0},{0;0},{0;0},{0;0},{0;0};{0;0},{0; ...
    0},{0;0},{0;0},{-1.0;0},{0;0},{0;0},{0;0},{0; ...
    0},{0;0},{0;0},{-1.0;0};{0;0},{0;0},{0;0},{0; ...
    0},{0;-1.0},{0;0};{0;0},{0;0},{0;0},{0;0},{0; ...
    0},{0;-1.0}}};
equ.c = {{0,0,0,0,0,0;0,0,0,0,0,0;'-eta',0,0, ...
    0,0,0;0,'-eta',0,0,0,0;0,0,'-eta',0,0,0,0, ...
    0,'-eta',0,0}};
equ.al = {{{1;0},{0;0},{0;1},{0;0},{0;0},{0;0}; ...
    {0;0},{1;0},{0;0},{0;1},{0;0},{0;0};{0;0},{0; ...
    0},{0;0},{0;0},{0;0},{0;0};{0;0},{0;0},{0;0}, ...
    {0;0},{0;0},{0;0};{0;0},{0;0},{0;0},{0;0},{0; ...
    0},{0;0};{0;0},{0;0},{0;0},{0;0},{0;0},{0;0}}};
equ.f = {{0;0;-1.0;0;0;-1.0}};
equ.ind = [1];
appl.equ = equ;
fem.appl{1} = appl;
% Shape functions
fem.shape = {'shlag(2,"K11")','shlag(2,"K12")',...
    'shlag(2,"K21")','shlag(2,"K22")',...
    'shlag(2,"A1")','shlag(2,"A2")'};
fem.border = 1;
fem.units = 'SI';
% Subdomain settings
clear equ

```

```

equ.be = {{{{0;0},{0;0},{0;0},{0;0},{-1.0;0},{0;0}; ...
          {0;0},{0;0},{0;0},{0;0},{0;0},{-1.0;0};{0;0}, ...
          {0;0},{0;0},{0;0},{0;-1.0},{0;0};{0;0},{0;0}, ...
          {0;0},{0;0},{0;0},{0;-1.0};{0;0},{0;0},{0;0}, ...
          {0;0},{0;0},{0;0};{0;0},{0;0},{0;0},{0;0},{0; ...
          0},{0;0}}}}};
equ.c = {'-eta';'-eta';'-eta';'-eta';0;0};
equ.da = 1;
equ.al = {{{{0;0},{0;0},{0;0},{0;0},{0;0},{0;0}; ...
          {0;0},{0;0},{0;0},{0;0},{0;0},{0;0};{0;0},{0; ...
          0},{0;0},{0;0},{0;0},{0;0};{0;0},{0;0},{0;0}, ...
          {0;0},{0;0},{0;0};{-1.0;0},{0;0},{0;-1.0},{0; ...
          0},{0;0},{0;0};{0;0},{-1.0;0},{0;0},{0;-1.0}, ...
          {0;0},{0;0}}}}};
equ.f = {{-1.0;0;0;-1.0;0;0}};
equ.ind = [1];
equ.dim = {'K11','K12','K21','K22','A1','A2'};
equ.var = {'absK11x_c','sqrt(K11x^2+K11y^2)', ...
          'absK12x_c','sqrt(K12x^2+K12y^2)', ...
          'absK12x_c','sqrt(K12x^2+K12y^2)', ...
          'absK21x_c','sqrt(K21x^2+K21y^2)', ...
          'absK22x_c','sqrt(K22x^2+K22y^2)', ...
          'absK22x_c','sqrt(K22x^2+K22y^2)', ...
          'absK22x_c','sqrt(K22x^2+K22y^2)', ...
          'absA1x_c','sqrt(A1x^2+A1y^2)', ...
          'absA2x_c','sqrt(A2x^2+A2y^2)', ...
          'absA2x_c','sqrt(A2x^2+A2y^2)', ...
          'absA2x_c','sqrt(A2x^2+A2y^2)', ...
          'absA2x_c','sqrt(A2x^2+A2y^2)'};
equ.expr = {'U','-(K11*P1+K12*P2)', ...
          'V','-(K21*P1+K22*P2)'};
fem.equ = equ;
% Global expressions
fem.expr = {'P1',0, ...
          'P2','0', ...
          'eta','0.001'};
% Coupling variable elements
clear elemcpl
% Extrusion coupling variables
clear elem
elem.elem = 'elcplextr';
elem.g = {'1'};
src = cell(1,1);
clear bnd
bnd.expr = {{{{},{},'K11'},{{{},{},'A2'},{'K22',{},{},'A2'},...

```



```

    {'2','2','2','2','2','2','2','2','2','2','2','2','2'});
bnd.ind = {'2','4'};
elem.geomdim = {'',bnd,{''}};
elemcpl{2} = elem;
fem.elemcpl = elemcpl;
% Solution form
fem.solform = 'general';
% Multiphysics
fem=multiphysics(fem, ...
    'sd',[1]);
% Extend mesh
fem.xmesh=meshextend(fem);
% Solve problem
fem.sol=femlin(fem, ...
    'conjugate','on', ...
    'solcomp',{'K21','K11','K22','A1','K12','A2'}, ...
    'outcomp',{'K21','K11','K22','A1','K12','A2'});
% Save current fem structure for restart purposes
fem0=fem;
% Integrate
K11a = 0.001*postint(fem,'K11','dl',[1])/(L*B);
K12a = 0.001*postint(fem,'K12','dl',[1])/(L*B);
K21a = 0.001*postint(fem,'K21','dl',[1])/(L*B);
K22a = 0.001*postint(fem,'K22','dl',[1])/(L*B);
Kavg = [K11a K12a; K21a K22a];
k= (K11a+K22a)/2;
error=((K11a-K22a)^2+((K12a+K21a)/2)^2)/k^2;
OBJ=-k+error;

```

APPENDIX B

APPENDIX B

Appendix b shows the Matlab program used to solve the topology optimization problem to minimize dissipation power in Chapter 5.

```
flclear fem
clc
clear all
warning off
flclear fem
fname1 = ['minimisedissipation'];
fpt1 = fopen( fname1, 'wt');
Da = 1e-3;
Define the Geometry
g1=rect2(1,1,'base','corner','pos',[0,0])+rect2(1.2,1.2,'base',...
    'corner','pos',[-0.1,-0.1]);
s.objs={g1};
s.name={'R1'};
s.tags={'g1'};
fem.draw=struct('s',s);
fem.geom=geomcsg(fem);
Define Mesh
fem.mesh = meshinit(fem,'Hmaxsub',[1, 0.02, 2, 0.02]);
meshplot(fem.mesh)
fem.const.alphamin = 0.001;
fem.const.alphamax = 1/Da;
fem.const.q = 0.01;
fem.const.eta = 0.01;
Phi0 = 1;
Define the variables and the governing equations
fem.sdim = {'x' 'y'};
fem.dim = {'u' 'v' 'p' 'rho'};
fem.shape = [2 2 1 1];
fem.bnd.shape = {[1:3]};
fem.bnd.type = 'neu';
fem.bnd.g = {0,{0.001;0.001;0;0}};
fem.bnd.ind = [2,2,1,1,1,1,1,1];
fem.equ.shape = {[1:3] [1:4]};
fem.equ.init = {{0;0;0;0.7}};
```

```

fem.equ.f = {'alpha*u-1';'alpha*v+1';'ux+vy';1},{'alpha*u-1';...
'alpha*v+1';'ux+vy'; 1}};
fem.equ.ga = {'-p+2*eta*ux';'eta*(uy+vx)'};{'eta*(uy+vx)';...
'-p+2*eta*vy'}; {0;0};{0;0}};
fem.equ.ind = [1,2];
% Coupling variable elements
clear elemcpl
Enforcing periodic boundary condition
clear elem
elem.elem = 'elcplextr';
elem.g = {'1'};
src = cell(1,1);
clear bnd
bnd.expr = {'v',{}};{'u',{}};{'u',{}};{'v',{}};
bnd.map = {'0','0','0','0'};
bnd.ind = {'1','2','3','4','5','6','7','8'};
src{1} = {'',bnd,{'}};
elem.src = src;
geomdim = cell(1,1);
clear bnd
bnd.map = {'1',{}};{'1',{}};{'',{}};{'2',{}};{'',{}};{'2'};
bnd.ind = {'1','2','4','5','6','7','3','8'};
geomdim{1} = {'',bnd,{'}};
elem.geomdim = geomdim;
elem.var = {'pconstr4','pconstr3','pconstr1','pconstr2'};
map = cell(1,2);
clear submap
submap.type = 'linear';
submap.sg = '1';
submap.sv = {'2','8'};
submap.dg = '1';
submap.dv = {'1','7'};
map{1} = submap;
clear submap
submap.type = 'linear';
submap.sg = '1';
submap.sv = {'7','8'};
submap.dg = '1';
submap.dv = {'1','2'};
map{2} = submap;
elem.map = map;
elemcpl{1} = elem;
Point constraint variables (used for periodic conditions)
clear elem
elem.elem = 'elpconstr';

```

```

elem.g = {'1'};
clear bnd
bnd.constr = {'pconstr4-(v)', 'pconstr3-(u)', '0', '0'}, {'0', '0', 'pconstr1-(u)', ...
    'pconstr2-(v)'};
bnd.cpoints = {'2', '2', '2', '2'}, {'2', '2', '2', '2'};
bnd.ind = {'3'}, {'8'};
elem.geomdim = {{{}, bnd, {}}};
elemcpl{2} = elem;
fem.elemcpl = elemcpl;
Define the objective function
fem.equ.expr = {'A' 'eta*(2*ux*ux+2*vy*vy+(uy+vx)*(uy+vx))'...
    'alpha', {0, 'alphamin+(alphamax-alphamin)*q*(1-
    rho)/(q+rho)'}, };
fem.bnd.expr = {'B' '0'};
fem=multiphysics(fem);
Define the adjoint problem
fem = femdiff(fem);
fem.xmesh = meshextend(fem);
fem.sol = assemnit(fem);
femadj = fem;
femadj.equ.ga = {{{ 'diff(A,ux)' 'diff(A,uy)' } 'diff(A,vx)' 'diff(A,vy)' } ...
    { 'diff(A,px)' 'diff(A,py)' } { 'diff(A,rhox)' 'diff(A,rhoy)' } };
femadj.equ.f = { 'diff(A,u)' 'diff(A,v)' 'diff(A,p)' 'diff(A,rho)' };
femadj.bnd.g = { 'diff(B,u)' 'diff(B,v)' 'diff(B,p)' 'diff(B,rho)' };
femadj.xmesh = meshextend(femadj);
flngdof(fem);
i4 = find(assemnit(fem, 'Init', { 'rho' 1 }, 'Out', 'U'));
L = assemble(fem, 'Out', { 'L' });
Vgamma = L(i4);
Vdomain = sum(Vgamma);
i123 = find(assemnit(fem, 'Init', { 'u' 1 'v' 1 'p' 1 }, 'Out', 'U'));
a0 = 1;
a = 0;
c = 20;
d = 0;
xmin = 0.01;
xmax = 1;
xold = fem.sol.u(i4);
xolder = xold;
low = 0;
upp = 1;
penal = 3;
for iter = 1:1000
fem.sol = femnlin(fem, 'Solcomp', { 'u' 'v' 'p' }, 'U', fem.sol.u);
[K N] = assemble(fem, 'Out', { 'K' 'N' }, 'U', fem.sol.u);

```

```

[L M] = assemble(femadj,'Out',{'L' 'M'},'U',fem.sol.u);
femadj.sol = femlin('In',{'K' K(i123,i123)' 'L' L(i123)' 'M'...
    zeros(size(M)) 'N' N(:,i123)});
rho = fem.sol.u(i4);
Phi = postint(fem,'A','Edim',2) + postint(fem,'B','Edim',1);
dPhidgamma = K(i123,i4)*femadj.sol.u-L(i4);
x = rho;
f = Phi/Phi0;
g = rho*Vgamma/Vdomain-0.5;
dfdx = dPhidgamma/Phi0; dgdx = Vgamma/Vdomain;
d2fdx2 = zeros(size(rho)); d2gdx2 = zeros(size(rho));
nel = size(x); nely = nel(1); nelx = nel(2); rmin = 0.1;
[dfdx] = check(nelx,nely,rmin,x,dfdx);
[xnew,y,z,lambda,ksi,eta,mu,zeta,s,low,upp] = mmasub(1,length(rho),iter,
...
x,xmin,xmax,xold,xolder,f,dfdx,d2fdx2,g,dgdx,d2gdx2,low,upp,a0,a,c,d);
xolder = xold; xold = x;
rho = xnew;
if iter >= 100
break
end
u0 = fem.sol.u; u0(i4) = rho;
fem.sol = femsol(u0);
disp(sprintf('Iter.:%3d Obj.: %8.4f Vol.: %6.3f Change: %6.3f', ...
iter,f,rho*Vgamma,max(abs(xnew-xold))))
fprintf(fpt1, '%f %f \n',iter,f);
set(gcf,'outerposition',[10,400,400,400]);
fname5 = ['topo-',int2str(iter)];
postplot(fem,'tridata','rho','trimap','gray')
axis equal; shg; pause(0.1)
saveas(gcf, fname5,'jpg')
end

```

APPENDIX C

APPENDIX C

In the topology optimization work shown in Chapter 6 and 7 the derivative of objective function with respect to the design variable is obtained using the adjoint problem as described by Olesen et al. According to their work the derivative of the objective function can be expressed using the chain rule,

$$\frac{d}{d\rho} [\text{Obj}] = \frac{\partial \text{Obj}}{\partial \rho} + \int_{\Omega_m} \frac{\partial \text{Obj}}{\partial \mathbf{u}} \cdot \frac{\partial \mathbf{u}}{\partial \rho} d\Omega \quad (\text{AC.1})$$

where Obj is the objective function, ρ is the design variable and \mathbf{u} is the velocity-pressure vector. The starting point of the finite element analysis is to approximate the solution component u_i on a set of finite element basis functions or also known as shape function $\{\varphi_{i,n}\}$

$$u_i = \sum_n u_{i,n} \varphi_{i,n} \quad (\text{AC.2})$$

where $u_{i,n}$ are the expansion coefficients. Similarly, the design variable field ρ is expressed as

$$\rho = \sum_n \rho_n \varphi_{4,n} \quad (\text{AC.3})$$

For a homogenized incompressible Stokes problem the standard Taylor-Hood element pair with quadratic velocity and pressure approximation is

commonly used. For the design variable linear Lagrange elements are chosen.

The governing equations and the boundary conditions are discretized by the Galerkin method as

$$L_i(U, \rho) - \sum_{j=1}^3 N_{ji}^T \Lambda_j = 0 \quad (\text{AC.4})$$

$$M_i(U, \rho) = 0 \quad (\text{AC.5})$$

where U_i , Λ_i and ρ are column vectors with the expansion coefficients for the solution $u_{i,n}$, the Lagrange multipliers $\mu_{i,n}$, and the design variable field ρ_n , respectively. The column vector L_i contains the projection of Neumann boundary conditions onto $\phi_{i,n}$. The partial integration is given by

$$L_{i,n} = \int_{\Omega_m} \left(\phi_{i,n} F_i + \nabla \phi_{i,n} \cdot \Gamma_i \right) d\Omega + \int_{\partial\Omega_m} \phi_{i,n} G_i d\partial\Omega_m \quad (\text{AC.6})$$

The column vector M_i enforces the Dirichlet constraint in the boundary conditions

$$M_{i,n} = R_i \quad (\text{AC.7})$$

The matrix $N_{ij} = -\partial M_i / \partial U_j$ describes the coupling to the Lagrange multipliers in Neumann boundary condition. The sensitivity analysis as shown in equation (AC.1) can be also written as

$$\frac{d}{d\rho} [\text{Obj}] = \frac{\partial \text{Obj}}{\partial \rho} + \sum_{i=1}^3 \frac{\partial \text{Obj}}{\partial U_i} \cdot \frac{\partial U_i}{\partial \rho} \quad (\text{AC.8})$$

Equation (AC.8) is computed using the standard adjoint method. From

equation (AC.4-AC.5) we have for any ρ that $L_i - \sum_{j=1}^3 N_{ij}^T \Lambda_j = 0$ and

$M_i(U, \rho) = 0$. Therefore also the derivative of those quantities with

respect to ρ is zero. Adding any multiple such as \tilde{U}_i and $\tilde{\Lambda}_i$ to equation

(AC.8) does not change the result. Equation (AC.8) can be written as

$$\begin{aligned} \frac{d}{d\rho} [\text{Obj}] = & \frac{\partial \text{Obj}}{\partial \rho} + \sum_{i=1}^3 \frac{\partial \text{Obj}}{\partial U_i} \cdot \frac{\partial U_i}{\partial \rho} + \\ & \sum_{i=1}^3 \left[\tilde{U}_i \frac{\partial}{\partial \rho} \left(L_i - \sum_{j=1}^3 N_{ij}^T \Lambda_j \right) - \tilde{\Lambda}_i^T \frac{\partial}{\partial \rho} M_i \right] \end{aligned} \quad (\text{AC.9})$$

Reorganizing the terms,

$$\begin{aligned} \frac{d}{d\rho} [\text{Obj}] = & \frac{\partial \text{Obj}}{\partial \rho} + \sum_{i=1}^3 \left(\tilde{U}_i^T \frac{\partial L_i}{\partial \rho} - \tilde{\Lambda}_i^T \frac{\partial M_i}{\partial \rho} \right) + \\ & \sum_{i=1}^3 \left[\frac{\partial \text{Obj}}{\partial U_i} + \sum_{j=1}^3 \left(\tilde{U}_i^T \frac{\partial L_i}{\partial U_i} - \tilde{\Lambda}_i^T N_{ij} \right) \right] \frac{\partial \tilde{U}_i}{\partial \rho} - \\ & \sum_{i=1}^3 \left[\sum_{j=1}^3 \tilde{U}_i^T N_{ij}^T \right] \frac{\partial \tilde{\Lambda}_j^T}{\partial \rho} \end{aligned} \quad (\text{AC.10})$$

The derivatives $\partial U_i / \partial \rho$ and $\partial \tilde{\Lambda}_i / \partial \rho$ of the implicit functions can be

eliminated by choosing \tilde{U}_i and $\tilde{\Lambda}_i$ such that

$$\sum_{j=1}^3 \left(\mathbf{K}_{ji}^T \tilde{\mathbf{U}}_j - \mathbf{N}_{ji}^T \tilde{\Lambda}_j \right) = \frac{\partial \text{Obj}}{\partial \mathbf{U}_i} \quad (\text{AC.11})$$

$$\sum_{j=1}^3 \mathbf{N}_{ij} \tilde{\mathbf{U}}_j = 0 \quad (\text{AC.12})$$

where $\mathbf{K}_{ij} = -\partial \mathbf{L}_i / \partial \mathbf{U}_j$. This problem is the adjoint of equation (AC.4) and

$\tilde{\mathbf{U}}_i$ and $\tilde{\Lambda}_i$ are the corresponding Lagrange multipliers.

REFERENCES

REFERENCES

Allaire, G (2002). Shape Optimization by the Homogenization Method, New York: Springer-Verlag.

Allen, M. III (1985). Numerical Modeling of Multiphase Flow in Porous Media. Advances in Water Resources: 8, 162-187.

Amaziane, B, Bourgeat, A. and Jurak, M. (2005). Effective Macro diffusion in Solute Transport through Heterogeneous Porous Media. Society for Industrial and Applied Mathematics- Multiscale Modeling & Simulation: 5, 1, 184-204.

Auriault, J.-L. (1980). Dynamic Behavior of a Porous Medium Saturated by a Newtonian Fluid. International Journal of Engineering Science: 18, 775-785.

Auriault, J.-L. and Lewandowska, J. (1993). Homogenization analysis of Diffusion and Adsorption Macrotransport in Porous Media: Macrotransport in absence of advection. Geotechnique: 43, 457-469.

Auriault, J.-L. and Lewandowska, J. (1997 May). Effective Diffusion Coefficient: From Homogenization to Experiment. Transport in Porous Media: 27, 205-223.

Auriault, J.-L. (2002, August). Up scaling Heterogeneous Media by Asymptotic Expansions. Journal of Engineering Mechanics: 128, 817-822.

Auriault, J.-L, Geindreau, C. and Boutin, C. (2005 July). Filtration Law in Porous Media with Poor Separation of Scales. Transport in Porous Media: 60, 1, 89-108.

Ballean, D, Levy, T. and Balint, S. (2003 April). Diffusion–Convection in a Porous Medium with Impervious Inclusions at Low Flow Rates. Transport in Porous Media: 51, 19-39.

Bandyopadhyay, D, Benard, A and Diaz, A (2008). Design of Porous materials using topology optimization. Submitted to AIAA

Bandyopadhyay, D and Benard, A (2008). Optimization of effective properties and solute transfer in porous media using shape optimization. In preparation.

Bandyopadhyay, D and Benard, A (2007) Optimization of solute transfer in porous media using homogenization. Proceeding of the Inverse Problems, Design and Optimization Symposium: p 1-8

Bang, B. and Dag Lukkassen, N. (1999). Application of Homogenization theory related to Stokes flow in porous media. Applications of Mathematics: 4, 309-319.

Bendsøe, M. and Kickuchi, N. (1998). Generating optimal Topologies in structural Design using a homogenization Method. Computer Methods in Applied Mechanics and Engineering: 71, 197-224.

Bendsøe, M.P. and Sigmund, O. (2003). Topology Optimization-Theory, Methods and Applications. Berlin: Springer.

Bensoussan, A. (1978). Asymptotic Analysis for Periodic Structures, New York: North-Holland Pub. Co.

Beran MJ (1968). Statistical Continuum Theories, New York: Interscience Publishers

Bird, R. B, Stewart, W. E, and Lightfoot E. N (2001). Transport Phenomena, Wiley.

Blackwell, R. J, Rayne, J. R. and Terry, W. M. (1959). Factors influencing the efficiency of miscible displacement. Transactions AIME: 216, 1-8.

Borrvall, T. and Petersson, J. (2003 January). Topology optimization of fluids in stokes flow, International Journal for Numerical Methods in Fluids: 41, 77-107.

Buyuktas, D. and Wallender, W. W. (2003 October). Dispersion in spatially periodic porous media. Heat and Mass Transfer: 40, 261-270.

Chella, R, Lasseux, D and Quintard, M (1998). Multiphase, Multicomponent Fluid Flow in Homogeneous and Heterogeneous Porous Media. Oil & Gas Science and Technology - Revue De L'Institut Francais Du Petrole: 53, 3, 335-346.

COMSOL version 3.2 and 3.3 Reference Manual. Comsol Inc.

Delgado, J. M. P. Q. (2005 September). A critical review of dispersion in packed beds. Heat Mass Transfer: 42, 279–310.

Diaz, A. R. and Sigmund, O. (1995 August). Checkerboard patterns in layout optimization. Structural and Multidisciplinary Optimization: 10, 1, 40-45.

Diaz, A. R. and Bénard, A. (2001 July). On the discretization of problems involving periodic planar tilings. Communications in Numerical Methods in Engineering: 17, 543–549

Diaz, A. R. and Bénard, A. (2003 March). Designing materials with prescribed elastic properties using polygonal cells. International Journal for Numerical Methods in Engineering: 57, 301–314.

Diaz, A. R. and Bénard, A. (2003 September). Topology Optimization of Heat-Resistant Structures. Proceedings of DETC'03 ASME 2003 Design Engineering Technical Conferences: Chicago, IL.

Edwards, M. F. and Richardson, J. F. (1968). Gas dispersion in packed beds. Chemical Engineering Science: 23(2), 109-123.

Edwards, D. A, Shapiro, M, Brenner, H. and Shapira, M. (1991). Dispersion of Inert Solutes in Spatially Periodic, Two-Dimensional Model Porous Media. Transport in Porous Media: 6, 337-358.

Eschenauer, H. A. and Olhoff, N. (2001). Topology optimization of continuum structures: a review. Applied Mechanics Reviews: 54, 4, 331–389.

Eshelby, J.D. (1961) Elastic inclusions and inhomogeneities. Progress in Solid Mechanics, vol. II. North-Holland, Amsterdam, pp. 87–140.

Evgrafov, A. (2004). Approximation of topology optimization problems using sizing optimization problems. PhD Dissertation. Göteborg University, Sweden.

Evgrafov, A (2005 July). Topology optimization of slightly compressible fluids. Journal of Applied Mathematics and Mechanics: 86, 1, 46 – 62.

Evgrafov, A (2005 October). The Limits of Porous Materials in the Topology Optimization of Stokes Flows. Journal Applied Mathematics and Optimization: 52, 3, 263-277

Fluent version 6.2. Reference Manual. Ansys Inc.

Gersborg-Hansen, A. (2003). Topology optimization of incompressible Newtonian flows at moderate Reynolds Numbers. MS Thesis, Technical University of Denmark.

Gersborg-Hansen, A, Sigmund, O. and Haber, R. B. (2005 September). Topology optimization of channel flow problems, Structural and Multidisciplinary Optimization: 30 181–192.

Gersborg-Hansen, A, Bendsøe, M. P. and Sigmund, O. (2006 March) Topology optimization of heat conduction problems using the finite volume method. Structural and Multidisciplinary Optimization: 30 181–192.

Guest, J. K. (2005). Design of Optimal Porous Material Structures for Maximized Stiffness and Permeability using Topology Optimization and Finite Element Methods. PhD Dissertation. Princeton University.

Guest, J. K. and Prevost, J. H. (2005 December) Topology optimization of creeping fluid flows using a Darcy–Stokes finite element. International Journal for Numerical Methods in Engineering: 66, 461-484.

Guest, J. K. and Prevost, J. H. (2006 March) Optimizing multifunctional materials: design of microstructures for maximized stiffness and fluid permeability. International Journal of Solids and Structures: 43, 22-23, 7028-7047.

Guest, J. K., Prévost, J. H. (2007 January). Design of maximum permeability material structures. Computer methods in applied mechanics and engineering: 196, 1006-1017.

Gunn, D. J. and Pryce, C. (1969). Dispersion in packed beds. Trans. Inst. Chem. Eng: 47, T341-T350.

Ishii, M. and Hibiki, T. (2006) Thermo-Fluid Dynamics of Two-Phase Flow. New York: Springer

Jensen, J. S. (2003). Phononic band gaps and vibrations in one- and two-dimensional mass-spring structures. Journal of Sound and Vibration: 266, 5, 1053 –1078.

Jensen, J. S. and Sigmund, O. (2004). Systematic design of photonic crystal structures using topology optimization: low-loss waveguide bends. Applied Physics Letters: 84, 12, 2022–2024.

Jörgens, A. (2003) Topology Optimization of heat resistant composite structures, PhD Dissertation Institut für Kunststoffverarbeitung.

Kaviany, A. (1991). Principle of Heat Transfer in Porous Media, New York, Springer – Verlag.

Kitandis, K, and Dykaar, B. B. (1997 January). Stokes flow in a slowly varying two dimensional pore. Transport in Porous Media: 26, 89, 89-98.

Klarbring, A, Petersson, J, Torstenfelt, B. and Karlsson, M. (2003 August). Topology optimization of flow networks. Computer Methods in Applied Mechanics and Engineering: 192, 35, 3909-3932.

Kleinstreuer, C. (2003). Two-Phase Flow: Theory and Applications. New York: Taylor and Francis.

Kroner, E. (1978) Self-consistent scheme and graded disorder in polycrystal elasticity. Physics of Fluid: 8, 2261–2267.

Kröner, E. (1986) Statistical Modelling. Netherlands: Elsevier.

Kurochkina, E. P, Soboleva, O. N and Epov, M. I (2004). Numerical modeling of two- phase liquid flow in fractural porous medium. Journal of Mixing Science: 40, 5 474-481

Larsen, U. D, Sigmund, O. and Bouwstra, S. (1996). Design and fabrication of compliant mechanisms and material structures with negative Poisson's ratio. IEEE, International Workshop on Micro Electro Mechanical Systems, MEMS-96.

Lee, C. K, Sun, C-C. and Mei, C. C. (1996 March). Computation of permeability and dispersivities of solute or heat in periodic porous media. International Journal of Heat and Mass Transfer: 39,4, 661-676.

Lomen, D.O, Islas, A. L, Fan, X. and Warrick A.W. (1991 October). A perturbation solution for nonlinear solute transport in porous media. Transport in Porous Media: 5, 5-6

Man, W, Donev, A, Stillinger, F. H, Sullivan, M. T, Russel, W. B, Heeger, D, Inati, S, Torquato, S and Chaikin, P. M (2005). Experiments

on Random Packings of Ellipsoids. Physical Review Letter: 94, 198001, 1-4

Martys, N. S, Torquato, S and Bentz, D. P (1994). Universal scaling of fluid permeability for sphere packings. Physical Review E: 50, 1, 403 - 408

Mei, C. C. and Auriault, J.-L. (1989 December). Mechanics of heterogeneous porous media with several spatial scales. Proceedings of the Royal Society of London, Series A, Mathematical and Physical Sciences: 426(1871), 391-423.

Mei, C. C. and Auriault, J. L. (1991). The effect of Weak inertia of flow through a porous medium. Journal of Fluid Mechanics: 222, 647-663.

Mei, C. C. (1991). Heat Dispersion in Periodic Porous Media by Homogenization Method. Multiphase Transport in Porous Media: 122, 11-16.

Mei, C. C. (1992). Method of Homogenization Applied to Dispersion in Porous Media. Transport in Porous Media: 9, 261-274.

Mei, C. C. (1995). Mathematical Analysis in Engineering. New York: Cambridge University Press.

Olesen, L. H, Okkels, F. and Bruus, H. (2005 September). A high-level programming-language Implementation of topology optimization applied to steady-state Navier–Stokes flow. International Journal for Numerical Methods in Engineering: 65, 975-1001.

Pan, Y. and Horne, R. N. (2001 October). Generalized Macroscopic Models for Fluid Flow in Deformable Porous Media I: Theories. Transport in Porous Media: 45, 1, 1-27.

Pan, Y. and Horne, R. N. (2001 November). Generalized Macroscopic Models for Fluid Flow in Deformable Porous Media II: Numerical Results and applications. Transport in Porous Media: 45, 2, 195-213.

Pfannkuch, H. O. (1963). Contribution à l'étude des déplacements de fluides miscibles dans un milieu poreux." Rev. I Fr. Petrol: XVIII(2), 170–215.

Pharm, D. C and Torquato, S. (2004 December). Exactly realizable bounds on the trapping constant and permeability of porous media. Journal of Applied Physics: 97, 013535, 1-8

Quintard, M and Whitaker, S (1988). Two-phase flow in heterogeneous porous media: The method of large-scale averaging. Transport in Porous Media: 3, 357-413

Quintard, M and Whitaker, S (1990). Two-phase flow in heterogeneous porous media I: The influence of large spatial and temporal gradients. Transport in Porous Media: 5, 341-379

Rifai, M. N. E, Kaufman, W. J., and Todd, D. N. (1956). Dispersion Phenomena in Laminar Flow through Porous Media. University of California, Berkeley, Berkeley, California.

Rubinstein, J. and Torquato, S. (1988). Diffusion-controlled reaction: Mathematical formulation, variational principles and rigorous bounds. Journal of Chemical Physics: 88, 10, 6372-6380.

Rubinstein, J. and Torquato, S. (1989). Flow in Random Porous Media: Mathematical Formulation, Variational Principles, and Rigorous Bounds. Journal of Fluid Mechanics: 206, 25-46.

Sáez, A. E, Otero, C . J and Rusinek, I. (1989). The effective Homogeneous Behaviour of Heterogeneous Porous Media. Transport in Porous Media: 4, 213-238

Sanchez-Palencia, E. (1980) Non-Homogeneous Media and Vibration Theory. Berlin: Springer. 1980.

Sigmund, O. (1995 June). Tailoring materials with prescribed elastic properties. Mechanics of Materials: 20, 351-368.

Sigmund, O. and Torquato, S. (1996). Composites with extremal thermal expansion coefficients. Applied Physics Letters: 69, 21, 3203-3205.

Sigmund, O. (2000). A new class of extremal composites. Journal of the Mechanics and Physics of Solids: 48, 397-428.

Sigmund, O. (2001). A 99 line topology optimization code written in Matlab. Structural and Multidisciplinary Optimization: 21 120–127.

Svanberg, K. (1987). The method of Moving Asymptotes-A new method for structural optimization. International Journal for Numerical Methods in Engineering: 24, 359-373.

Svanberg, K. (2002 January). A Class Of Globally Convergent Optimization Methods Based On Conservative Convex Separable Approximations. Journal on Optimization: 12, 2, 555–573.

Torquato, S and Pham, D. C. (2004). Optimal Bounds on the Trapping Constant and Permeability of Porous Media. Physical Review Letter: 92, 255505, 1-4

Wang, Y. (2003). A study on Microstructures of Homogenization for Topology Optimization. PhD Dissertation. Victoria University of Technology

Zijl, W and Trykozko, A (2002). Numerical homogenization of two-phase flow in porous media. Computational Geosciences: 6, 49-71.

N.N Industrial Quick Search URL:
<http://www.heatexchangers.org/info/heatexchangers>, February 2007

N.N: H-IP-O URL: www.hipo-online.de, February 2007

N.N: Filtration and Separation Buyers Guide URL:
www.filtsepbuyersguide.com, February 2007

N.N: Cleveland Eastern Mixers URL: www.clevelandmixer.com, February 2007

N.N: Corn Burner URL: www.thecornburner.com, February 2007

MICHIGAN STATE UNIVERSITY LIBRARIES



3 1293 02956 7512